Aus dem Leibniz-Institut für Neurobiologie
der Medizinischen Fakultät
der Otto-von-Guericke-Universität Magdeburg

Roles of TRPC4 Channels in the Hippocampal CA1 Region in Spatial Working Memory and Contextual Novelty

Dissertation

zur Erlangung des Doktorgrades

Dr. rer. medic.

an der Medizinischen Fakultät

der Otto-von-Guericke-Universität Magdeburg

vorgelegt von **Babak Saber Marouf**

aus **Tabriz**

Magdeburg 2024

Documentation sheet

Bibliographic Description:

Saber Marouf, Babak:
Roles of TRPC4 Channels in the Hippocampal CA1 Region in Spatial Working Memory and Contextual Novelty. 2024. – 165 pages., 91 Figures., 2 Tables.

Abstract

Working memory is the retainability of a small amount of information available for ongoing activities. Transient receptor potential channels (TRPC1–7) may be involved in this process. This study explores the role of hippocampal CA1 region's TRPC4 in spatial working memory and modulation of oscillations in novel context. After injecting the developed shRNA TRPC4 into the mice CA1 area, behavioral and electrophysiological data were recorded in T-maze and linear track to study spatial working memory and oscillations modulation, respectively. While behavioral results showed a significant decrease ($p<0.001$) in spatial working memory performance, theta-gamma coupling analysis revealed a significant reduction ($p<0.001$) in theta-gamma coupling for TRPC4KD group compared to scramble group. The groups exhibited significant differences in cells' spatial information. In addition, the spike phase histogram showed different distribution, mean phase, and resultant vector length in the main stem for TRPC4 compared to scramble. Local field potential analysis in linear track revealed the modulation of beta oscillations via hippocampal CA1 TRPC4 channels. Collectively, the study results indicate that TRPC4 impairs gamma and beta oscillations, theta-gamma coupling, spikes' theta phase, and firing rate. While the impairment in gamma oscillations may alter plasticity according to previous reports, theta-gamma coupling was the main mechanism impaired during the spatial working memory task, leading to behavioral deficits.

Keywords: Hippocampus; CA1; TRPC4; spatial working memory; theta-gamma coupling; beta oscillations

Abbreviations:

AAV	adeno-associated virus
ACC	anterior cingulate cortex
ACh	acetylcholine
ADP	afterdepolarization
AMPA	α-amino-3-hydroxy-5-methyl-4-isoxazolepropionic acid
AP	anterior-posterior
APP	amyloid precursor protein
AUC	area under curve
BDNF	brain-derived neurotrophic factor
CA	cornu ammonis
CaM	calmodulin
CaMK II	calmodulin kinase II
cAMP	cyclic adenosine monophosphate
CAN	cationic non-selective
CCh	carbachol
CCK	cholecystokinin
cDNA	complementary DNA
DG	dentate gyrus
DNMTP	delayed nonmatching-to-place
DV	dorso-ventral
DZNE	deutsches zentrum für neurodegenerative erkrankungen e.v.
EC	entorhinal cortex
EEG	electroencephalogram
EGF	epidermal growth factor
EPSP	excitatory postsynaptic potential
ER	endoplasmic reticulum
fMRI	functional magnetic resonance imaging
FN	false negative
FNR	false negative rate
FPR	false positive rate
GABA	gamma-aminobutyric acid
GC	granule cell
GCL	granule cell layer
GFP	green fluorescent protein
HF	hippocampal formation
HFO	high frequency oscillation
Hi	hilus
Hz	hertz
ING	interneuron network gamma
IP_3	inositol trisphosphate
LFP	local field potential
LIA	large irregular amplitude activity
LTD	long term depression
LTM	long-term memory
LTP	long term potentiation
LTS	long-term store
MAECs	mouse aortic endothelial cells
MC	mossy cell

MD	medialis dorsalis
MEC	medial entorhinal cortex
mGluR	metabotropic glutamate receptor
MI	modulation index
ML	medio-lateral
mRNA	messenger RNA
MS/VDB	medial septum and vertical limb of the diagonal band of broca
MTL	medial temporal lobe
mV	millivolt
nAChR	nicotinic acetylcholine receptor
NMDA	n-methyl-d-aspartate
O-LM	oriens lacunosum-moleculare
PaS	parasubiculum
PBC	pyramidal basket cell
PBS	phosphate buffered solution
PCPA	para-chlorophenylalanine
PF	persistent firing
PFA	paraformaldehyde
PFC	prefrontal cortex
PH	parahippocampal area
PING	pyramidal-interneuron network gamma
PIP2	phosphatidylinositol 4,5-bisphosphate
PKA	protein kinase a
PKC	protein kinase k
PL	polymorphic layer
PLC	phospholipase c
PM	plasma membrane
POR	postrhinal cortex
PP	perforant path
PrS	presubiculum
PSD	power spectrum density
PSD-95	postsynaptic density protein 95
PV	parvalbumin
qPCR	quantitative polymerase chain reaction
R	receptor
REM	rapid eye movement
RisPyr	rising phase-firing pyramidal cells in gamma cycles
ROC	receiver operating characteristic
ROI	region of interest
SG	stratum granulare
shRNA	short hairpin RNA
SLM	stratum lacunosum-moleculare
SLu	stratum lucidum
SM	stratum multiforme
SIA	small irregular amplitude activity
SO	stratum oriens
SP	stratum pyramidale
SR	stratum radiatum
STDP	spike-timing dependent plasticity
STE	short-term enhancement

STM	short-term memory
STS	short-term store
SuM	supramammillary nucleus
SWM	spatial working memory
SWR	sharp wave ripples
SWS	slow wave sleep
TP	true positive
TPR	true positive rate
TroPyr	trough-firing pyramidal cells in gamma cycles
TRP	transient receptor potential
TRPC	canonical transient receptor potential
VTE	vicarious trial and error
WM	working memory

Contents

Chapter 1 Introduction

1.1 Significance of Hippocampus and Memory

1.1.1 Introduction

The hippocampus, a structure located in the medial temporal lobe, comprises millions of neurons forming a network that is quite distinct from other regions of the central nervous system. A group of brain areas, including the hippocampus, dentate gyrus (DG), subiculum, presubiculum, parasubiculum, and entorhinal cortex (EC), creates hippocampal formation (1). The hippocampus has played a key role since the early years of brain research, attributed to its large, curved shape, visibly seen by ancient anatomists. The hippocampus was previously called cornu ammonis (Latin for the horn of the ram). This terminology remains in the acronyms for the hippocampal subfields CA1 (cornu ammonis), CA2, and CA3. The hippocampus became more attractive after microscopy emergence, with its condensed single-layer cell population. A notable instance is Camillo Golgi's picture from 1886; he used his groundbreaking new technique to show the hippocampus structure (1). In 1906, Camillo Golgi (1834–1926) shared the Nobel Prize for Physiology or Medicine with Santiago Ramón y Cajal (1852–1934, another outstanding neuroscientist) "in recognition of their work on the structure of the nervous system" (Figure 1.1.1) (2).

In parallel, clinicians interested in the basis of neurological conditions, such as epilepsy or Alzheimer's disease, were curious to study hippocampal formation. The pathological changes in the hippocampus and the potential for discovering novel therapeutics through its study remain the two main drivers of hippocampal research (1). Researchers have observed marked effects on memory following bilateral medial temporal lobe damage, with milder effects resulting from selective damage to the hippocampus. Patients with such conditions are often impaired in acquiring new, consciously accessible memories (3). Advanced studies on patient HM (Henry Molaison) have demonstrated the crucial role of the hippocampus and surrounding medial temporal lobe structures in memory function (4).

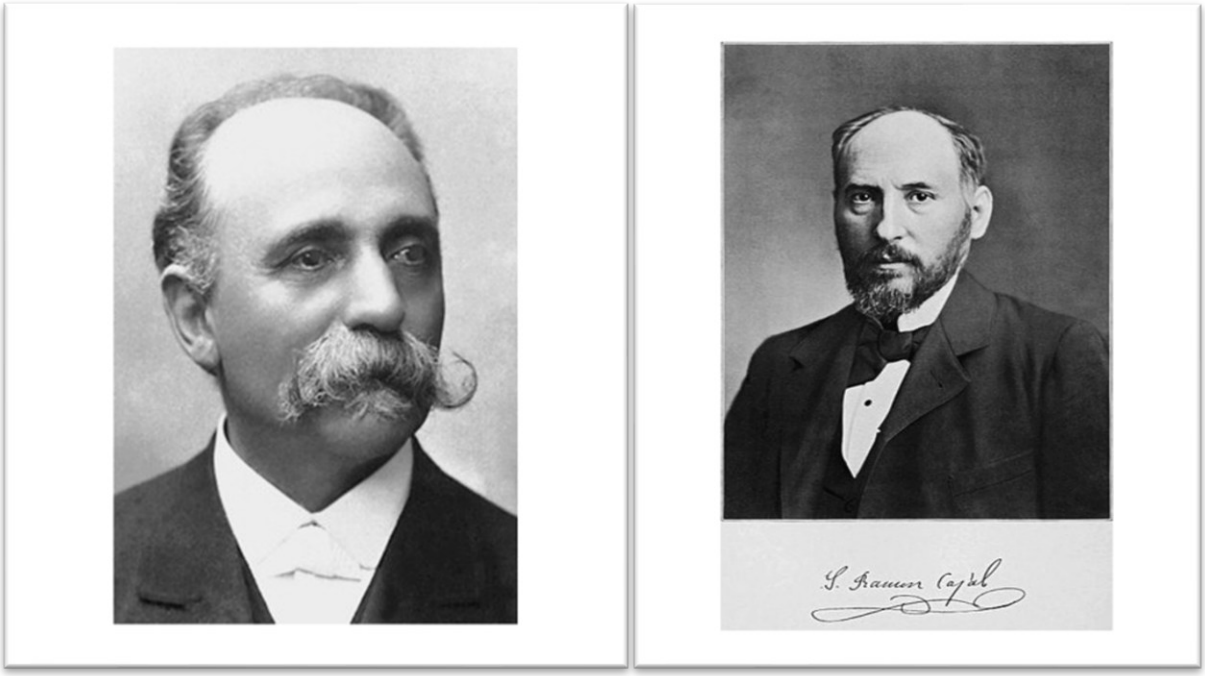

Figure 1.1.1: Left: Camillo Golgi (1834–1926). **Right**: Santiago Ramón y Cajal (1852–1934) (5).

1.1.2 Hippocampal function

As previously mentioned, researchers were inspired to study hippocampal formation due to various factors, including the profound memory deficits caused by bilateral medial temporal lobe damage and similar amnesia observed in animal models. These studies led to the development of several influential theories, such as Larry Squire's Declarative Theory of hippocampal function, the Multiple-Trace Theory, the Dual-Process Theory, and the Relational Theory, proposed by other researchers. Finally, O'Keefe and Nadel (The Hippocampus Book, 1978) proposed a neural-level conception of hippocampal function in a particular cognitive area. The declarative theory (Figure 1.1.2) posits that the hippocampus functions in coordination with other areas of the medial temporal lobe and is essential for all types of memory, including semantic (facts), episodic (events), familiarity, and recollection, particularly over a short temporal

duration. It further asserts that all memories are eventually consolidated in the neocortex, rendering them unaffected by medial temporal lobe damage (3).

Edward Tolman (1948) first proposed and explained cognitive map theory as the internal representation of a characteristic spatial map in his paper (Cognitive Maps in Rats and Men. Psychological Review, 55(4), 189–208). Getting all information from an outside environment (allocentric representation) is unfeasible. Thus, an internal representation of such an environment is certainly imperfect (6).

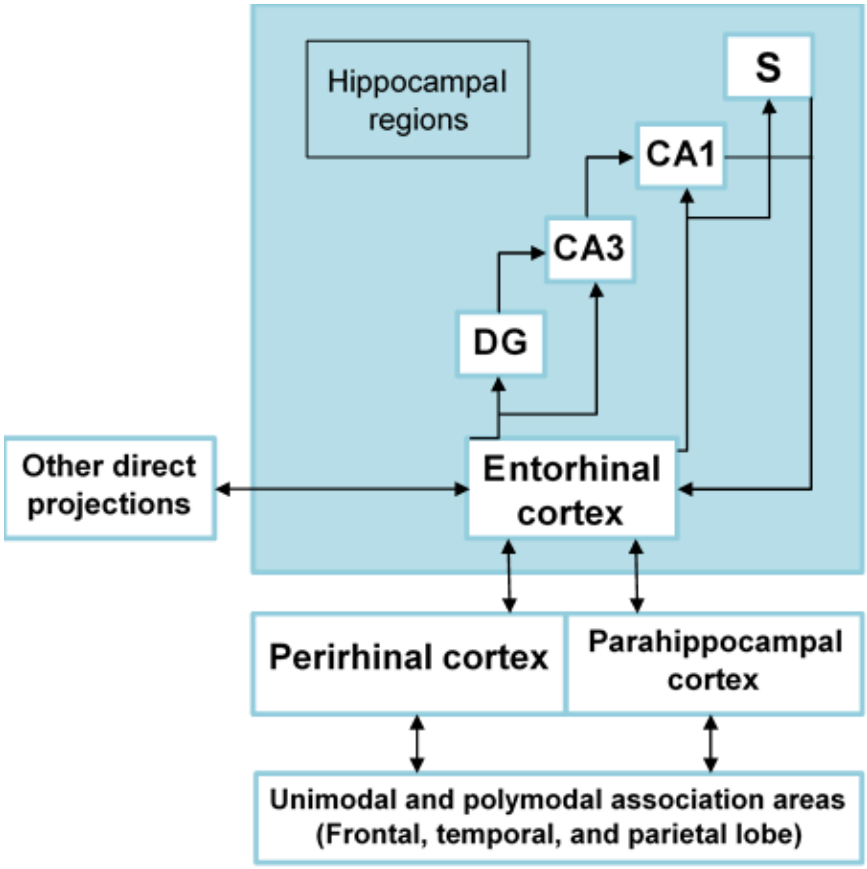

Figure 1.1.2: Medial temporal lobe memory system and the main parts of Squire and Zola-Morgan's (1991). Information enters the system from neocortical association areas. It is sent via the neighbor parahippocampal and perirhinal cortices to the EC, which is a crucial point for entering and exiting information into the hippocampal formation. Information enters hippocampal formation through a cascade of one-way projections before new signals for encoding or consolidating memories are fed back to the neocortex. Sub: subiculum (1).

Accumulating evidence supports the notion that a cognitive map is a defensible and convincing concept to decipher the actions of humans and other species. Internal changes in spatial information stay in working memory, with the outcomes linked to special conditions, places, or tasks (6). Tolman introduced behavior control by memory representations, which are organized as a cognitive map. He challenged the idea that behavior results solely from fixed stimulus–response associations. Instead, he proposed that animals develop a cognitive map, integrating different stimuli to regulate their final behavioral responses (7).

John O'Keefe and Nadel's (1978) were of the same opinion and emphasized mapping of connections in relational space between experiences in a spatial frame and flexible behavior. Their findings strongly implicated the hippocampus in spatial learning and memory. A review provided strong evidence that hippocampal damage impairs spatial learning and memory tasks, while nonspatial tasks and other types of spatial learning do not require the hippocampus (6,7).

O'Keefe and Nadel suggested two different systems that guide spatial learning and memory. The first system is the 'taxon' system; it uses egocentric cues and specific behavioral responses to particular stimuli or landmarks to provide route-based navigation. The second one, the 'locale' system, establishes allocentric spatial encoding and the formation of a cognitive map of the environment. They hypothesized that this cognitive map is retained in the hippocampus: place cells in the hippocampus of a behaving animal individually increases their firing rate only when the animal is in a well-defined area (place field) within the environment (Figure 1.1.3). Hippocampal lesions impair allocentric memory, unlike egocentric memory in varying tasks (Morris water maze, radial maze, T-maze-rewarded alternation, and many others), which aligns with this hypothesis (8).

O'Keefe clearly explained the relationship between place cells and cognitive mapping as follows:

"These findings suggest that the hippocampus provides the rest of the brain with a spatial reference map." (pg.174, O'Keefe and Speakman, 1971).

The authors mention that the map presents both the animal's current location and possible future position. Nevertheless, the main and rational hypothesis is that the hippocampus depicts locations in an allocentric, map-like way:

"The end point of the chapter will be the assertion that the hippocampus acts as a cognitive mapping system, which we shall call the locale system and which generates place hypotheses and exploration." (pg. 89–90, O'Keefe and Nadel, 1978.)

The demonstration of space by the hippocampus was a representation of a flexible place map in the Tolmanian sense for O'Keefe and Nadel (9). John O'Keefe received the 2014 Nobel Prize in Physiology and Medicine for his pivotal brain research in cognitive function (10).

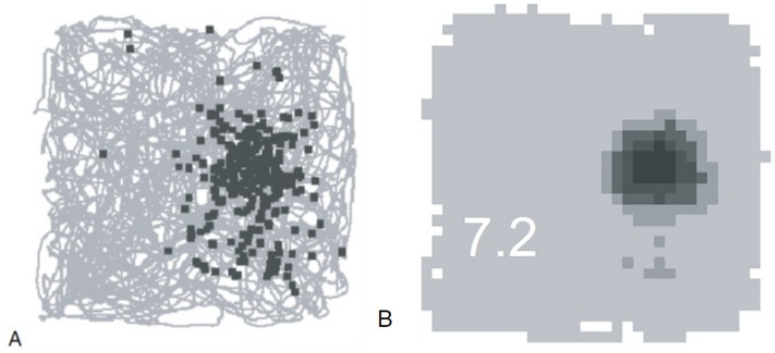

Figure 1.1.3: **A**: Firing locations (dark gray dots) of a CA1 place cell in a rat moving in an open field for 10 minutes. **B**: Place field in graded gray color. Darker colors mean a higher firing rate in the area. The number in the bottom left represents the peak firing rate of the cell (1).

1.2 Hippocampus Anatomy

The hippocampus is a stretched structure laid deep in the medial temporal lobe. It is called the hippocampus due to its likeness in dissection to a seahorse (genus Hippocampus). In rodents, the hippocampus is also quite large compared to other areas buried under the neocortex (Figure 1.2.1).

Coronal section of the hippocampus depicts textbook illustration of the 'trisynaptic loop' showing the hippocampal anatomical connectivity (Figure 1.2.2). The EC has the main and reciprocal projection to the hippocampus via perforant-

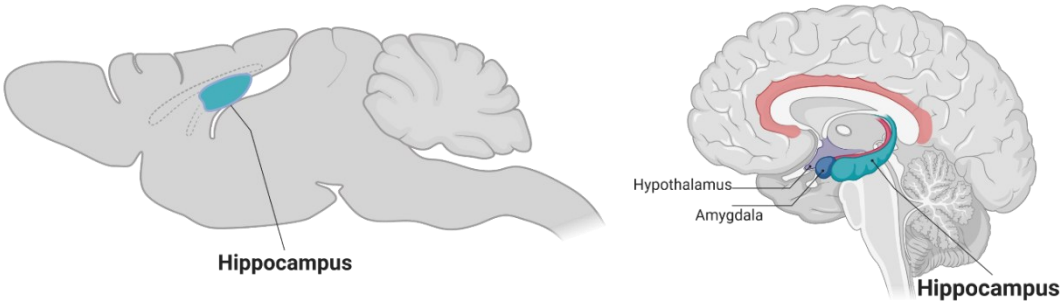

Figure 1.2.1: Left: mouse brain and hippocampus (blue). **Right**: Human brain and hippocampus marked in blue (11).

path to the DG. The DG projects via mossy fibers to CA3. CA3 projects via Schaffer Collateral to CA1. Apart from projections to CA1, the CA3 axon projection also creates a recurrent network with other CA3 neurons. The one-way projection network was thought to be mostly held through a section (lamellar hypothesis). The hypothesis posits the hippocampus as an arranged stack of these lamellae, assembled as independent operating modules along the longitudinal axis. However, more recent anatomical studies have proposed widespread connectivity along the longitudinal axis and dependent functionality in coronal sections (12).

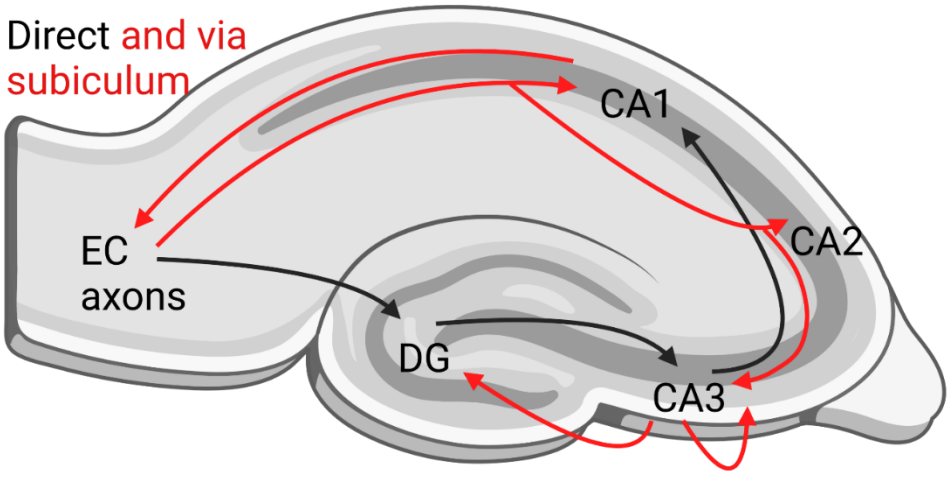

Figure 1.2.2: The black lines show classic 'trisynaptic loop' and the red lines depict other crucial pathways in the hippocampus, including projection from the EC to CA fields, the feedback to the EC through the subiculum, the recurrent collateral network of CA3, and the feedback projection from CA3 to DG (11).

Cornu Ammonis is made of four layers (Figure 1.2.3). The stratum lucidum (SLu) is the only mossy fiber-recipient layer in CA3. The other layers are easily distinguishable pyramidal layer [Stratum pyramidale] (SP) and on its basal side is the oriens layer of the hippocampus [Stratum oriens] (SO). The apical dendrites of the pyramidal neurons are split into the radiatum layer [Stratum radiatum] (SR) and the lacunosum-moleculare layer [Stratum lacunosum-moleculare] (SLM). SLu is located between the SP and SR layers. The pyramidal layer comprises large pyramidal neurons: the dendrites are aligned toward the radiatum layer and the axon positioned to the oriens layer. The axons unite in the alveus and unify in the fimbria. Finally, they form the fornix, which is the main efferent tract of the hippocampus (Figure 1.2.4). The fornix passes via the thalamus. The mouse hippocampus also has mostly excitatory projections to the amygdala. Another crucial efferent from the hippocampus is directed toward the prefrontal cortex, specifically targeting the cingulate, prelimbic, and infralimbic cortices. An efferent to the nucleus accumbens and hypothalamus exists. The hippocampus also has an afferent from the nucleus reuniens (13).

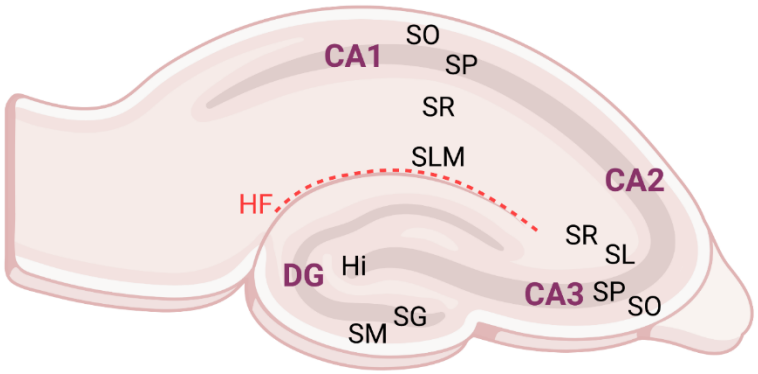

Figure 1.2.3: Coronal section through the mouse hippocampal formation, indicating the different layers of the Cornu Ammonis (CA) and the Dentate Gyrus (DG). CA: From external to internal, the stratum oriens (SO) with the axons of the pyramidal cells in the stratum pyramidale (SP) are traced by the strata radiatum (SR) and lacunosum-moleculare (SLM). The stratum lucidum (SL) is only present in the CA3 region. DG: the stratum moleculare anchors the dendrites of the granule cells in the stratum granulare (SG). The axons of the granule cells, the mossy fibers, leave the SG via the hilus (Hi) or stratum multiforme (SM). Hippocampal fissure (HF) (11).

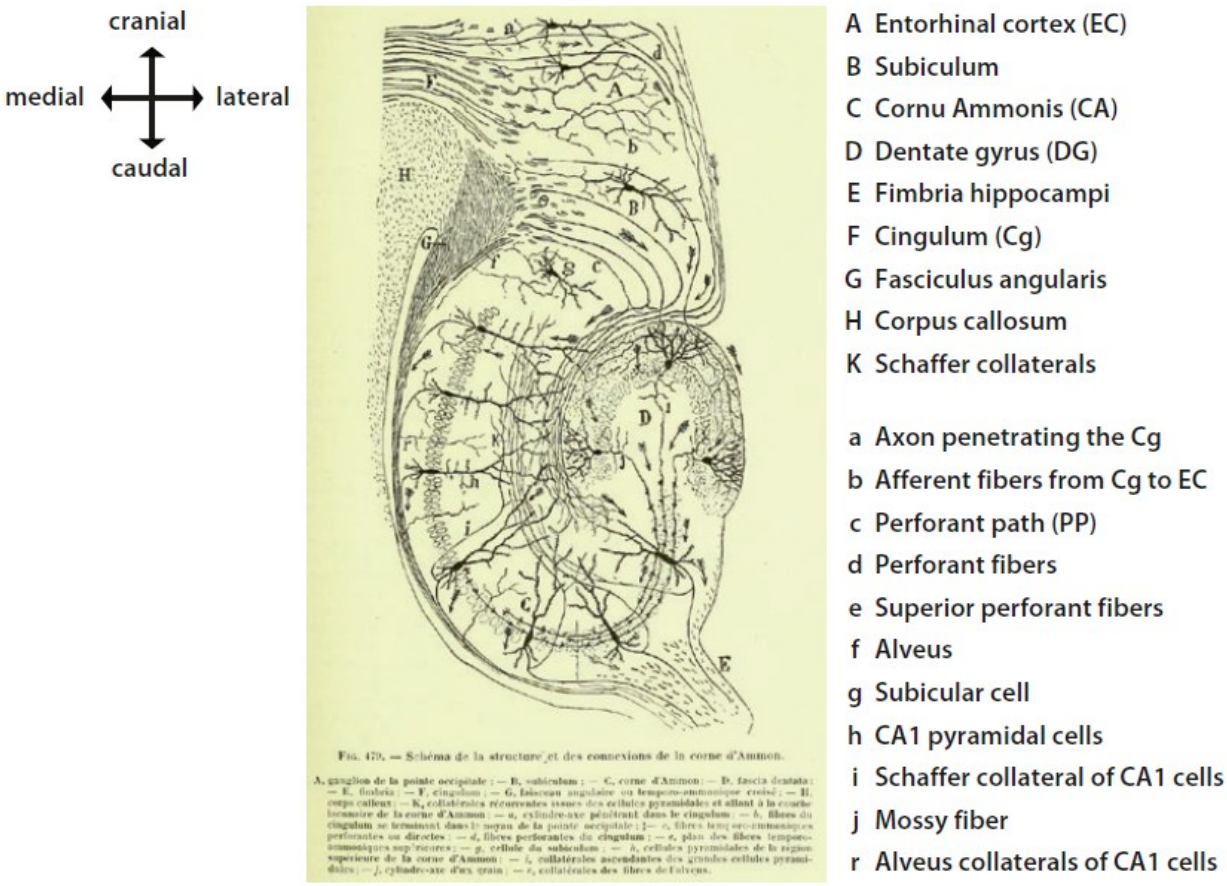

Figure 1.2.4: Trisynaptic loop: entorhinal cortex (A) has a projection to the dentate gyrus (D) and CA regions (C) via the perforant path (c, d). The dentate gyrus projects via mossy fibers (j) to CA3. CA3 projects to the CA1 region via Schaffer collaterals (K). Efferent fibers of the hippocampal formation project back to the entorhinal cortex (A) (13).

1.2.1 Morphology of hippocampal cells

CA1

Pyramidal cells of CA areas, granule cells in DG, and mossy cells of the hilus are the principal cells of the hippocampus, forming a largely homogenous population. CA1 pyramidal cells are the most studied cells in the brain. The pyramidal cells have a

pyramidal soma, a large caliber apical dendrite, and a number of small caliber basal dendrites (Figure 1.2.5). Although the cell bodies of the pyramidal cells are localized in the SP, dislocated pyramidal cells have been shown in the SR (14). The pyramidal cell diameter is around 15 μm and the surface area is 465 ± 50 μm^2. The apical dendrites expand in the SR, giving 9 to 30 side branches: the bifurcation ends in this layer and makes a dendritic tuft in the SLM. From cell bodies, 2–8 basal dendrites come out and bifurcate repeatedly and extend unto the alveus. The pyramidal cells have about 11.5–17.5 mm dendritic length. The spine distribution on the dendritic area is heterogeneous. Spine density is higher in the SO and SR and lower in the SLM (14). About 12,000 μm dendrites in single pyramidal cells have around 30,600 excitatory and 17,000 inhibitory synapses, with 40% located in the persomatic area and 20% in the SLM dendrites.

Proximal apical and basal SR and SO dendrites do not have spine or have scattered spines: distal part of dendrites in these layers has tightly packed spines (68% of dendritic tree). While the excitatory afferents end on dendritic spines, only dendritic shafts get inhibitory projections. Distal SR and SO dendrites receive very low (~3%) inhibitory inputs compared to proximal dendritic parts that have the most inhibitory inputs (70–100%). CA3 afferents project to SR and SO, whereas EC and other cortical structures, such as the nucleus reuniens and amygdala, innervate distal apical dendrites in the SLM (15).

CA3 and CA2

Morphologically, CA3 pyramidal cells share many similarities with CA1 pyramidal cells, but key differences exist. First, the surface area of the CA3 cell body is 2–4 times larger than that of the CA1 pyramidal cells. Second, the proximal dendrites of CA3 cells have larger and more complex spines. Third, the apical dendrite bifurcation in CA3 cells occurs much closer to the SP, with 2–3 apical dendrites emerging from the apical pole. The complex spines receive synaptic inputs from mossy fibers. The soma and dendritic surface without spines is 22,033–50,400 μm^2 (13).

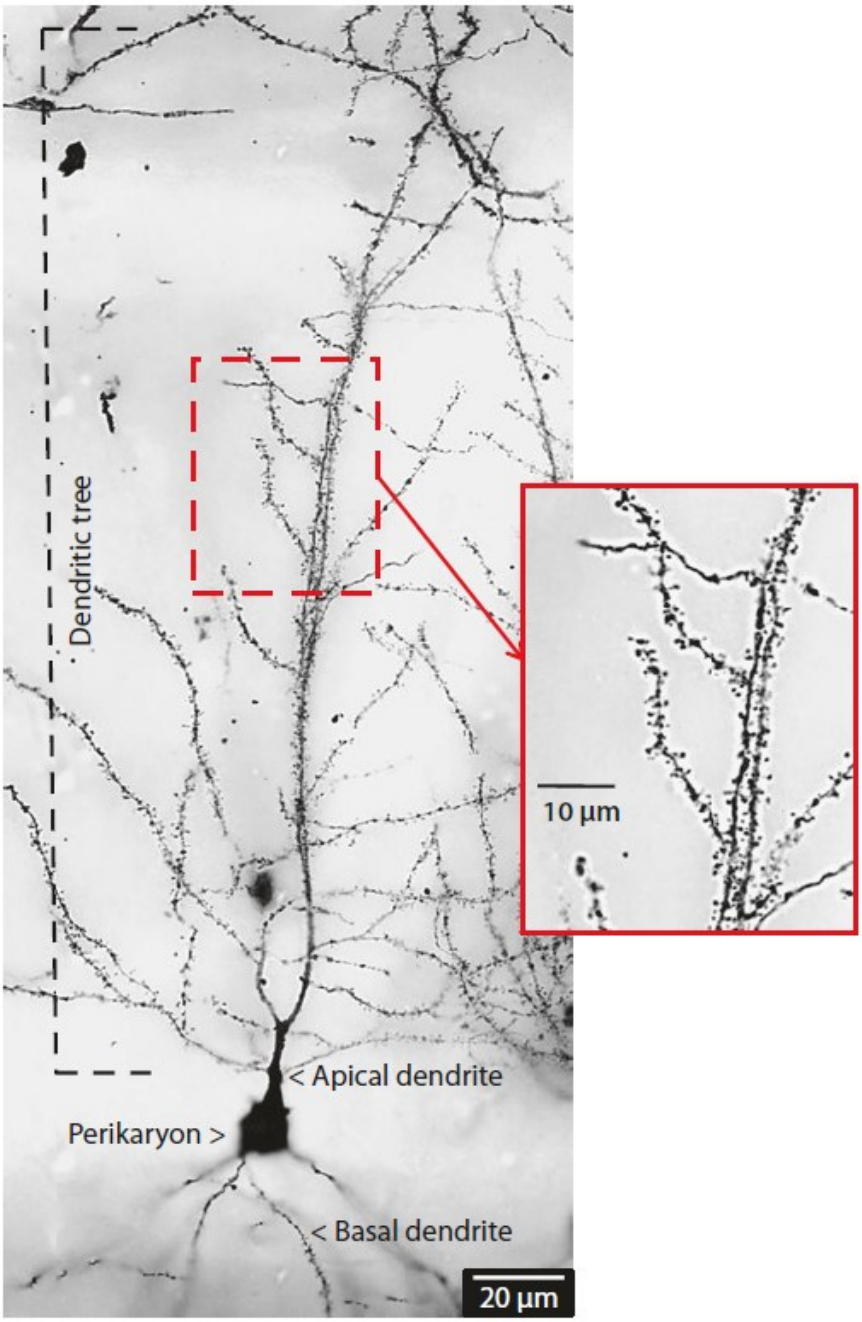

Figure 1.2.5: Mouse (C57BL/6) hippocampus (Cornu Ammonis). Golgi staining. A pyramidal neuron is shown with the dendritic compartment (dendritic tree, apical dendrite, and basal dendrites) and the perikaryon. Dendrites have dense dendritic spines (13).

The cell bodies of CA2 and CA3 pyramidal cells are almost the same size, and the surface areas of their cross section are 2–3 times of the CA1 pyramidal cells. CA2 and CA3 pyramidal cells have 1–3 primary apical dendrites that usually split to make 4 or more thick secondary apical dendrites. In contrast, CA1 pyramidal cells have 1–2 primary apical dendrites that do not bifurcate. CA3 and CA2 have 2–7 primary basal dendrites relative to 1–5 in CA1. While the distal apical dendrites in CA3 generally extend in a vertical direction, in CA1, the distal dendrites tend to extend horizontally (16).

DG

The DG has three layers: molecular (ml) or cell-free layer, granule cell layer (gcl), and polymorphic layer (pl) (Figure 1.2.6). The molecular layer is branched into:

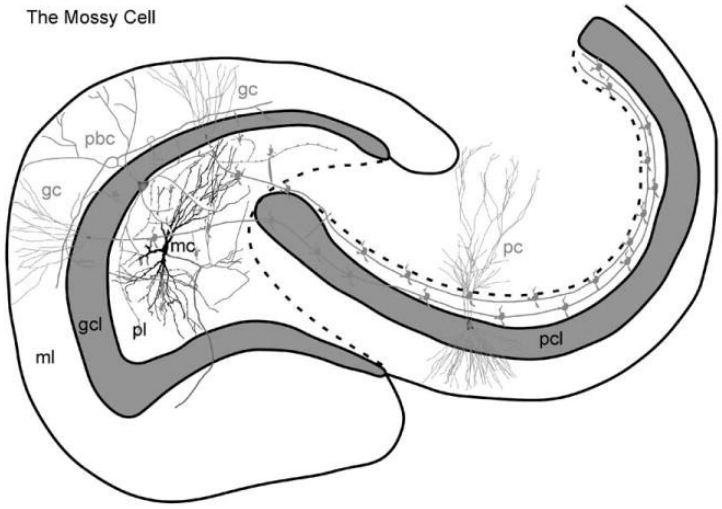

Figure 1.2.6: The dentate granule cell (gc) with an axonal arbor. Most synapses are onto the dendrite of inhibitory interneurons in the polymorphic layer. Many of the mossy fiber expansions in the polymorphic layer terminate in the proximal dendrite of the mossy cells (mc). Mossy fiber project to CA3 The pyramidal basket cell (pbc) body is located between the granule and polymorphic cell layers. The axon synapse with granule cell bodies. The mossy cell (mc) axons develop a plexus in the polymorphic layer and an ipsilateral projection to the inner molecular layer (the associational pathway); the axon also projects contralaterally to the inner molecular layer, forming the commissural pathway (17).

three sublayers based on the laminar organization of inputs. The fibers of the perforant path and other external inputs to the DG, dendrites of the granule cells, and a few interneurons are located in the molecular layer. The granule cell layer comprises dense granule cells. Some other neurons are placed at the boundary of the granule and polymorphic cell layers, such as dentate pyramidal basket cells. No glial sheath exists between the granule cells. The principal cells of the DG are granule cells with elliptical cell bodies and cone-shaped apical dendrites in the molecular layer. The second type of cell in the DG is mossy cells located in the polymorphic layer. Their cell bodies are large and triangular or multipolar in shape. Proximal dendrites of mossy cells are covered by huge complex spines. The distal dendrites of the mossy cells seem to have a less dense spine than the hippocampal pyramidal cells. Mossy cells innervate granule cells and GABAergic neurons (17).

Hippocampal interneurons-CA1

The pyramidal cells of CA1 predominantly receive GABAergic and glutamatergic synaptic inputs. Local GABAergic inputs help in cell assembly formation by controlling pyramidal cell activity. The local GABAergic interneurons tune the firing rate of pyramidal cells and their spike timing, and synchronize their activity (18). Basket cells target the somata and proximal dendrites; axo-axonic interneurons target the initial segments of the axon, and they can potentially control the output of pyramidal cells. However, 92% of GABAergic synapses in CA1 are located on the dendrites of pyramidal cells rather than on the initial segments of the somata or axon. Interneurons innervating dendrites of CA1 pyramidal cells are categorized into four cell groups: parvalbumin (PV), cholecystokinin (CCK), axonal arborization density, and long-range projections. Overall, the four cell groups have 12 distinct cell types (Figure 1.2.8) (18).

Unlike organized pyramidal cell bodies in the SP in CA1 and other hippocampal subfields, interneuron bodies are spread all over the main subfields. The location of interneuron somatodendritic arbors grants them integration with a more restricted intrinsic and extrinsic afferent input collection compared to pyramidal cells. Interneurons are the main provider of GABAergic synaptic input, utilizing Cl^- influx or K^+ efflux via $GABA_A$ or $GABA_B$ receptor activation to transiently hyperpolarize or shunt the cell

membrane away from the action potential threshold. They markedly contribute to the adjustment of single-cell excitability while controlling the temporal window for synaptic excitation and latter action potential beginning, thereby adjusting the timing of the afferent and efferent information stream. Moreover, they restrain and synchronize both local and distributed cortical circuits to boost oscillatory activity in wide frequency ranges (19).

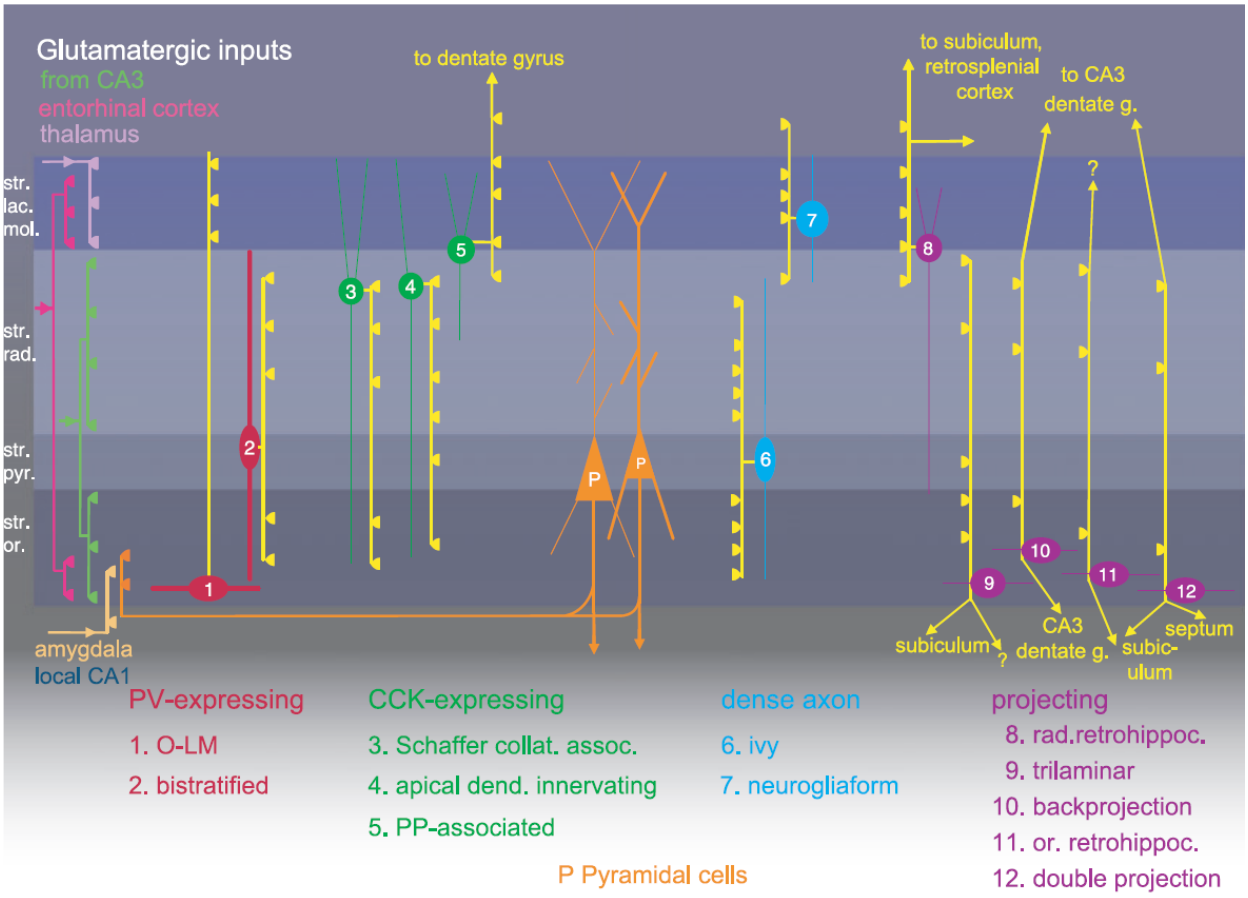

Figure 1.2.8: 12 types of GABAergic interneurons split up into four cell groups project to CA1 pyramidal cell dendrites (orange). Abbreviations: str., stratum; lac. mol., lacunosum moleculare; pyr., pyramidale; or., oriens; g., gyrus; O-LM, oriens lacunosum-moleculare; PP, perforant path; retrohippoc., retrohippocampal projecting (18).

The spiking of neurons is synchronized within anatomical layers of the brain, such as the CA1 region of the hippocampus. This synchronized activity is reflected in network oscillations observed in extracellular field potentials. The cellular mechanisms underlying network oscillation and its maintenance are of primary interest, with GABAergic interneurons identified as the main contributors to the synchrony of pyramidal cell activity. Interneurons with synapses on the soma and axon initial segments of pyramidal cells undoubtedly contribute to network oscillations. Gamma oscillations (30–80 Hz) occur during various behavioral stages and are simultaneously regulated by theta oscillations (4–12 Hz) (18).

1.3 Spatial Working Memory

1.3.1 Introduction

Working memory is defined as the ability to maintain a small amount of information that is accessible for current activities. It plays a crucial role in decision making, staying on track in conversations, navigation, and supporting creative thinking and problem solving. Additionally, working memory helps in remembering tasks, updating information about our surroundings throughout the day, and managing daily activities. Philosopher John Locke (1690) proposed the main idea and mentioned ‘contemplation’ in contrast with the ‘storehouse of ideas’ (20).

Hermann Ebbinghaus created the term ‘memory’ in 1880 and then William James in 1890 distinguished the difference between primary and secondary memory. Currently, the most accepted classification of memory includes short-term, long-term, and working memories (21). The term working memory was used for the first time in brief by Miller, Galanter, and Pribram (1960); however, the main theoretical progress was made by Alan Baddeley and Graham Hitch (1974), and further work by Baddeley and colleagues (20). After a series of experiments studying the role of memory in reasoning, learning, and comprehension, Baddeley and Hitch (1974) proposed an alternative for short-term memory (STM) and termed it working memory (22). Olton used the working memory term for the performance of rats in the radial arm maze task; in this task, animals need to remember the baited arms in several trials during a day in order to enhance the

reward; this would be considered long-term memory (LTM) within the human context (23).

This section seeks to review the crucial working memory models proposed by leading neuroscientists and psychologists and the models' cons and pros.

1.3.2 Working memory models

By the 1960s, the categorization of memory into two or more types had been widely accepted, which led to the development of various memory models. Among these, Atkinson and Shiffrin (1968) proposed the most influential model, known as the "modal model." This model presumes three separate memory types (Figure 1.3.1). The shortest of these was a series of sensory memory systems that may be considered parts of perceptual processing. These comprised visual sensory memory (Sperling 1960), also called iconic memory, and its identical sensory acoustic storage system (Crowder and Morton 1969), named echoic memory by Neisser (1967). Other sensory inputs were also reckoned to contain some form of transient storage. Information was thought to pass from a parallel array of sensory memory systems to a solo short-term store. This worked as a working memory of the small data storing potential or the short-term store (STS). STS can retain and change information. It was presumed to encode information into LTM and later retrieve it. The small information capacity STS system therefore had an interplay with a long-term store (LTS). Thus, long-term learning also relies on LTS and STS (24).

The model faced two problems. The first issue was the assumption that merely maintaining information in STM would guarantee long-term learning. In other words, it suggested that simply holding information in STM was sufficient for transferring it to LTM, and that the longer information remained in STM, the higher the likelihood of it being transferred to LTM, resulting in better learning. This idea was rejected because the degree of learning largely depends on the depth of processing. Therefore, encoding information based on its emotional tone or meaning is far more effective for learning than focusing on superficial aspects, such as verbal sound or mere perception. The second problem with this model is that information should be quickly lost without an

adequate STM, leading to impaired learning. In addition, patients with impaired STM should be severely cognitively handicapped, and LTM should also be impaired if this system operates as working memory (23,24).

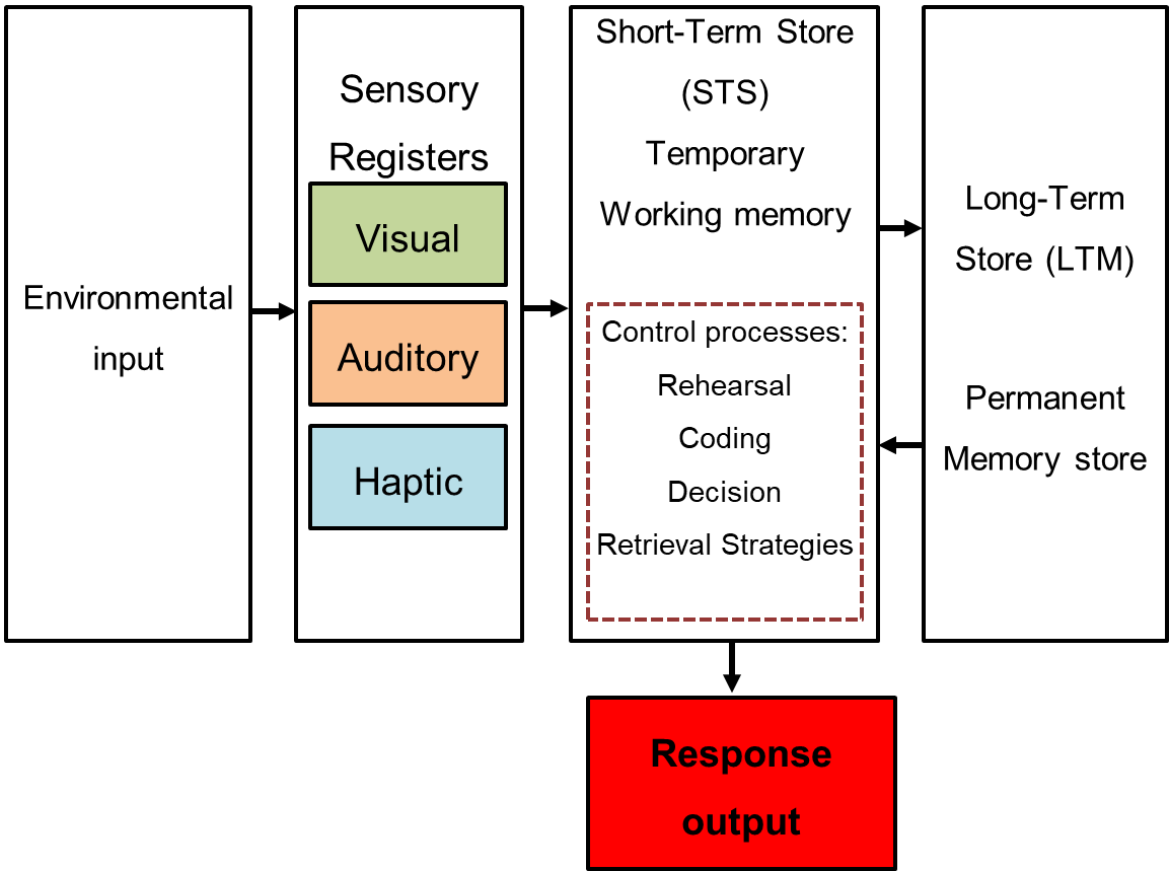

Figure 1.3.1: The modal model proposed by Atkinson and Shiffrin (1968). Information passes from the environment to a series of sensory registers and then into a short-term store. Short-term stores play an essential role in maintaining the current of information toward and out of the long-term store.

In 1974, Baddeley and Hitch proposed a three-component model; this comprises an attentional control system, the central executive system, supported by two short-term storage systems, one for visual data called visuo-spatial sketchpad and the other for verbal acoustic data called phonological loop. All three have a finite size (Figure 1.3.2).

The central executive is supposed to comprise a finite supply of universal processing size (23,24).

Baddeley's proposed model is modified and shows that information flows from LTM to the loop and vice versa. An essential difference is made between working memory and LTM. Working memory is depicted as a series of fluid systems that need only transient activation, and LTM indicates more enduring crystalized skills and knowledge.

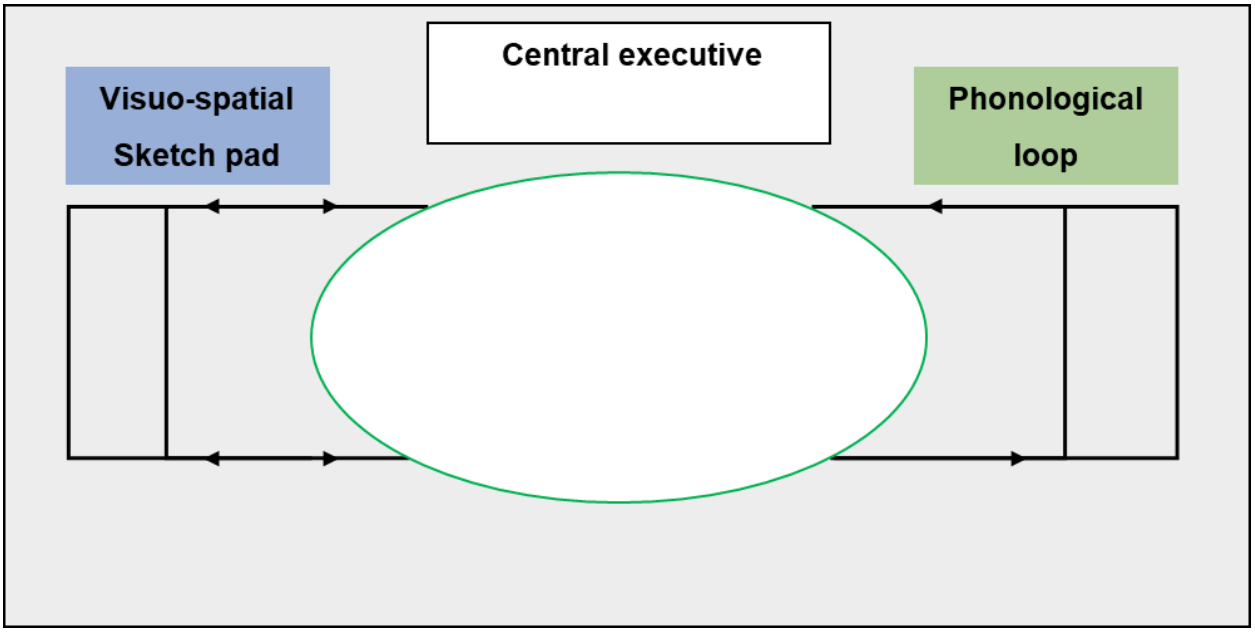

Figure 1.3.2: The working memory model proposed by Baddeley and Hitch. This model includes an attentional control system and two temporary stores. The components interact and are connected to both perception and LTM. Adapted from Baddeley et al. (2010) (23).

A new component, called the episodic buffer, was added to the model. It acts as a bridge between working memory, LTM, and perception, integrating information across these systems. It has a limited size like most buffer stores (25). The episodic buffer holds multidimensional episodes or pieces, which may integrate visual and auditory information, probably with smell and taste (Figure 1.3.3) (23).

1.3.3 Spatial working memory in animals

The capability to assess working memory in nonhuman animals would be highly fruitful for examining models of disorders known to affect working memory in humans, such as schizophrenia, dementia, and developmental disorders like attention deficit hyperactivity disorder. Olton et al. (1979) proposed that measuring working memory is feasible in rodents using win-shift spatial learning tasks. The term ‘working memory’ was used in David Olton and Werner Honig's experiments in 1970. Olton et al. (1979) proposed that spatial working memory could be differentiated

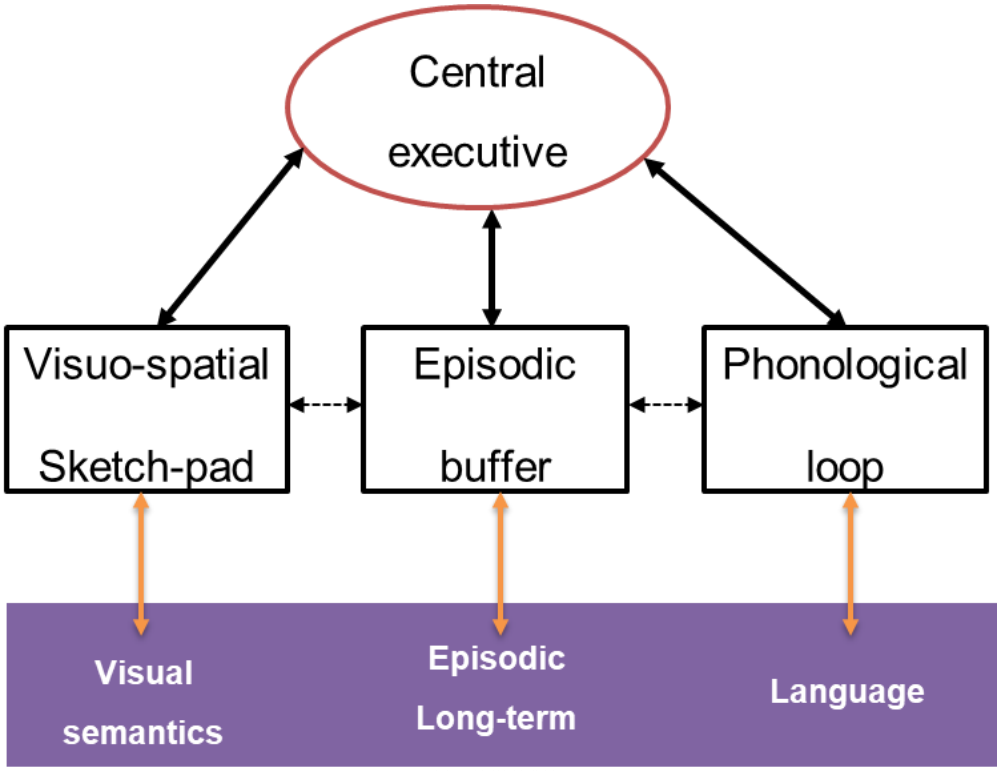

Figure 1.3.3: Multicomponent model advancement. It includes a connection to long-term memory and the episodic buffer as a fourth component.

as a distinct process from spatial reference memory. They proposed that spatial working memory requires the ability to retain trial-specific information for a limited period, allowing flexible responses to spatial stimuli. In contrast, spatial reference memory

involves the ability to learn a consistent response to a stimulus based on a fixed relationship between the stimulus and the outcome (26).

Olton and Samuelson designed the radial arm maze, a classic task for evaluating memory in rodents (Figure 1.3.4). The maze contains eight arms with a central platform. Food rewards are placed at the end of each arm. They observed that rats learned to visit each arm and get back the food reward from their arms without re-entering a previously baited arm. Trained rats usually visited more than seven correct arms before an error occurred. The authors excluded the possibility that the rats visited arms in a specific order, used odor marking to choose the arm, or relied on other types of cues. Based on these findings, Olton defined working memory as a memory that enables the animal to recall which arms were baited in a session (27).

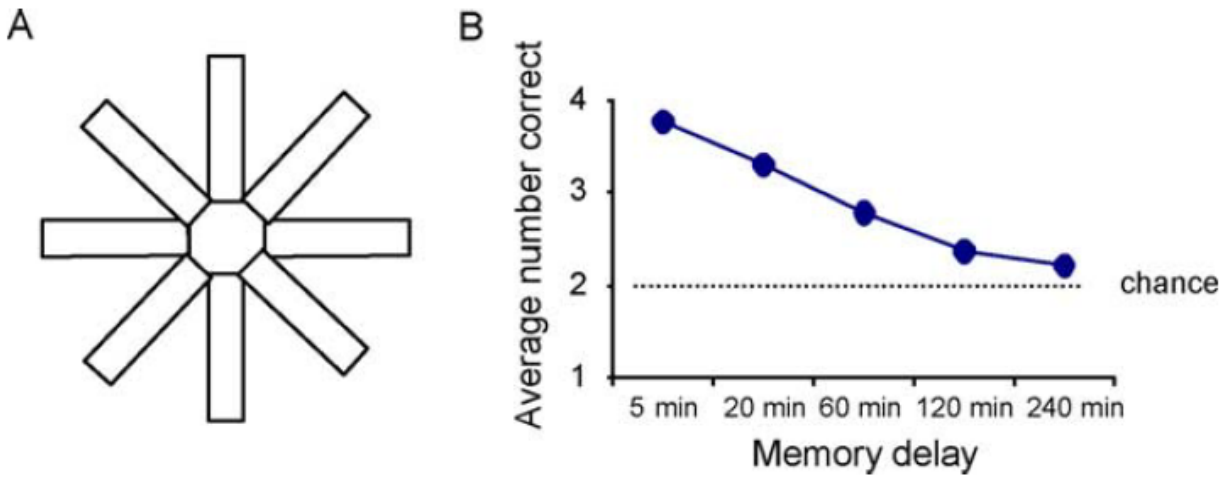

Figure 1.3.4: (A) Radial arm maze with 8 arms. (B) Increasing the delay between the fourth arm choice and the remaining arm choices results in a performance decline (27).

This memory becomes irrelevant the next day, as all arms are visited again. Working memory is described as the representation of cues during a delay period when the cues are no longer present, allowing for later decision-making and responses (27).

Another principal maze task to evaluate the spatial working memory is delayed alternation, which highlights the rats' propensity to choose alternate arms of the maze or locations when they are in the apparatus again. This is an STM task since the animal should remember the initial choice to elect the alternative arm. The T-maze is probably the most popular version of the delayed alternation problem (Figure 1.3.5) (27).

Olton asserted that optimal performance on the T-maze requires recalling information about the sample arm during the interval between the end of the sample phase and the beginning of the choice phase. Lesions of the hippocampus deeply change performance

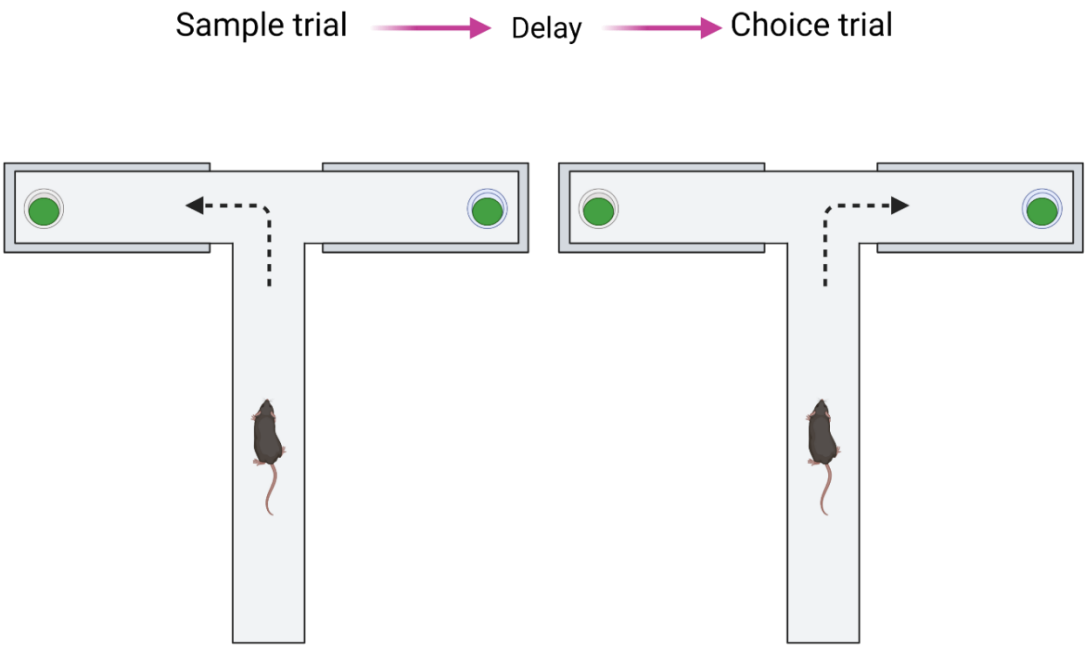

Figure 1.3.5: T-maze delayed alternation task. On the first sample run, the rat/mouse is placed on the main stem area and allowed to enter one of the arms. The animal may then be removed from the maze for a delayed duration. After the delay, the animal is returned to the main stem and will choose the other arm in most cases. A sample trial could be a forced trial in which the animal needs to turn to one arm. In this case, it is called the forced alternation task (11).

on both T-maze alternation and shift, nonmatching-to-place behavior in the radial arm maze. Lesions to the entire hippocampus typically result in animals performing at a chance level. However, determining whether the lesions specifically impair spatial working memory, disrupt the ability to form or use a spatial representation, or affect both processes remains challenging (26).

1.4 Cellular Mechanisms of Working Memory

1.4.1 Neuromodulation-cholinergic system

Introduction

Small stores of neurons in the brain stem, pontine nucleus, and basal forebrain comprise the neuromodulatory system in mammals: the stores could be thousands of neurons in rodents and tens of thousands in humans and could markedly influence cognitive functions. The neuromodulatory system comprises cholinergic, dopaminergic, serotonergic, and noradrenergic projections to various brain regions, all of which are involved in rewards, novelty, risks, endeavor, and social collaboration. These subsystems make a foundation for higher cognitive tasks such as goal-directed behavior, decision-making, emotion, and attention. These originate from the interplay between the neuromodulatory system and brain regions such as the hippocampus, frontal cortex, sensory cortex, striatum, and anterior cingulate (Figure 1.4.1.1) (24).

This section will focus on the cholinergic system due to its key role in memory and learning and its cholinergic neuron projections to the hippocampus.

Receptors

The cholinergic system is located in the basal forebrain and comprises nerve cells that employ acetylcholine (ACh) for activation or release when a nerve impulse propagates (28,29). This system plays many cognitive roles, including memory, attention, and emotions. ACh is produced in cholinergic cells containing acetyltransferase enzymes. It is metabolized and degraded by acetylcholinesterase to choline and acetic acid. These choline molecules are later used for ACh synthesis (28). The two ACh receptor types are nicotinic (subtypes: N1, N2, N3, N4, and subunits: α, β,

δ, ɣ subunits for every subtype) and muscarinic receptors (M1, M2, M4, M4, M5). The α7 nAChR is an essential receptor in hippocampal memory. The hippocampus expresses almost all nAChR subtypes and highly expresses the α7 nAChR pre- and post-synaptically. Receptor allocation is greatly conserved across species (30). The nicotinic receptor shapes ligand-gated ion channels in the membrane, with its activation resulting in cation influx. The muscarinic receptors shape G protein-coupled channels. Among the five muscarinic receptor subtypes, M1, M2, and M4 are more dominant (28).

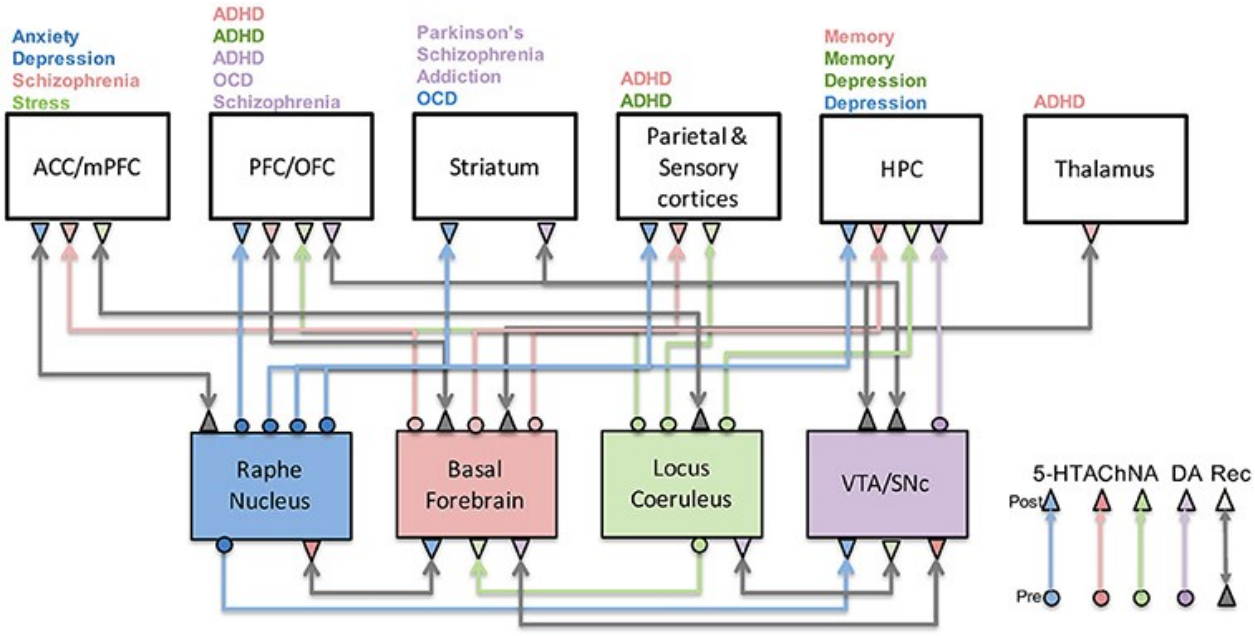

Figure 1.4.1.1: Four main neuromodulatory systems and their relation to each other. Their role in disease is also highlighted in different colors related to the corresponding neuromodulatory system. Serotonergic: blue, cholinergic: red, noradrenergic: green, dopaminergic: purple. Gray arrows indicate recurrent connections (29).

The cholinergic network has been involved in the cognitive function in normal and disease conditions. It began when Dr. Alois Alzheimer (1906) discussed the symptoms and neuropathology of the disease that carries his name today. Non-neuronal cells,

including peripheral macrophages, microglia, and astrocytes, also react to ACh. These non-neuronal cells affect short-term and long-term synaptic plasticity and function; via these mechanisms, they can help enhance or impair cognition. ACh might affect hippocampal function through the central and peripheral immune systems. ACh disrupts hippocampal astrocytes and consequently controls hippocampal neuron firing (30). Hasselmo proposed that high ACh levels promote encoding by stopping improper activations (31). The release of ACh from the septohippocampal pathway leads to the gradual inhibition of dentate granule cells by activating astrocytes. The nAChR antagonist can hamper astrocyte activation, which implies that astrocytes react particularly to basal forebrain projections via α7 nAChR. Activation of α7 nAChR on astrocytes triggers glutamate release, which in turn inhibits the activation of dentate granule cells via hilar inhibitory interneurons (32,33). This reduced firing rate leads to a decrease in the firing rate of CA3 pyramidal cells, preventing the involvement of past associations in the encoding process. Moreover, microglia play a crucial role in hippocampal memory through the release of brain-derived neurotrophic factor (BDNF) (30).

Circuits of the cholinergic system and roles in cognition

Three main regions in the brain with cholinergic neurons are the brain stem (inhibiting thalamus), striatum (cholinergic interneurons suppressing dopamine release), and basal forebrain (medial septum, vertical limb of the diagonal band, horizontal limb of the diagonal band, and nucleus basalis) (30,34). The circuits play a crucial role in cognitive function of the hippocampus, amygdala, olfactory bulb, prefrontal cortical, and ventral tegmental area projections to the striatum. All regions of the hippocampus receive cholinergic neurons input from the medial septum and vertical limb of the diagonal band of the broca (MS/VDB) (30,34).

The primary function of ACh is in memory consolidation based on sleep–wake cycle research. Hasselmo et al. (2012) proposed that memories are retrieved when recurrent connections are powerful due to lower ACh levels. During slow-wave sleep, attenuated ACh levels in the hippocampus result in recurrent activity rise, easing memory consolidation, whereas ACh levels are increased in rapid eye movement (REM)

sleep or awake subjects. This leads to ACh level elevation, increasing cortical input to the hippocampus and enhancing memory encoding (Figure 1.4.1.2) (29).

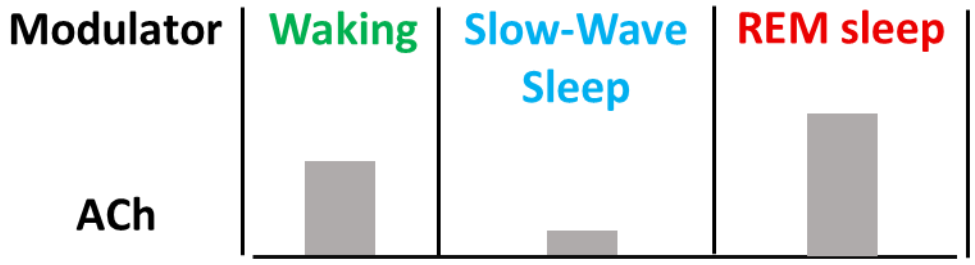

Figure 1.4.1.2: Acetylcholine levels change during waking, slow-wave sleep, and REM sleep in cortical structures. Histogram bars show ACH levels relative to the waking state. The ACh was measured by microdialysis.

Depletion of cholinergic inputs in the hippocampus and prefrontal cortex (PFC) impairs working memory systems. Cholinergic depletion after basal forebrain lesions impairs primate spatial working memory. Moreover, administering local scopolamine in the perirhinal cortex reduces learning of trace fear conditioning tasks. Interestingly, blocking muscarinic receptors does not affect performance of STM tasks, for instance digit span (35). This suggests that familiar stimuli might strengthen synaptic connections; cholinergic modulation in working memory seems more pivotal for novel stimuli than familiar ones (35).

1.4.2 Persistent firing

Introduction

Working memory is a system that retains and manages information for many seconds through the planning and execution of several cognitive tasks. Working memory employs frontoparietal and other surrounding brain regions (36,37). Initially, the neuronal basis of working memory was believed to be the persistent activity (persistent firing) of a specific neuronal population (36). However, recent advances have introduced new perspectives on the possible mechanisms of working memory, including

synchronized oscillations and changes in synaptic plasticity. These ideas suggest that short-term synaptic facilitation, precise tuning of recurrent excitation and inhibition, and intrinsic network dynamics are key components of working memory function (36,37).

Persistent firing

Persistent firing/spiking/activity is the consecutive action potential even with disappearing of the stimulus. Persistent firing is believed to be the key mechanism involved in bridging the temporal gap (delay) of working memory-dependent tasks (38–40). The mechanism is verified in the *in vivo* study of prefrontal neurons in the early seventies; these neurons showed escalated firing in the delay period of the working memory task (38). Traditionally, in landmark studies, monkeys were presented with a temporary stimulus and trained to recall and indicate that stimulus after a delay period, even when the stimulus was no longer present. Electrophysiological recordings from monkeys' PFCs showed sustained and increased firing rates during the delay period, which is controlled by the identity of previously shown stimulus (Figure 1.4.2.1) (41).

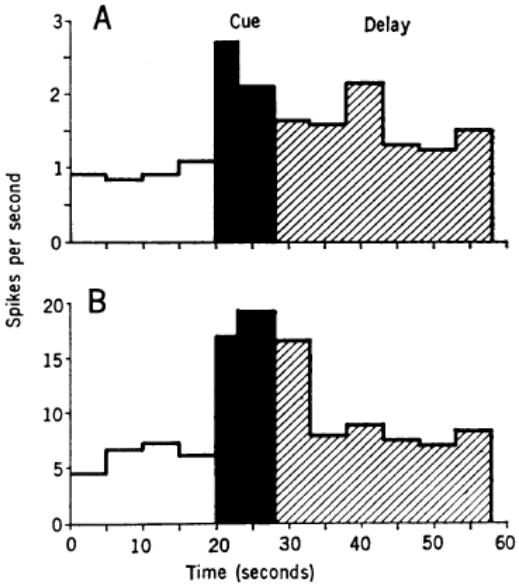

Figure 1.4.2.1: Mean firing rate of two neurons in five delayed responses during voluntary activity (20 sec), during cue, and during delay period (30 sec). **A:** Neuron in the prefrontal cortex. **B:** Neuron in the medialis dorsalis (MD) (41).

During the delay period, 65% of PFC units and 58% of the medialis dorsalis units showed increased firing frequency compared to frequent intertrial times (42). Some units exhibited higher spiking only in the cue presentation, some only during the delay time, and some in both periods. The increased firing rate was preceded by an inhibitory phase during the cue period. This was the most remarkable in neurons showing the highest spiking (Figure 1.4.2.2 & 1.4.2.3) (41). Further studies reported similar delay period activity in the temporal cortex, parietal cortex, auditory cortex, visual cortex, somatosensory cortex, presupplementary motor area, and medial promotor cortex. In rodents, increased activity during the delay period has been reported, similar to monkeys, but fewer cells were active during this period compared to monkeys. In contrast, most of these cells in rodents fire within specific time windows, which collectively cover the delay period, resulting in a sequential firing pattern that represents upcoming behavior (43).

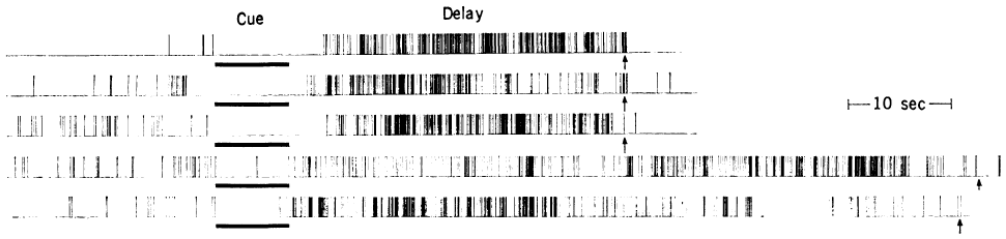

Figure 1.4.2.2: Firing raster plot of a prefrontal cortex neuron in five continuous trials with 32, 32, 32, 67, and 65 seconds delay period (41).

Furthermore, *in vitro* studies have reported persistent firing in different brain regions. Egorov et al. (2002) reported persistent firing in layer V of an EC single neuron. Layer V of the EC connects the hippocampus to other cortical areas. The maintained firing rate could be elevated or reduced based on a special input way. The activity is related to cholinergic muscarinic receptors and depends on Ca^{2+} sensitive cationic current (Figure 1.4.2.4) (44). M_1 muscarinic receptors or metabotropic glutamate receptors in medial EC were activated by a short stimulus; this results in triggering a non-selective cationic current (I_{CAN}) and persistent firing (45).

Persistent activity was observed in the postsubiculum, where a brief 200-ms stimulus was enough to induce sustained firing. Additionally, persistent firing has been demonstrated in other brain regions, such as the medial vestibular nucleus, nucleus prepositus hypoglossi, and area I neurons in the brainstem (45). *In vitro* slice recording results of hippocampus CA3 pyramidal cells and perirhinal cortex revealed persistent firing in the presence of the cholinergic agonist carbachol (CCh). In CA1 interneurons, persistent firing can be induced by several stimulations of the axon's distal end. In DG semilunar granular cells, persistent firing can be triggered via perforant path stimulation. However, the muscarinic receptor antagonist atropine did not alter persistent firing, suggesting a distinct mechanism compared to other studies (46,47).

ACh also modulates persistent spiking in the *in vitro* slice preparation of rat medial EC. Increased entorhinal and hippocampal spikes have been observed in both humans and monkeys, indicating that ACh, in response to distinct stimuli, may play a key role in regulating persistent firing (35). Persistent firing is proposed as a mechanism for working memory. Cholinergic agonist application such as carbachol

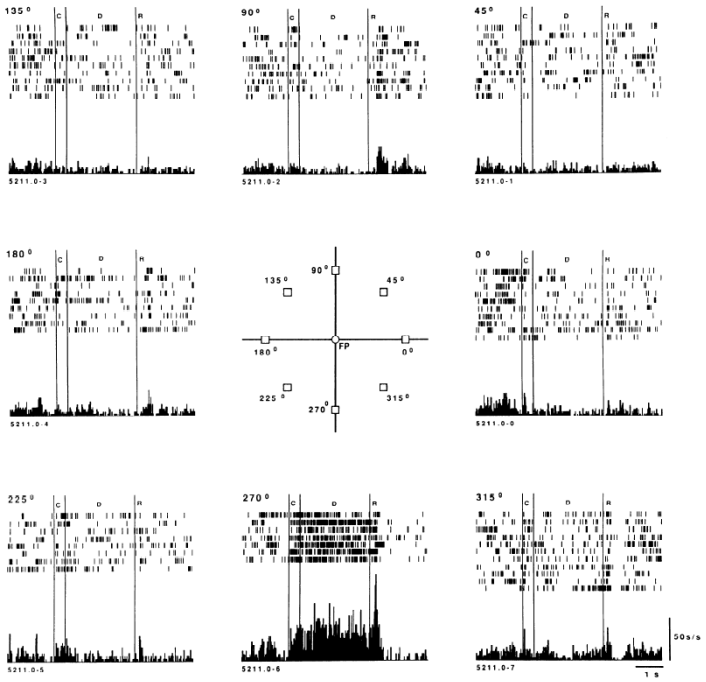

Figure 1.4.2.3: Neurons with persistent activity responding to cue position in task (270°) recorded from monkey caudal area (arcuate sulcus) of the principal sulcus (48).

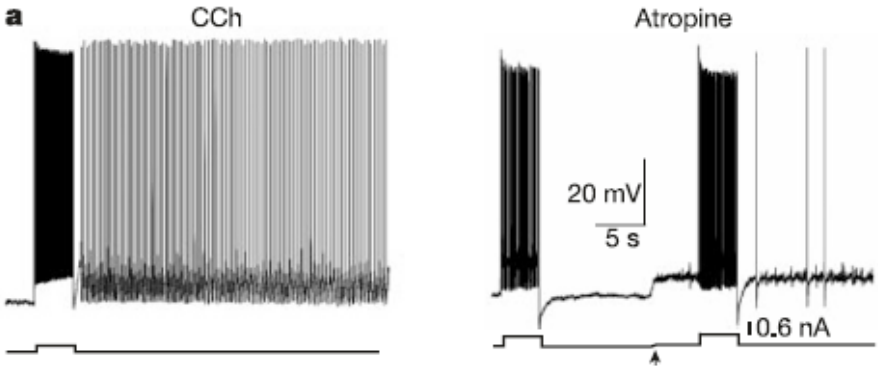

Figure 1.4.2.4: Muscarinic dependent persistent firing. **Left:** persistent firing in the presence of a cholinergic agonist (carbachol). **Right:** Lack of persistent spiking in the presence of cholinergic antagonist (atropine) (44)**.**

in bath and injecting depolarizing current lead to persistent firing that persists after ending depolarizing stimulus (35). A likely mechanism for maintained activity is cortical glutamatergic input release following stimulus disappearance during a task. This causes calcium-induced firing in the medial EC and gives feedback on cholinergic axons. Activating muscarinic receptors triggers a nonspecific cation current (I_{CAN}) and results in self-maintained persistent activity due to calcium influx (35).

Transient receptor potential channels (TRPCs) may be involved in persistent firing in layer V of the medial EC, as evidenced by the suppression of both plateau potentials and persistent firing via generic nonselective cation channel blockers and TRPC blockers (49). The next section will review TRPCs from different aspects.

TRPCs

TRPCs form a superfamily of cation-permeable channels. The founding member of this superfamily was identified as a Drosophila gene product essential for visual transduction, a phospholipase C-dependent process in the fruit fly. The title "*transient receptor potential*" originates from the transient response to light of the flies having a mutant in the *trp* locus. Moreover, *trp* mutants show a defect in light–induced Ca^{2+} influx. Based on similarities to the *Drosophila* TRP and TRPL protein sequences, the complementary DNA (cDNA) of 28 mammalian TRP-related proteins has been cloned using various methods in recent years. A diverse group of TRP-related proteins is

conserved across species, including flies, worms, fish, and tunicates (Table 1.4.2.5) (50).

TRP subfamilies	Fly	Worm	Sea squirt	Fish	Mouse	Human
TRPC	3	3	8	8	7	6
TRPV	2	5	2	4	6	6
TRPM	1	4	2	6	8	8
TRPA	4	2	4	1	1	1
TRPN	1	1	1	-	-	-
TRPP	4	1	9	2	3	3
TRPML	1	1	1	4	3	3
Total	16	17	27	25	28	27

Table 1.4.2.5: The seven subfamily of TRP genes. TRPC2 seems to be a pseudogene in humans, explaining why the human TRPC family contains six members (50).

Although crystal structures for TRP proteins remain unidentified, all TRP protein sequences include a minimum six predicted transmembrane domains (6TM) and hence look like voltage-gated k^+ channels in the general transmembrane architecture (Figure 1.4.2.6) (50).

TRPC expression

TRPCs are nonselective cation channels that comprise seven subfamilies (TRPC1–TRPC7). They are activated through phospholipase C-coupled receptors, resulting in an influx of Na^+ and Ca^{2+} into the cell. This influx depolarizes the membrane potential and initiates a Ca^{2+}-dependent intracellular signaling cascade. TRPCs can be split into three subgroups: TRPC1, TRPC4, and TRPC5 (first), TRPC3, TRPC6, and TRPC7 (second), and TRPC2 (third). The first subgroup is expressed in different areas of the hippocampus (Figure 1.4.2.7) (51), including the pyramidal layer of the hippocampal CA1–CA3 regions, the DG granule layer. Heterologous co-expression experiments show that this subgroup exhibits an intra-subgroup interaction, although some studies have reported a heterologous interplay between TRPC1 and all other TRPC families plus TRPp2 and TRPV4.

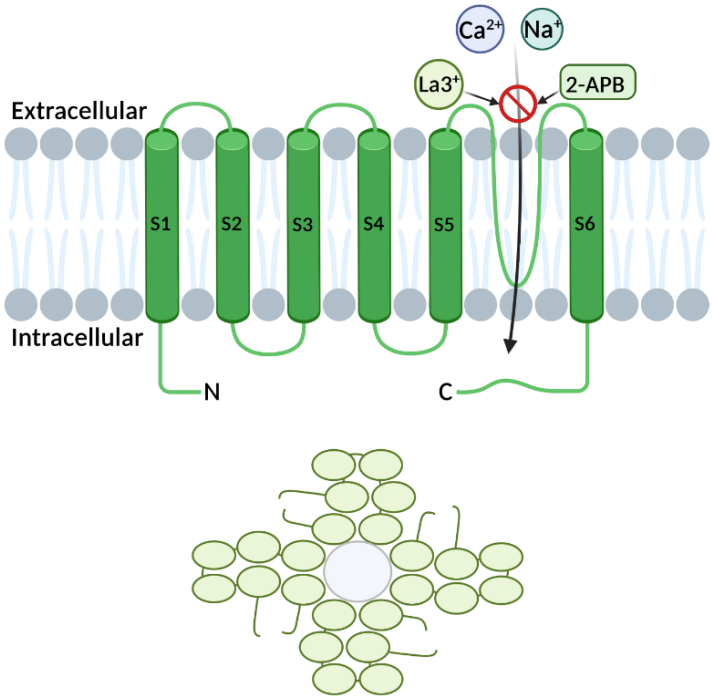

Figure 1.4.2.6: A TRP protein includes six domains (S1–S6), predicted to cross the cell membrane, and a pore loop in the extracellular linker isolating the fifth and sixth transmembrane domains. Lanthanum ions (La3+) and 2-aminodiethyldiphenyl borate (2-APB) often block these channels, but not specifically (top). Four TRP proteins are thought to form homo-oligomeric and hetero-oligomeric channel structures (bottom) (11).

Other studies have reported the formation of TRPC1 heteromultimers with TRPC4, TRPC5, TRPC3, and TRPC6 in the embryonic brain. Nevertheless, these reports are masked due to the lack of subtype-specific antibodies and strict negative controls as produced by the specific target-knockout mice (51).

TRPC4 is expressed in various organs and tissues, including the endothelium, kidney, retina, testis, and adrenal gland. The mechanisms by which it is activated may differ across these cell systems. In the nervous system, a functional role is shown in a special type of synaptic terminal of the thalamic network called F2 terminals. F2 terminals branch from the dendrites of local GABAergic interneurons and are located in a synaptic triadic positioning in a glomerular neuropil of the dorsal lateral geniculate nucleus. The release of γ -aminobutyric acid (GABA) from F2 terminals is controlled by

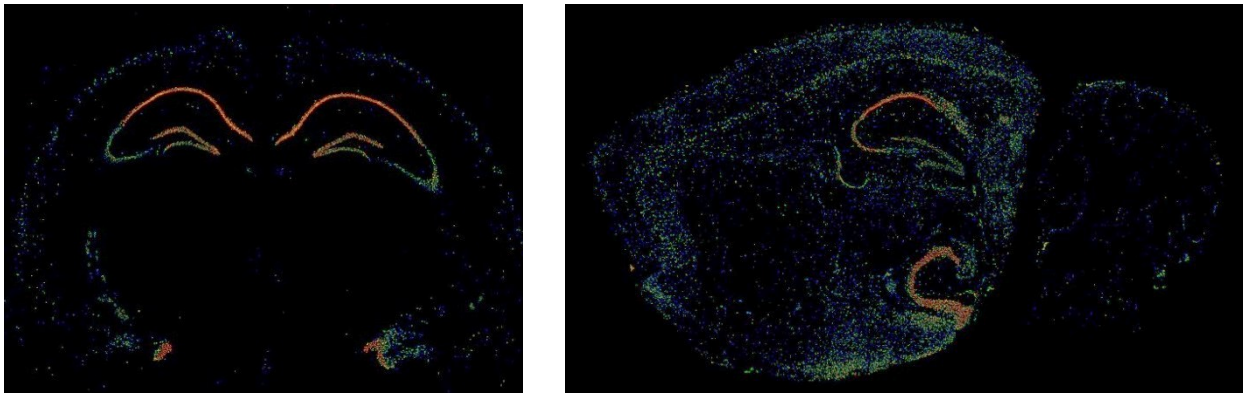

Figure 1.4.2.7: Left, TRPC4 expression in mouse coronal section. Red color shows higher expression compared to other regions. CA1 has a higher TRPC4 expression in comparison with other hippocampal areas. Right, TRPC4 expression in mouse sagittal section (52,53).

extrathalamic input systems functioning on metabotropic receptors: this release happens in a Ca^{2+}-dependent way (42).

TRPC activation and regulatory proteins

TRPCs are activated via Gq-coupled receptors, such as the group 1 mGluR and muscarinic ACh receptors. Gq/phospholipase C signaling activates TRPC 4 and TRPC 5, releasing Ca^{2+} from intracellular stores, or initiating vesicular translocation to the membrane (54). The Gq-receptor-mediated activation of phospholipase C (PLC) triggers inositol triphosphate (IP_3), which attaches to the IP_3 receptor on the endoplasmic reticulum and consequently releases the Ca^{2+}. A structural change opens a TRPC link to IP_3, which binds to the C-terminal at the end of the S6 subdomain TRPC via the Calmodulin/ IP_3 receptor binding domain (Figure 1.4.2.8 and Figure 1.4.2.9) (54).

Furthermore, PLCβ or PLCγ (or both) activation is needed to stimulate recombinant channels formed by TRPC4. While notable inconsistencies remain regarding the exact mechanism of channel activation downstream of PLC, ionic currents attributed to TRPC4 in mouse aortic endothelial cells (MAECs) and adrenal cells appear to be stimulated by the release of intracellular Ca^{2+} stores (55).

A well-known regulatory mechanism of TRPC activity is phosphorylation and dephosphorylation. Protein kinase C was reported to block the activity of TRPC3, TRPC4, TRPC5, and TRPC6. TRPC6 activity is also controlled by calmodulin kinase II (CaMK II)-dependent phosphorylation. Whether the kinase directly phosphorylates the channel remains unclear. Src kinases may be needed for TRPC3 and TRPC6 activation by the M3 muscarinic receptor and epidermal growth factor (EGF) receptor. Myosin light chain kinase is required for TRPC5 activation. Tyrosine phosphorylation controls the EGF-intervened translocation of TRPC4 and TRPC5 to the plasma membrane (PM) (56).

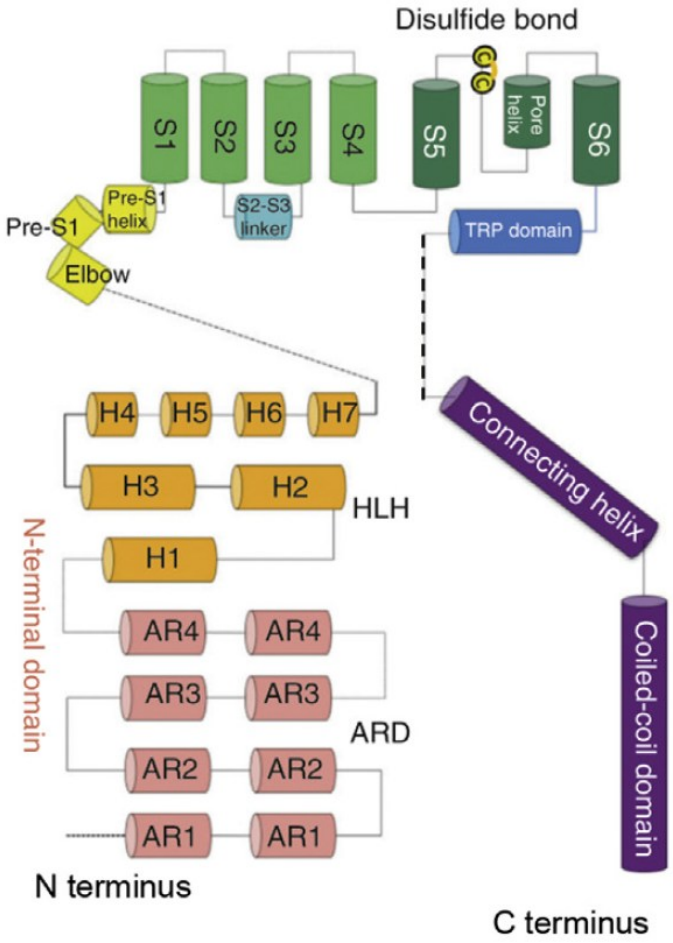

Figure 1.4.2.8: Topology and domain organization of TRPC4 (57).

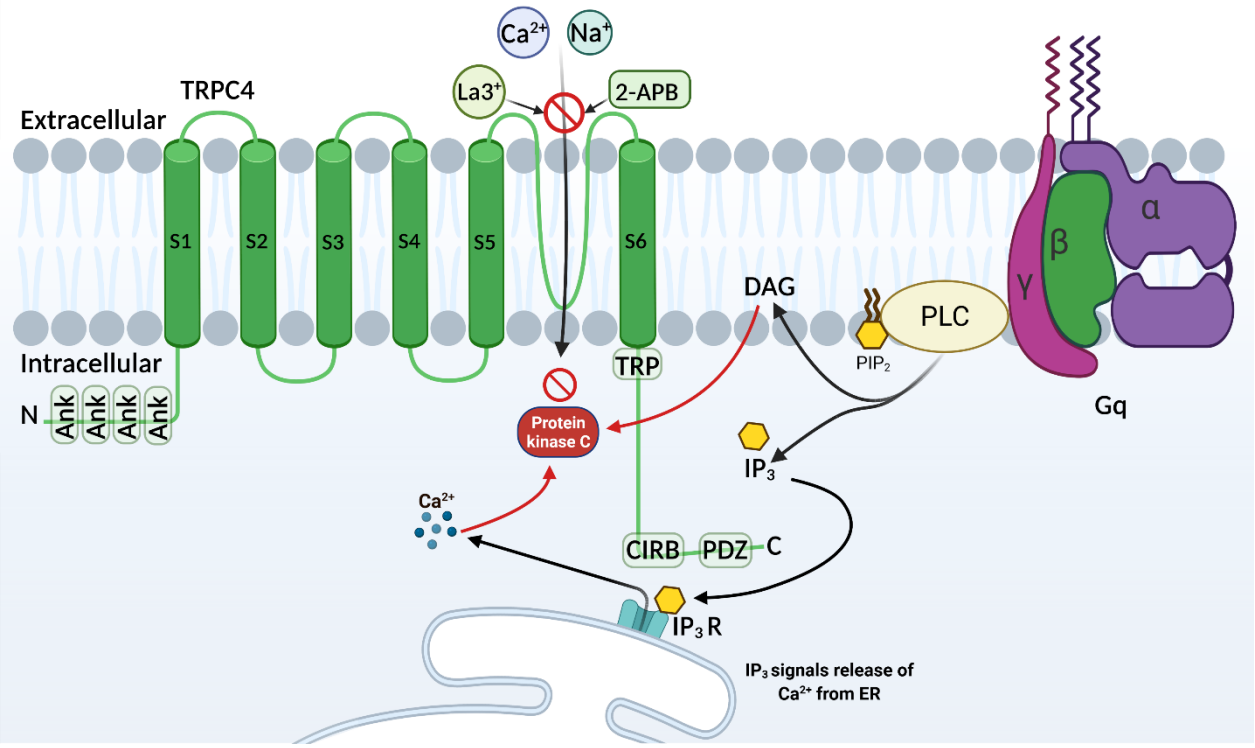

Figure 1.4.2.9: TRPC4 contains four ankyrin repeats in the N-terminus and TRP, CRIB, and PDZ domains in the C-terminus. The channel is activated by intracellular Ca2+ release from the endoplasmic reticulum (ER), triggered by Gq-coupled receptor activation, IP3 binding to IP3R, and vesicular translocation. The channel is inhibited by Protein Kinase C (PKC) and potentiated by La3+ (11).

TRPCs play a central role in Ca^{2+} signaling. Similar to other Ca^{2+} transporters, regulatory feedback loops mediated by Ca^{2+} are expected to intervene in their functions. Calmodulin (CaM), a Ca^{2+}-binding protein, is the key transporter of the cellular Ca^{2+} signal. All mammalian TRPCs encompass at least one CaM binding site at their C-terminal. The CaM binding site of TRPCs overlaps with the IP_3R binding site. It seems IP_3R and CaM compete to attach this site. While IP_3R binding activates Ca^{2+} release, CaM binding triggers TRPC inhibition. Another indirect controlling mechanism by CaM is the protein enkurin. Enkurin attaches CaM, phosphatidylinositol-3-kinase (PI3K) and

TRPC1, TRPC2, and TRPC5; therefore, it may work as an adaptor for other CaM-controlled proteins with TRPCs (56).

Roles of TRPCs in synaptic transmission

TRPCs are involved in various neuronal functions, including neuronal excitability, excitotoxicity, neurogenesis, and neurite growth. The role of TRPC1, TRPC4, and TRPC5 in synaptic transmission and neurotransmitter release remains unclear (51).

TRPC1 has been reported by Bröker-Lai et al. (2017) to generate slow excitatory postsynaptic potential (EPSP) in cerebellar Purkinje cells, as demonstrated through interference with an anti-TRPC1 antibody. In infant TRPC5$^{-/-}$ mice, synaptic plasticity was reduced at afferents to the amygdala, although this effect was not observed in older TRPC5$^{-/-}$ mice. A decrease in GABA release was observed in TRPC1/4$^{-/-}$ double knockout mice, indicated by reduced inhibitory postsynaptic currents (IPSCs) in mitral/tufted cells of the olfactory bulb (51).

In TRPC1/4/5$^{-/-}$ mice, the action potential-elicited EPSC amplitude drastically declined in hippocampal neurons, with alterations of synapse density and miniature EPSC (mEPSC) frequency in neuronal culture (51). Furthermore, a recent study reported graded changes in synaptic plasticity at glutamatergic synapses corresponding to alterations in TRPC5 expression. Further study revealed a TRPC-dependent increase and prolongation of the intraterminal Ca^{2+} signal, which speeds up the quantity of vesicle reloading, and supports short-term enhancement of synaptic signaling. Thus, TRPC-mediated mechanisms markedly alter short-term synaptic plasticity (58).

Roles of the TRPCs in persistent firing

Persistent activity (or persistent firing) has been explained in several brain regions engaged in learning processes, including the amygdala, EC, hippocampus, and PFC. Persistent firing in the hippocampus helps working memory and associative learning. It originates from burst-induced maintained depolarization, which reaches the firing threshold (59). Depolarization occurs because an activity-dependent stimulation of Ca^{2+} initiates a nonselective cationic current (CAN) (59). Activation of the CAN current can induce stable depolarization from the baseline voltage (plateau), which may persist for

several minutes beyond the initial stimulus. If the firing threshold is reached, this leads to persistent firing. Plateau persistent firing is induced by a brief depolarizing current injection in the presence of muscarinic receptor agonists or glutamatergic agonists (60). TRPCs are the primary candidates for involvement in CAN current activation. CAN channels are believed to function downstream of glutamate receptors, generating plateau potentials and increasing burst spiking (61).

Under *in vitro* conditions, persistent firing can be stimulated by a short depolarizing current using muscarinic or metabotropic glutamatergic agonist or by cholinergic afferent stimulation (59,62–64). Activation of anterior cingulate cortex (ACC) layer II/III neurons via muscarinic receptors or mGluR5 triggers persistent firing, which requires phospholipase C (PLC)-coupled TRPC-like cation conductance (65). Moreover, burst firing of numerous neurons could result in seizures. TRPC4 and TRPC1 may be key players in the mGluR-induced depolarizing plateau potential in the CA1 region, as their elimination results in impaired working memory (59). While Zhang et al. (2011) suggested that TRPCs play a key role in maintaining persistent firing in medial EC layer V (49), a study demonstrated non-involvement of TRPC family in persistent firing in layer V medial EC. The study was done using two different TRPC knockout mice ($TRPC1^{-/-}$, $TRPC4^{-/-}$, $TRPC5^{-/-}$ or all TRPC families) (66).

Studies have revealed a decline in TBS-induced long-term potentiation (LTP) in $TRPC1^{-/-}$ mice, which suggests that TRPC1 exerts its effect on TBS-induced LTP after its activation via mGluR5. The residual LTP observed in brain slices from $TRPC1^{-/-}$ mice could not be further reduced by mGluR antagonists. Despite this, strong tetanization (HFS) of Schaffer collaterals was shown to be normal in $TRPC1/4^{-/-}$, $TRPC1^{-/-}$, and $TRPC1/4/5^{-/-}$. Genetic removal of TRPC7 resulted in the interruption of HFS-induced LTP at CA3 recurrent collateral synapses and at Schaffer collaterals to CA1 synapses. This could help to start epileptiform bursts and seizures, respectively. HFS-induced LTP is decreased in $TRPC5^{-/-}$ unlike $TRPC1/4/5^{-/-}$ at Schaffer collaterals-CA1 synapses. TRPM4 has also been shown to be a crucial player in the LTP of Schaffer collaterals to CA1 synapses. TRPM4 is Ca^{2+} sensitive but Ca^{2+} impermeable, and it forms a feed-forward loop, which leads to postsynaptic depolarization. It is required to completely

activate NMDAR through LTP induction. Moreover, mGluR-LTD is weakened in TRPC1$^{-/-}$ and it corresponds to a modification of the reversal spatial task (59).

However, fMRI and neuronal recordings have demonstrated that escalated persistent activity could not distinguish the delay period of working memory unlike prosperous behavior. In addition, persistent firing has high metabolic demands and is easily disrupted by additional inputs, making it less effective at holding more than one memory simultaneously (37,67). Recently, additional mechanisms for working memory have been proposed that do not rely on persistent activity. Instead, these mechanisms suggest that short-term alterations in synaptic properties may be sufficient to retain information. The rhythmicity of neural activity during working memory is now considered the key factor for maintaining information rather than the rate of persistent activity. The frequency, amplitude, and phase of neural oscillations have been shown to vary in response to stimuli and task demands, suggesting that multiple mechanisms may contribute to the representation of working memory. These findings are not inconsistent with the idea that information can also be stored through persistent neuron firing. In fact, persistent firing measurements strongly predict behavior in working memory tasks (68).

1.4.3 Hippocampal oscillations

Introduction

Brain oscillations are known to be beneficial tools for solving neural mechanisms involved in the shaping of a memory mark (69). Local field potentials (LFP) in the theta (4–8 Hz) and gamma (25–140 Hz) frequency ranges have crucial mechanistic functions in memory. It comprises retaining events and the sequence of them, evaluation of novelty, plasticity induction in the encoding period, as well as consolidation and retrieval (70). Brain oscillations create time windows for neuron firing and facilitate synaptic plasticity. This process is achieved through the synchronization and desynchronization of neural groups (71). Jensen et al. asserted the pivotal role of theta-gamma oscillations in forming a multi-item buffer to encode sequences via LTP (72). Brain oscillations mainly depict perceptual and cognitive procedures during encoding. Moreover, these procedures could or could not be useful for memory based on how the retrieval is

performed. Thus, various frequency ranges might be associated with successful memory formation in several manners (69).

Two views exist regarding how information is encoded in the nervous system. The nervous system comprises neurons, which function as individual computing units, and these neurons interact reciprocally by transmitting distinct packets of information along their axons. Another view suggests that the nervous system operates on more comprehensive principles, with numerous cells working in harmony, possibly reflected in synchronous neuronal activity or rhythmic electroencephalographic (EEG) patterns. The general view is that the hippocampus employs both strategies. Accumulating evidence suggests that pyramidal cells in the hippocampus encode specific locations within an environment by significantly increasing firing rates. However, that piece of the code for locations engages the timing of cell firing linked to a clock wave shown by theta wave in EEG and related interneurons and those groups of pyramidal cells can function as group (1). This section addresses the main brain oscillations, hippocampus oscillation network, and what information is depicted in hippocampal electrical activity.

Hippocampal network oscillations

Hippocampal networks depict rhythmic oscillations in different frequency ranges in a behavior-associated way. Three types of hippocampal oscillatory activities have been reported in freely moving rats. Theta (5–10 Hz) and gamma (30–100 Hz) frequency oscillation rhythms are shown in rats during exploration and REM sleep (73). The frequency range has been defined differently in various studies. Theta and gamma usually coincide but can happen independently. Gamma and theta rhythms in the neocortex have been suggested to form a pivotal mechanism of cognitive tasks, such as feature recognition, associative learning, content-sensitive and context-sensitive processing of sensory information. Furthermore, periodic population bursts, sharp wave ripples (SWR; 100–300 Hz), exist in the CA3–CA1-subiculum-EC throughout awake immobility, slow wave sleep (SWS), and consummatory behaviors (Figure 1.4.3.1) (73).

Theta oscillation

Theta oscillations show the “on-line” state of the hippocampus. The extracellular currents in theta waves are produced primarily by CA3 (Schaffer) collaterals, entorhinal input and voltage-dependent Ca^{2+} currents in pyramidal cell dendrites. Theta oscillations are postulated to be essential for transient coding/decoding of active neuronal groups and modification of synaptic weights. The largest amplitude of theta is in str. lacunosum-

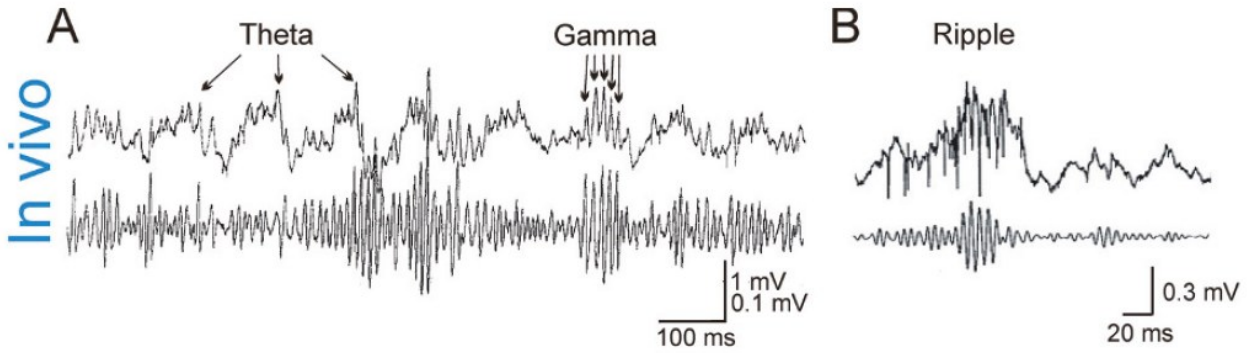

Figure 1.4.3.1: Hippocampal network oscillations. A: Theta- and gamma-related modulation in the dentate gyrus during exploration. B: Sharp wave ripples in the CA1 area during slow wave sleep (73).

moleculare of hippocampal CA1. The amplitude and phase of theta waves vary with depth changes but remain highly similar within the same layers along the hippocampus's longitudinal axis. Apart from the hippocampus, theta oscillations are present in the subicular complex, EC, perirhinal cortex, cingulate cortex, and amygdala. These structures are the major current generators of theta; however, none of these cortical structures can produce theta oscillations by themselves (74).

Hippocampal theta comprises two parts, which can be identified based on behavioral correlates and pharmacology. One is sensitive to drugs targeting cholinergic synapses, such as cholinergic antagonists (atropine and scopolamine), cholinergic agonists (carbachol), and anticholinesterase (eserine). This element is called attentional theta (a-theta) or atropine-sensitive theta. The second element of theta is not influenced by cholinergic drugs and corresponds to translational movement (t-theta). Some

evidence suggests that it relies on serotonin and glutamate. Hippocampal theta phase and amplitude changes in various parts (1).

The generation of theta oscillations in rodents involves the interaction of various brain structures. The hippocampus seems to function as a network of coupled theta oscillators, arranged in sequences along the septotemporal axis, producing moving septotemporal waves. Nevertheless, hippocampal oscillators are controlled by inputs external to the hippocampus. Both superficial and deep pyramidal cells fire in theta oscillation during active exploration but only deep pyramidal cells choose to fire at the peak of theta during REM sleep (Figure 1.4.3.2). The coherence of theta oscillation and the link between theta power and moving speed decline across the septotemporal axis (75).

Origin of theta oscillation

Multiple subcortical areas are considered pivotal for the generation of the theta rhythm. Inward projections from these areas release neurotransmitters that may permit the appearance of network oscillation in the hippocampus and related formations (“permissive action”) or might give a coherent, theta frequency output (“pacemaker” function). The inactivation or lesion of neurons in the medial septum-diagonal band of Broca (MS-DBB) eliminates theta oscillation in all cortical targets, leading to its identification as the final generator of theta rhythm. The second key nucleus involved in generating theta rhythm is the supramammillary area, which is bilaterally connected to the MS-DBB. Whether the MS-DBB and supramammillary nucleus function as true pacemakers or rely on hippocampal and entorhinal feedback remains unclear (74).

Hippocampal theta oscillations are followed by a high cholinergic tone in behaving rats. The hippocampal activity is separated from the resting state, distinguished by SWR (large irregular activity). This alteration is provoked and maintained by medial septum pacemaker activity via direct cholinergic projections to the hippocampus. There are three different populations of projecting cells in the MS identified by

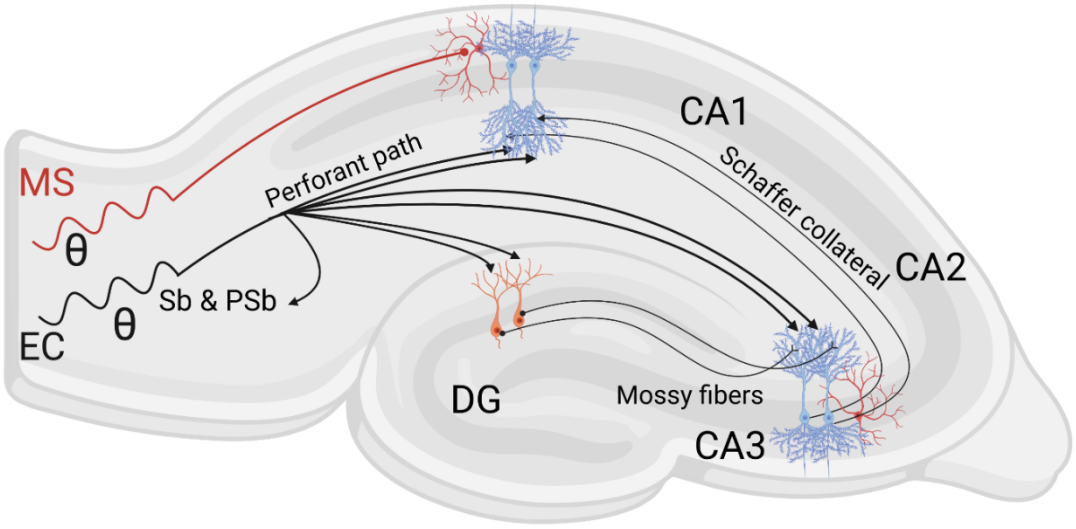

Figure 1.4.3.2: Hippocampal network controlling theta oscillation. Excitatory (black) and inhibitory (red) inputs associated with the generation of theta oscillation. The medial septum (MS) supplies rhythmic inhibitory to CA1 basket cells (red) and the basket cells in turn send rhythmic perisomatic inhibition to CA1 pyramidal cells (blue). The entorhinal cortex (EC) sends rhythmic excitatory inputs at theta frequency via a perforant path to the granule cells of the dentate gyrus (DG) and to the apical dendrites of CA1 and CA3 pyramidal cells (11).

cholinergic, GABAergic, or glutamatergic neurotransmission. Only glutamatergic and GABAergic cells showed pacemaker characteristics. MS cells fire in the negative peak of the theta signal recorded in the CA1 pyramidal layer; moreover, their firing is stopped during SWR. The MS parvalbumin-expressing interneurons projecting to hippocampal basket cells can control hippocampal activity and its feedback to the medial and lateral septum (Figure 1.4.3.3) (75). Glutamatergic MS-DBB neurons elicit fast depolarization that could stimulate spiking in hippocampal pyramidal cells; they can give a strong synchronizing input and likely help hippocampal theta oscillations if these depolarizations are rhythmic. The hippocampal theta rhythm can result from many reciprocally intrinsic and extrinsic theta generators functioning harmonically (76).

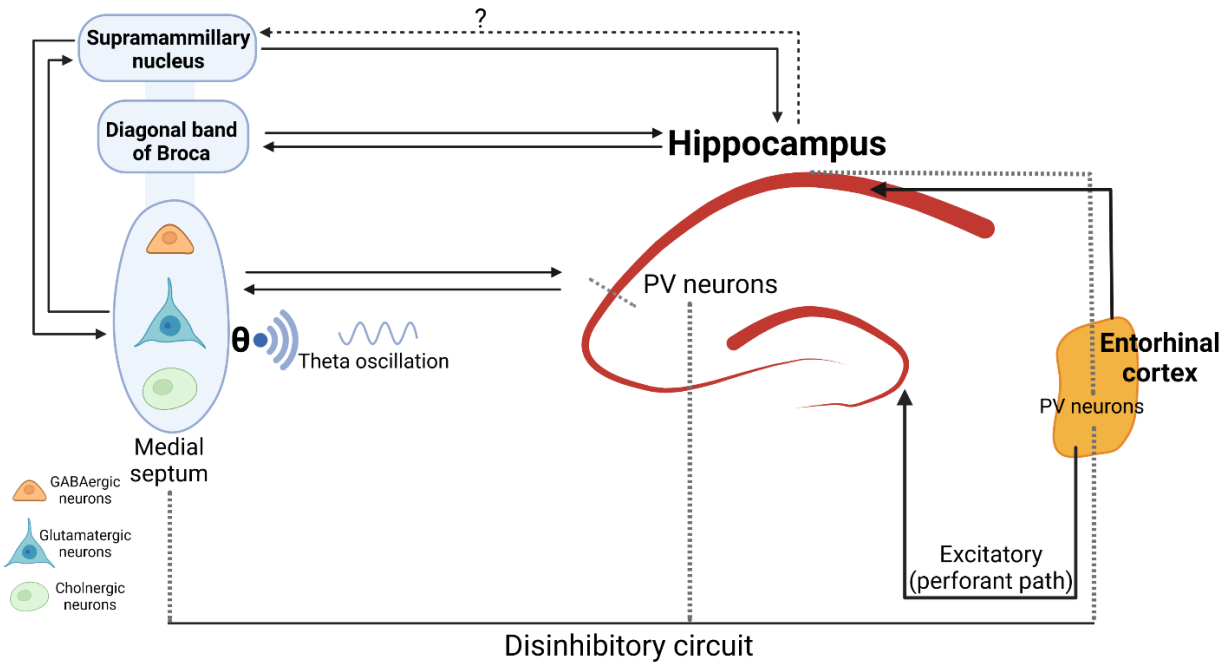

Figure 1.4.3.3: Theta oscillation generation circuit between MS_DBB and supramammillary nucleus and hippocampus and entorhinal cortex. Arrows show projections between the regions, and dashed lines represent disinhibitory network involved in theta generation (11).

Theta and entorhinal cortex

The main cholinergic projections to the hippocampal formation come from MS-DBB. Analogous input of medial septal nucleus and EC to hippocampal theta oscillation have been studied by applying lesions and pharmacological manipulations.

Lesions in the medial septum and diagonal band eliminate both the a-theta and t-theta types of theta oscillations. However, lesions in the EC abolish the t-theta while preserving the a-theta. Para-chlorophenylalanine (PCPA) or reserpine chronic administration decreases serotonin and tends to terminate t-theta. Ketamine (NMDA receptor blocker) injection also removes t-theta. Therefore, glutamatergic projections from the EC to the distal dendrites of CA3 and CA1 are likely responsible for this

component of theta. This explains why t-theta passes through the EC to the hippocampus. In contrast, a-theta requires direct cholinergic inputs from MS-DBB to the hippocampus via interneurons activation (1).

Hippocampus neurons exhibit entrainment to the theta rhythm, known as phase precession. This phase precession is believed to function as a temporal code that organizes the spikes of neurons with overlapping place fields into different sub-theta timescales. These timescales align with the working range of spike timing-dependent plasticity (STDP). Rate and temporal codes have been demonstrated to be separable and assumed to code alone for various variables in the hippocampus. While theta-modulated inputs are engaged in temporal code generation, nontheta-modulated inputs may help the rate code in the hippocampus. MEC inputs from visuospatial regions (primary, lateral, and medial visual cortical areas plus cingulate, retrosplenial and posterior parietal cortices) are stronger than those from LEC. Similarly, MEC neurons encode spatial information, while LEC neurons exhibit less or no spatial precision than MEC (77).

Functions of theta

Theta is a universal synchronizing mechanism. It locks the whole hippocampal formation into a universal operating mode and aligns every hippocampal area activity with regard to other areas. Hippocampal theta oscillation is synchronized and coherent in vast regions of hippocampus formation; this indicates that if two cells have firing patterns locked to the hippocampus theta cycle, they have organized temporal relevance to each other; it does not matter if they are in two different areas of the hippocampus. Theta also works as a periodic clock for hippocampal spike timing. The relation of a pyramidal cell to the existing theta phase is not fixed but can change from one cycle to the next one (12).

Several studies have proposed likely engagement of theta oscillation in synaptic plasticity. *In vitro* and *in vivo* studies have suggested that LTP induction is ideal when there is a 200-ms time interval between stimuli and only the second stimuli trigger potentiation. Backpropagating spikes to synapse-activated dendrites is crucial for increasing synaptic weights. Carbachol can boost the somatodendritic propagation of

action potentials via muscarinic receptor activation. LTP may be induced by triggering Ca^{2+} spikes through large-amplitude fast spikes. The associated large depolarization from Ca^{2+} spikes can, in turn, activate NMDA receptors. *In vivo*, theta-related somatic hyperpolarization may provide the silent periods necessary for the occurrence of complex spike bursts. Through theta oscillation, repeated pairing of distal dendritic depolarization by the entorhinal input and trisynaptically active CA3 recurrent/Schaffer collaterals to CA3 and CA1 pyramidal cells may lead to synaptic changes in the intrahippocampal association pathway. The occurrence of repeated trains on the negative peak of the theta will result in depotentiation. Thus, the theta cycle is pivotal for the timing of the dendritic excitatory inputs for strengthening or weakening the synapses. Buzsáki et al. proposed that theta oscillation mounts and separates neuronal ensembles (74).

Beta oscillations

The hippocampus exhibits oscillations between 15 and 35 Hz, which is known as beta oscillations (78). In addition, the hippocampus shows oscillations ranging from 20 to 40 Hz when the animal is processing odor input information (78). Beta oscillations are involved in environmental novelty and object location (79–81). NMDA and AMPA receptors modulate beta oscillation generation in the CA1 hippocampal region (79,81). Notably, the mean firing rate of pyramidal cells in CA1 increased in response to beta-band population oscillations (82).

Gamma oscillations

Berger (1929) used the Greek letters alpha and beta to name oscillations below 12 Hz and faster than 12 Hz for the first time. Later, Jasper and Andrew (1938) called oscillations between 35 and 45 Hz gamma waves. Thereafter, Das and Gastaut (1955) used cognitive rhythm or 40 Hz oscillation for that frequency range. Walter Freeman (Bressler & Freeman 1980) papers made the gamma oscillation phrase renowned (83).

Gamma oscillation was first observed in the cat amygdala by Lesse in 1995 and has since been demonstrated in various brain regions across both animals and humans. Gamma oscillations range between 20 and 100 Hz and are thought to synchronize

components of complex representations across different areas of the neocortex. Gamma waves have been reported in the dentate and entorhinal cortex and CA regions. They might be linked to visual and olfactory system oscillations (40 Hz). Cholinergic antagonists and septal lesions reduce gamma activity in rats. Physostigmine, a parasympathomimetic drug that triggers a-theta, increases the number of gamma waves, although this effect does not appear in immobile rats. Seizures cause a rapid increase in beta or gamma oscillations, which can be suppressed by cholinergic antagonists, regardless of the animal's current behavior (1).

Gamma origin

Hippocampal gamma oscillations have two origins: the first is the EC and the second is internal to the hippocampus. Entorhinal gamma wave frequency range is fast at around 90 Hz; high frequency gamma (~80 Hz) has been shown in the hippocampus. Nevertheless, a slower gamma wave (~40 Hz) is more visible in the animals with EC lesions; this slow gamma wave fits with the current profile related to the Schaffer collateral/commissural pathway from CA3 to CA1. These studies show that hippocampal gamma oscillations have many sources; this increases the chance that alterations in gamma frequency in CA1 depict synchronization change with fast gamma in EC and slow gamma in CA3. Gamma oscillations in CA1 have two distinguished frequency elements; one frequency range is slow gamma (25–50 HZ) and the second is fast gamma range (65–140Hz) (84).

Two principal mechanisms have been proposed as key players in producing and maintaining gamma oscillation. The pyramidal-interneuron network gamma (PING) model assumes that excitation of pyramidal cells leads to local connected interneuron firing. Then, this feedback inhibits pyramidal neurons, and it stops when the inhibition disappears. The second suggested mechanism is the interneuron network gamma (ING). The tonic and synchronized firing of interneurons by themselves makes them fire at their favored frequency. This causes rhythmic inhibition of the entire network. Hence, the gamma cycle length depends on the interspike interval of the interneurons. The application of carbachol (acetylcholine receptor agonist) or kainite in CA3 or mEC slices results in gamma oscillation generation; both are generated via the PING mechanism

(Figure 1.4.3.4). Gamma oscillations require $GABA_A$ receptors or AMPA/kainate receptors and NMDA receptors; blockade of either of these receptors eliminates gamma oscillations (85).

Various studies have shown the pivotal role of fast-spiking basket neurons in gamma oscillations. Basket cells have some characteristic specifications compared to other interneuron families; the first is a low spike threshold. The second is the capability to fire fast without exhaustion. Third, a narrow spike is given by a high density of Kv3.1/3.2 channels. Fourth is a resonance at gamma frequency in response to random excitatory conductance inputs.

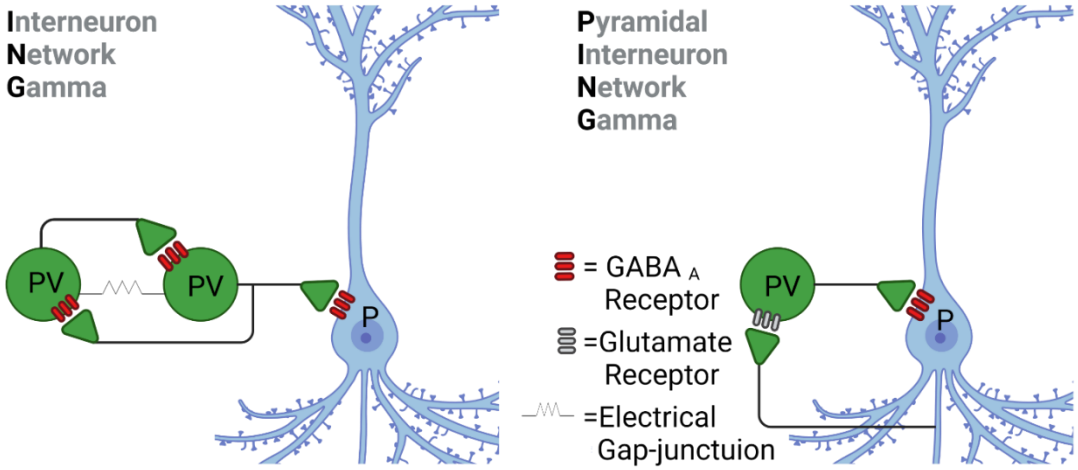

Figure 1.4.3.4: Two different mechanisms of gamma oscillation generation. Left panel: gamma oscillation is generated by a feedback network between PV-positive basket cells (PV). Tonic excitatory current is the primary source for interneuron activation in the ING mechanism. Pyramidal cells (P) are synchronized by the interneuron network but are not included in gamma rhythm generation. Right panel: In the PING mechanism, gamma oscillation depends on interneuron and pyramidal cell interaction via a recurrent network. Monosynaptic excitation (phasic) of interneuron by glutamate-mediated currents coming from pyramidal cells is an essential part of interneuron activation in PING. Thus, pyramidal neurons are key players in the gamma oscillation mechanism (11).

The participation of other interneuron types in gamma oscillation remains unclear. While chandelier cells (axo-axonic cells) are less likely to be cardinal in interneuron–interneuron (I–I) models, they project to principal cells. The somatostatin-containing O-LM interneurons connect to the distal dendrites, with their resonance frequency in the theta range. CCK interneurons are not essential in gamma oscillation maintenance. Hippocampal CA1-bistratified neurons present a powerful phase locking of spikes to gamma oscillation compared to PV basket cells. While phase locking may originate from the CA3 output, the IPSPs generated in pyramidal cell dendrites may not transition to the soma. The other types interneurons appear to support slower oscillations and, by regulating basket cells, likely play a key role in forming cross-frequency coupling between slower oscillations and gamma rhythms (83).

Functions of gamma

Gamma oscillation is thought to participate in cognition. Abnormal gamma waves have been reported in various cognitive disorders such as Alzheimer's disease and Fragile X syndrome. Gamma oscillations play a crucial role in multiple brain areas: in the hippocampus, this process contributes to attentional selection and memory functions. As hippocampal fast gamma rhythms are coupled with medial entorhinal fast gamma input, fast gamma may contribute to the transfer of current sensory information. This suggests that hippocampal fast gamma plays a role in the exploration of novel object–place pairing. Notably, hippocampal place cells can depict recent and current locations during fast gamma. Furthermore, fast gamma dominates slow gamma when mice visit external cues to navigate to a goal area (86). A remarkable correlation exists between trajectory length and the type of gamma oscillation in relation to the number of gamma cycles during a theta cycle. While the number of fast gamma cycles is positively related to path length, that of slow gamma cycles remains unchanged with trajectory length during theta cycles. The number of slow gamma cycles remains unchanged if the sequences of locations are shown within slow gamma cycles (87).

Although fast gamma power increases when rats receive stimuli signaling the start of a trial in a spatial alternation task, fast gamma may not reflect a memory-encoding

element (88). Yamamoto et al. reported that fast gamma is related to working memory but not memory encoding in mice doing a delayed nonmatching-to-place task (DNMTP). Another likely hypothesis is that slow gamma contributes to memory retrieval from CA3. Recent studies on place cell group activity suggest that slow gamma facilitates the activation of previously stored representations of spatial order, highlighting its role in supporting memory retrieval (88).

Slow gamma coupling has been reported by Carr et al. (2012) to increase between CA1 and CA3 during SWR in immobile awake rats . CA1 and CA3 become phase-locked to the same gamma rhythm, and the gamma phase accounts for the reactivation of neurons in both areas. Moreover, higher gamma coupling in awake SWR is linked with a high fidelity replay of past experience. The results suggest that gamma waves control the temporal structure of spiking during SWR in the hippocampal circuit. Gamma synchrony increases during quiescence but is lower than that of the awake state. Consequently, spiking is less regulated by gamma oscillation during quiescent SWRs. Gamma oscillations ameliorate information transmission in cortical circuits. They are present during theta oscillation but can be seen during SWRs when the animal is immobile. In addition, CA3 gamma weakly synchronizes CA1 spiking during theta (89).

Studies have suggested that hippocampal gamma oscillations assist in memory encoding (90). A later study in monkeys showed that coherence between hippocampal spiking activity and local field potentials was higher in gamma frequency during encoding of stimuli, which were well identified later. Colgin et al. (2010) proposed that fast gamma synchronization between CA1 and MEC layer III based on the connection between hippocampal gamma oscillation and memory encoding might help memory encoding. A likely mechanism for memory encoding is the timing of the primary depolarization (via depolarizing input by fast gamma) and following spiking on the next excitatory phase of fast gamma, which would result in STDP-induced LTP. This indicates that high gamma waves are perfect for information transmission of ongoing experience from the EC to the hippocampus throughout memory encoding (90,91).

Numerous studies have proposed gamma oscillations as a crucial element of working memory. The power of gamma oscillation rises by escalating the working

memory load in epileptic individuals. Another study reported theta-gamma coupling in the hippocampus through the delay period of working memory tasks. Working memory depends on different brain areas, such as the hippocampus and PFC. A study on monkeys showed prefrontal neuron synchronization at a gamma frequency range (~30 Hz) during the maintenance phase of working memory tasks. In addition, the hippocampus and PFC show an increase in theta coherence during working memory tasks, with prefrontal neurons phase-locked to hippocampal theta oscillations (90).

In addition, the gamma phase of TroPyr (trough-firing pyramidal cells in gamma cycles) and RisPyr (rising phase-firing pyramidal cells in gamma oscillations) changes differently through a theta cycle. This could be associated with various gamma differences depicted by spikes during fast and slow gamma oscillations. Nevertheless, the reported results do not support this hypothesis. Despite a reported negative correlation between fast and slow gamma power, a positive relationship was observed between the firing rates of single cells during slow and fast gamma rhythms. The results suggest that place cells are active to the same extent through either fast or slow gamma oscillations and not electively during fast or slow gamma (87).

In addition, gamma oscillations play a role in determining which cells should fire. Consequently, a representation is formed that is active in a gamma cycle (92). A study suggests that selecting which cells should fire is crucial, and the mechanism operates as a winner-take-all process driven by feedback inhibition, which primarily relies on gamma oscillations (93). The study findings revealed that if the cell suprathreshold excitation (*E*) is within the *E%* of the cell that obtains maximum excitation, cells will fire (*E%*-max). The gradual decrease in inhibition creates a gradient, effectively "searching" for the neuron with the highest excitation. The first cell to begin firing will then trigger feedback inhibition (93). This mechanism may be crucial in shaping the place cells in the hippocampus. According to the *E%* max mechanism, neurons that are excited a little more than other neurons will be selected. These neurons are winners in a proportionally small area of the environment (93). Therefore, firing in networks could not have originated from neuron excitation but from a competitive circuit computation. This suggests that the traditional textbook explanation, where excitation determines firing

(with firing being a single cell property and firing rate defined by how far excitation exceeds the threshold), does not apply in a network with feedback inhibition (93).

LIA, SIA and Ripples

Large irregular amplitude activity (LIA) and small irregular amplitude activity (SIA) are two non-rhythmical activities in the hippocampus. LIA co-occurs with ripples (100–200 Hz). The LIA has a more random template, and it is identified by sharp waves that show the spike and oscillation of the epileptiform region. High-frequency ripples occur on the LIA sharp waves. However, SIA encompasses a wide spectrum of high frequencies, and it occurs sporadically. LIA can be seen during quiet sitting, eating, drinking, grooming, and SWS. SIA does not occur often and can be seen in awake rats when the movement is suddenly stopped, transition from rest to alertness, and periods of SWS after REM events (Figure 1.4.3.5) (1).

The LIA may depict a neural correlate of memory consolidation. Each sharp wave lasts 50 to 100 ms and the maximum amplitude can reach 1 mV or more in the SR. Sharp waves occur across CA1 in the dorsal hippocampus. Buzsaki and colleagues proposed that sharp waves originate in CA3, with CA1 sharp waves representing the accumulation of extracellular EPSPs from Schaffer collaterals, which are generated by the synchronous firing of CA3 pyramidal cells. During the negative peak of the sharp wave, a high frequency oscillation (120–200 Hz) exists in which the peak amplitude happens in the CA1 pyramidal layer. Through ripple, all theta interneurons and 1 in 10 of the complex–spike pyramidal cells fire. Sharp waves are also present at the same time in the EC deep layers (5 and 6) and subiculum. Sharp wave ripples (SPW-R) rates declined following vicarious trial and error (VTE) episodes, and VTE episodes decreased following increased SPW-R rates (1,94).

Sharp waves and ripples usually coexist in local field potentials (LFP). SPW-R replays previous experiences for memory consolidation or future actions and decisions. SPW-Rs are phase-locked with a power peak in a slow gamma frequency. Nevertheless, whether the same CA1 network is involved in ripple and slow gamma oscillation remains unknown. Oliva et al. recognized three spectral elements using laminar recording. First, slow element or sharp-wave (~5–15 HZ), evoked by a

depolarizing valley from CA3 to CA1 apical dendrites, is most distinguished in the SR. Second, the ripple (130–200 Hz) has the maximum power in the CA1 pyramidal layer. The third element is the slow gamma range (~20–40 Hz). The gamma power and frequency correspond with SPW-R duration.

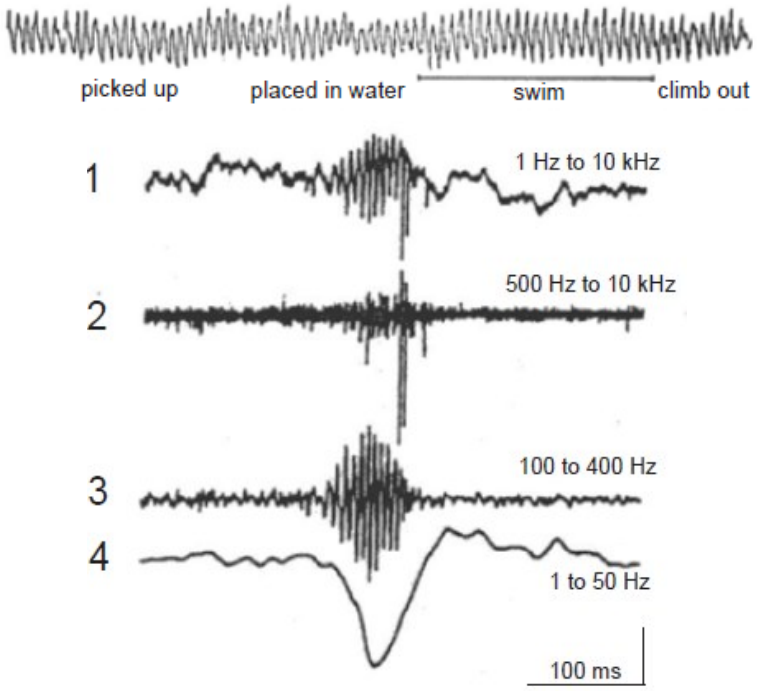

Figure 1.4.3.5: Top trace. LIA during quiet sitting. Bottom (trace 1), LIA and ripples. Bottom (trace 2–4), filtered recording. Trace 3 shows ripples, and trace 4 presents sharp waves. Trace 2 shows bursts of action potentials in hippocampal interneurons (small spikes) and principal cells (large spikes) (1).

Entorhinal Layer 2/3 neurons are active about 50 ms before the beginning of the long CA1 SPW-Rs in the awake animal. Nonetheless, the firing probability of entorhinal layer 2/3 in non-REM sleep is negatively correlated with CA1 SPW-R duration (95).

Recent studies have reported that SPW-R and theta mechanisms support memory in delayed spontaneous alternation tasks. For instance, rodents usually stay immobile in the delay area of a spontaneous alternation task, linked with hippocampal SPW-Rs. Furthermore, when SPW-Rs are artificially disturbed or prolonged, working memory performance decreases or improves, respectively (96). Awake replays may occur in both

the forward and reverse directions. Forward replay is more common in trajectory anticipation when the consultation between spatial working memory and the future path is vital. Reverse replay can be seen when the animal has reached the goal area. The results suggest an actively managed retrieval system linked to current behavior (97).

Sleep SPW-R replay is part of system consolidation. Memory consolidation during sleep is believed to require the reactivation of neural templates formed during wakefulness, facilitating synaptic changes in hippocampal-neocortical circuits. Hippocampal sleep SPW-R replay occurs during the SWS period. Several reports have shown a link between sleep SPW-R and memory using a spatial memory task. SPW-R sequences in the sleeping condition mainly replay in a forward direction, keeping the temporal order of the animal's real experience (97).

Function of Nested Theta-Gamma (Theta-gamma Coupling) in Memory

Some shapes of STM seem to be maintained by neurons that keep firing after they are activated by a short input. Hebb and others suggested that this firing is maintained by resonance of electrical activity in the neuronal circuit. Lisman et al. (1995) proposed an alternative mechanism: firing is maintained by a rise in membrane excitability, which is renewed on every cycle of network oscillation. They showed that a simple oscillatory network that combines this might store numerous STMs. A psychophysical experiment depicted that humans can keep 7 ± 2 STMs. Different memories may be stored in high-frequency oscillation (40 Hz) sub-rhythms of a low-frequency oscillation (5–12 Hz). The likelihood of this mechanism became stronger with recent evidence from the cortex and hippocampus. The observation showed that around seven high-frequency sub-rhythms are nested in a low-frequency wave. Lisman et al. (1995) proposed afterdepolarization as a putative mechanism that leads to a transient increase in excitability to store information in between cycles of theta frequency (5–12 HZ) (Figure 1.4.3.6; 1.4.3.7) (98).

Success in memory performance requires 30–100 Hz gamma coupled to a specific phase of the theta. Recent studies show that theta-gamma coupling might accelerate information transfer from the EC to the hippocampus. Triggering gamma-controlled neuronal groups in the special theta phase enables the circuit to make a stronger output

through firing neurons in a short period. Colgin (2015) proposed that this mechanism could help memory encoding or retrieval based on the gamma oscillation frequency employed. Theta-gamma coupling might permit the entorhinal–hippocampal circuit to manage the order of the events through each theta oscillation (Figure 1.4.3.8) (99). Theta-gamma phase amplitude coupling is an outstanding property of

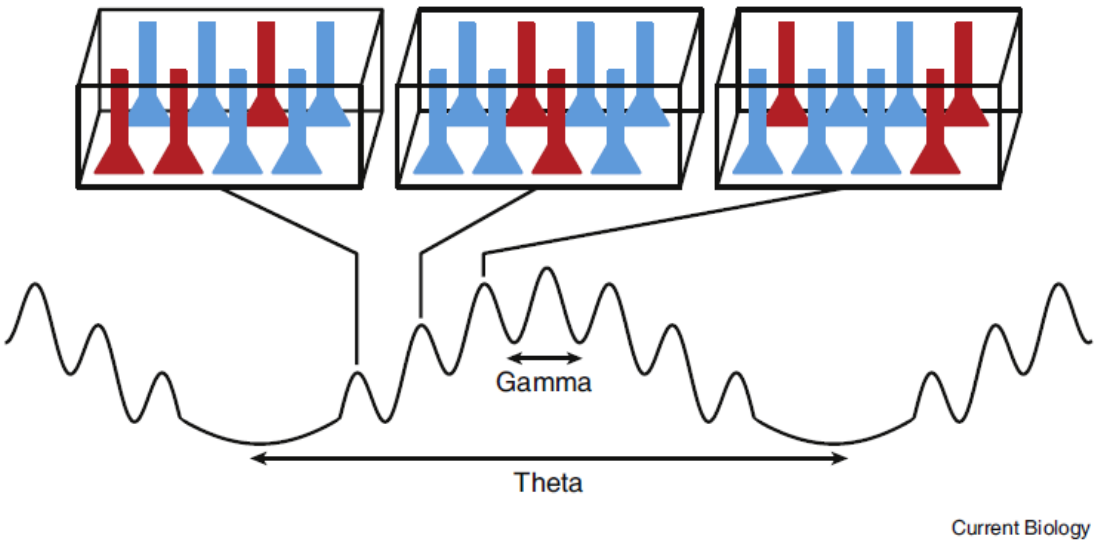

Figure 1.4.3.6: Theta and gamma nesting in working memory. Theta and gamma coupling allow numerous memories to be stored in the same network (top). Several memories (3 rectangle cubes) are indicated by different active neurons (red) that fire in various gamma cycles of the theta phase. Therefore, each memory has its own theta phase (100).

LFP activity for goal directed behaviors. The highest phase-amplitude coupling seems to occur when animals need to make a decision and behavioral choice. Phase coding may be the mechanism occurring in the hippocampus to depict locations and units in working memory (101).

A link exists between theta modulation of gamma oscillations and phase precession. Place cell firing in different theta phases represents distinct information processing. Gamma oscillation can split sensory and memory processing into discrete phases of theta. Moreover, the asymmetry of theta waves depicts

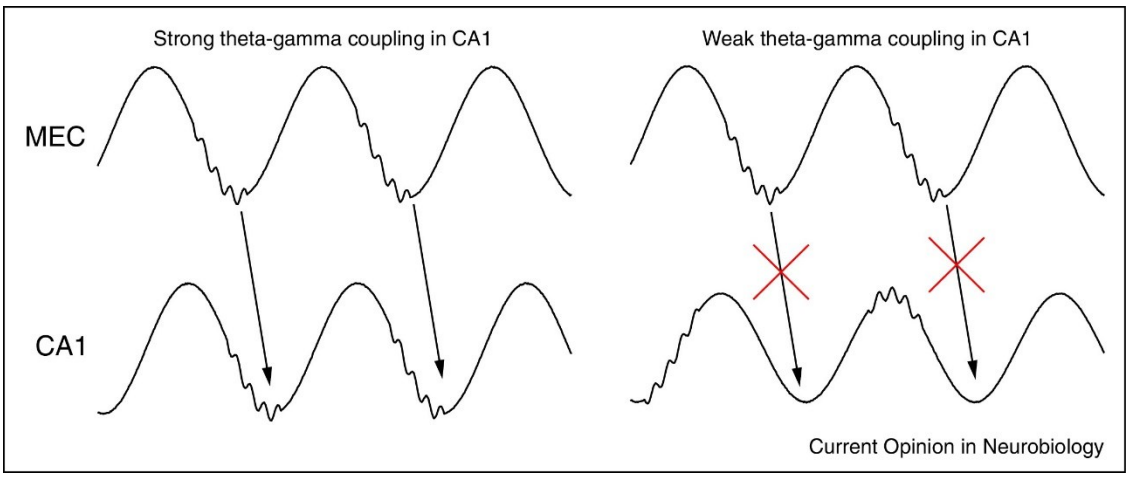

Figure 1.4.3.7: A drawing showing theta-gamma coupling between MEC and CA1. The arrows show the phase of theta in which gamma oscillation can be seen. **Left:** The aligned theta-gamma in MEC and CA1 can be observed in the high theta-gamma power coupling in CA1. Neurons are firing as soon as after about 80 Hz gamma oscillations. **Right:** Misaligned theta-gamma would result in information transfer between the areas (99).

the power superiority between high gamma and low gamma. A low gamma condition is related to future coding and high gamma with encoding of the current place (31).

Furthermore, hippocampus CA1 is coupled with fast gamma (60–100 Hz) inputs from the medial EC. Yamamoto et al. (2014) reported that high gamma synchrony from medial entorhinal to dorsal CA1 is related to successful performance in spatial working memory (102). A hippocampus CA1 spatial exhibition may be linked to external cues or to a retained sequence of neuron groups based on the spontaneously chosen behavioral plan. Deleting NMDA receptors in mice forebrain caused oscillation activity related to place cell map maintenance to change, highlighting the role of oscillations in choosing behaviorally proper computations (102).

Theta-low gamma coupling also has functional importance. During learning, low gamma (30–60 Hz)-theta cross frequency coupling increases and remains high during training in rat's CA3 area; the rate of the coupling is correlated with performance

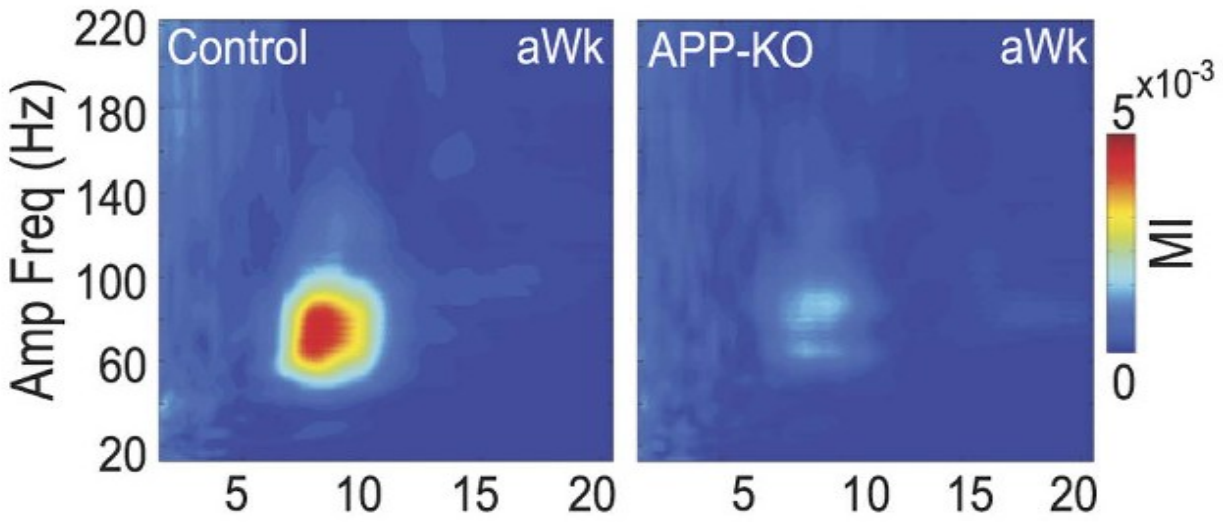

Figure 1.4.3.8: An example of theta-gamma modulation recorded from the hippocampus CA1 in awake mice. **Left:** Strong modulation of high gamma and theta in control awake (aWk) mice. **Right:** Weak modulation of theta-gamma in amyloid precursor protein (APP) knockout mice (APP-KO). APP is involved in the pathophysiology of Alzheimer's disease (101).

improvement in learning sessions (31). A study in humans revealed that coupling between 45 Hz gamma oscillations and the theta phase increased when individuals successfully recalled previously shown words in a word recognition test. Later, solid studies were shown in rodents. The coupling between the theta phase and 40 Hz gamma amplitude was enhanced when animals learned the task. Another study reported a strong phase lock of 20–40 Hz oscillation to the theta phase in CA1 when animals learned odor–place association. A study in a delayed spatial alternation task revealed 30–45 Hz gamma power increase at the decision-making point (99).

Persistent firing has an oscillatory nature and the theta (4–8 Hz) and gamma (30–100 Hz) frequencies are related to it (100). Rutishauser et al. (2010) and Fuentemilla et al. (2010) showed that oscillation sites rely on the specific information stored in humans. Moreover, the firing of single neurons occurs at a distinct phase of the theta waves. Both studies present a link between oscillatory mechanisms and prosperous memory

remembering. Theta oscillations and a second higher frequency oscillation (gamma, 30–100 HZ) enable numerous memories to fire through theta cycle while keeping the memories segregated and sequenced. Single memories are stored by the spatial order of neurons, which fire during gamma cycles accompanied by theta; several memories are activated in various phases of gamma. Memory size is restricted by the number of gamma cycles in the theta cycle (100).

A study on rats showed that firing with early theta phase indicates close positions on the forthcoming maze. Firing with the rising theta phase shows close future positions in the maze arm. Therefore, the theta and gamma allow the fast remembering of the anticipated maze segments. Several studies show the pivotal role theta-gamma nesting plays in working memory, and it signals working memory performance (100).

1.5 Involved circuits in novelty signal

The hippocampus plays an essential role in encoding memories related to new experiences and environments (79,103,104). New memories must be encoded when a remarkable difference exists between old and new experiences (105). Thus, novelty detection originates from a discrepancy between the parts of the confronted stimulus and context (106). Forming novel memories needs to be retained in cell assemblies in the hippocampus, which is distinct from previously encoded experience (105). The DG is involved in novelty detection and communicating this information to other downstream regions. However, studies suggest that the DG is also involved in detecting differences between contexts, regardless of whether they are novel or familiar (105). Other brain regions are involved in novelty and memory-shaped circuits with different hippocampal regions; the supramammillary nucleus (SuM) in the hypothalamus sends contextual novelty information to the DG (107). Moreover, the locus coeruleus projects to the DG, CA3, and CA1 (108).

Two feasible hypotheses about the source of the novelty signal are as follows: the first, ventral mossy cells (vMC) function as relays that transfer the novelty signal from various regions. The second, novelty signal is produced in ventral mossy cells from

different presynaptic inputs carrying the old and current situation (108). Ventral MC excitatory projection to granule cells is required to gain contextual memory in novel environments (108). In addition, SuM input signals to the dorsal DG are essential for contextual memory (108).

1.5.1 Role of CA1 beta oscillations

The hippocampal CA1 area plays a crucial role in novelty, and the activity varies unlike CA3 (104). CA1 place cells' firing rate increases in the presence of novel objects in new locations or moving familiar objects to different locations (79,104). CA1 may transmit the existence of novelty instead of sending what is new, and fast plasticity allows new memories to be combined with previously acquired memories (104). Regarding LFPs, distinct oscillatory conditions in CA1 have shown behavioral correlate to theta, gamma, and ripple oscillations; however, beta oscillations' functions are less investigated (80). Beta frequency oscillation power differs between novel and familiar environments (79). NMDA receptors in CA3 are pivotal for novelty-generated oscillations (79). Beta oscillation power reduces with time during exploration in a novel context (79,81,109). In addition, ACh release is associated with novelty, which is linked to beta oscillations (109,110). Beta oscillations in a novel context synchronize interneurons and create a narrow temporal window for pyramidal cells to fire about ¼ cycle (79), creating an optimal state for synaptic change (79).

1.6 Aim of the thesis

The involved mechanisms of working memory, such as neuromodulation, persistent firing, hippocampal oscillations, and long-term synaptic potentiation (LTP), are all processes that occur within the hippocampus. Our focus on TRPC4 stems from its role in supporting persistent firing in individual neurons. The role of persistent firing and other involved mechanisms through TRPC4 in working memory and *in vivo* persistent firing have not been fully explored. However, TRPC involvement in working memory has been reported by Bröker-Lai et al. (2017) (51). Underlying changes in neural activity responsive to working memory deficits remain to be understood. First, TRPCs support persistent firing in individual cells *in vitro*. However, it still remains unclear whether

TRPC supports persistent firing *in vivo* and if working memory impairment involves change in *in vivo* persistent firing. Second, the roles of TRPCs in other mechanisms of working memory, such as oscillations, remain to be studied *in vivo* during working memory. In fact, the role of TRPCs in hippocampal oscillations in awake animals remains largely unknown. Thus, this thesis explores the role of TRPC4 in working memory to understand the specific cellular and molecular mechanisms, focusing on persistent firing and oscillatory activities.

Chapter 2 Materials and Methods

2.1 Developing shRNA-TRPC4KD and Scramble

The project was started by developing an shRNA virus to knock down the TRPC4 in CA1. Oligos for TRPC4 were designed based on Puram et al.'s (2011) paper and ordered from SIGMA-ALDRICH (Figure 2.1.1, Table 2.1.1, technical datasheet) (111). Adeno-associated virus (AAV2) as a vector and U6 as a promotor were used for this project. The following protocol was used for stock primer hydration:

1. Resuspending oligos to 100 µM/L or pmol/µl.
   Oligoes tube marked from 380 to 387.
2. Calculated amount of ddH_2O was added.
3. Samples were rotated for 10 seconds.
4. To each tube, 42.5 µl ddH_2O was added.
5. T4 buffer 10X (5 µl) was added.
6. 1 µl of oligos were transferred (1 µl sense and 1 µl anti sense) to tubes.
7. 5 µl of ligase was added to each tube.
8. Tubes were transferred to a heat block at 37°C for 30 minutes.
9. Tubes were transferred to a heat block at 95°C for 5 minutes.

Second, annealing oligos was done in the following steps:

1. 49 µl ddH_2O was added to each tube.

1. 5.66 µl ddH_2O was added to the PCR tubes.
2. 2 µl diluted oligo was added to the tubes.

Oligo Name	Oligo #	Len	Pur	Scale	MW	Tm°	µg/OD	OD	µg	nmol	Epsilon 1/(mMcm)	Dimer	2ndry	GC %	µl for 100µM	Sequence(5'-3')	
Mouse TRPC4: Sense siRNA 1	8810579740-000010	61	DST	0.025	18788	83.2	31.7	13.5	429.0	22.8	591.1	No	Strong	37.7	228	GATCCGGTGGAATCTAATGGACTTTTTCAAGAGAAAAGTCCATTAGAT TCCACCTTTTTTG	380
Mouse TRPC4: Anti -Sense siRNA	8810579740-000020	61	DST	0.025	18784	82.2	31.0	11.3	350.4	18.7	605.7	No	Strong	34.4	186	AATTCAAAAAAGGTGGAATCTAATGGACTTTTCTCTTGAAAAAGTCCA TTAGATTCCACCG	381
Mouse TRPC4: Sense siRNA 2	8810579740-000030	61	DST	0.025	18790	87.5	32.3	9.3	300.5	16.0	581.5	No	Strong	44.2	159	GATCCGGTCAGACTTGAACAGGCAATTCAAGAGATTGCCTGTTCAAGT CTGACCTTTTTTG	382
Mouse TRPC4: Anti -Sense siRNA	8810579740-000040	61	DST	0.025	18786	86.3	31.5	11.4	359.2	19.1	596.1	No	Strong	40.9	191	AATTCAAAAAAGGTCAGACTTGAACAGGCAATCTCTTGAATTGCCTGT TCAAGTCTGACCG	383

Table 2.1.1: Ordered oligo sequence and technical data from SIGMA-ALDRICH

2. 1 µl oligo was added to each tube.

Third, ligation of vector and oligos was done in the following steps:

3. 0.348 µl vector was added (calculated using nanodrop).
4. 1 µl buffer was added (T4 ligation buffer NEB).
5. 1 µl enzyme was added (T4 ligase NEB).
6. Tubes were rotated.
7. Tubes were transferred to a thermocycler (defined program).

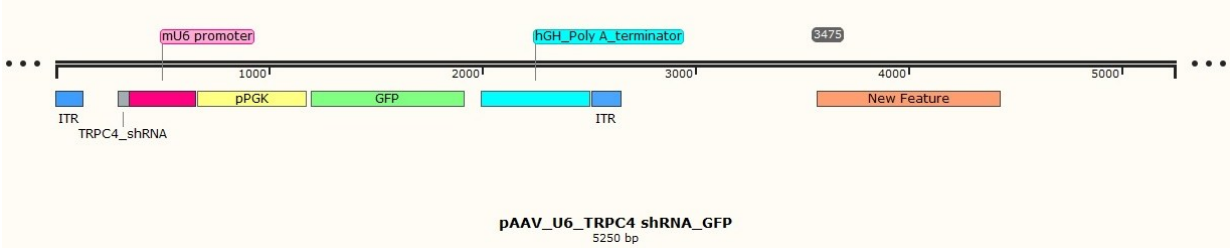

Figure 2.1.1: Linear backbone design of AAV_U6_TRPC4_shRNA_GFP virus

Fourth, transformation was done in the following steps:

1. 5 µl of ligation tubes were transferred to the new tubes.
2. 100 µl of each bacteria tube (NEB stable) was transferred to other marked tubes.
3. Tubes were kept in ice for 20 minutes.
4. Tubes were transferred to a heat block at 42°C for 1 minute.
5. Tubes were transferred to ice again for two minutes.
6. 900 µl culture media were transferred to the tubes.
7. The tubes were transferred to a heat block at 37°C, shaking at 350 RPM for 60 minutes.
8. The tubes were centrifuged at 13000 RPM for one minute.
9. Inside the laminar hood, 900 µl of tubes were removed and the remaining were mixed.

a) The remaining were transferred to Petri dish culture media, and a plastic loop was spread.
b) The Petri dishes were incubated overnight at 37°C.

Fifth, checking culture media revealed bacterial colonies in all 4 petri dishes.

Sixth, preparing mini-prep:

1. Plates were transferred from the fridge to the incubator at 37°C for 15 minutes.
1. 20 mini-prep tubes were prepared for five plates, and 2.5 ml of ampicillin culture media were transferred to the tubes.
1. 4*5 table was drowned behind the culture media, and using a wooden toothpick, the colonies were transferred to the center of the cells in the table. The wooden toothpick was placed in the mini-prep tubes.
2. The Petri dishes were transferred to an incubator and the four-culture media to a fridge.
3. The mini-prep tubes were transferred to a shaker incubator at 37°C and 250 RPM.

Qiagen miniprep kit 250 (QIA prepsin) was used in this step.

Culture test on all cells in the table was positive.

1. Culture tubes were transferred to 2 ml tubes.
2. The liquid inside the tubes was discarded.
3. Eppendorf syringes were filled with 300 µl resuspension buffer.
4. A 300 µl lysis buffer was added to the syringes.
5. The tubes were reversed 10 times to mix them.
6. 400 µl neutralization buffer was added to the syringes.
7. The syringes were centrifuged at 13,000 RPM for 10 minutes.
8. 500 µl Supernatants were transferred to spin column at first step and then 200 µl supernatants were transferred.
9. The tubes were centrifuged at 13,000 RPM for 1 minute.
10. 500 µl PB buffer was added to the tubes.
11. The tubes were centrifuged at 13,000 RPM for 1 minute.
12. The tubes' residue was completely discarded on a paper towel.
13. A 700 µl PE buffer was added to the tubes.
14. The tubes were centrifuged at 13,000 RPM for 1 minute.
15. The tubes' residue was completely discarded on a paper towel.
16. The tubes were centrifuged at 13,000 RPM for 2 minutes.

17. The tubes were transferred to a heat block at 70°C.
18. The top part of the filter tubes (spin column) was transferred to new Eppendorf tubes.
19. The tubes were left for 1 minute to dry.
20. 25 µl heated ddH_2O (70°C) was added to the center of the column (membrane).
21. The tubes were left for 1 minute.
22. The tubes were centrifuged at 13,000 RPM for 2 minutes.
23. 25 µl Heated ddH_2O (70°C) was added.
24. The tubes were left for 1 minute.
25. The tubes were centrifuged at 13,000 RPM for 2 minutes.
26. Samples were checked using Nanodrop (nucleic acid program). The blank sample was water.

Seventh, digestion test and gel electrophoresis were done in the following steps:

1. Random samples were chosen from each DNA mini-prep sample.
2. In each tube, there were 5 µl DNA sample, 2 µl fast digest green, 0.1 µl ECOR I, and 0.1 µl AgeI. This was for the samples and digestion control.
3. For the undigested control, 5 µl control digest, 2 µl FDG without ECOR I, and AgeI.
4. Samples were centrifuged.
5. In 10 tubes, 12.8 µl ddH_2O was added for digest and 13 µl ddH_2O was added for undigested tube.
6. 4 µl fast digest was added to digest (D) and undigested (UD) tubes.
7. 2 µl fast digest was added to the sample tubes.
8. 10 µl V110 were added to the UD tube.
9. 10 µl V110 were added to the D tube.
10. 5 µl mini-prep was added to the tubes.
11. 0.1 µl ECOR I enzyme was added to the sample and D tubes.
12. 0.1 µl AgeI enzyme was added to the sample and D tubes.
13. The tubes were centrifuged and transferred to a heat block at 37°C for 60 minutes.

Eighth, agarose gel preparation was done in the following steps:

1. Agarose gel was prepared using 1g agarose powder in 100 ml Tris acetate-EDTA buffer (1X TAE- buffer).
2. An Erlenmeyer flask (agarose gel mixture) was transferred to a microwave for 2 minutes.
3. 1 µl SYBR green was added (SYBR safe DNA gel stain).
4. The solution was mixed slowly.
5. After filling the gel in the well and putting two combs, 10 µl ladder was added to the wells (Quick loader 1kb DNA #N0552G).
6. 20 µl sample, UD and D were added.
7. The gel was run at 110 mV for 30 minutes.
8. After finishing gel electrophoresis, the gel was placed in a reader plate and read using UV light and a camera.

Ninth, maxiprep was done in the following steps:

1. 1L Erlenmeyer was filled with 250 ml LB media.
2. A colony using toothpick was transferred to Erlenmeyer and then it was transferred to a shaking incubator running at 37°C 250 RPM.
3. 40 falcon tubes (50 ml) were filled with Erlenmeyer.
4. Samples were centrifuged at 4°C, 4000 RPM for 20 minutes.
5. Samples were sent for sequencing. To do this, primers were diluted (1:5) and then samples and ddH_2O were added to tubes.
6. 12 ml resuspension buffer was added to tubes and mixed by pipetting and then 12 ml transferred to the next falcon.
7. A 12 ml column preparation solution was added to all vacuum tubes.
8. Vacuum was started, and 12 ml lysis buffer was added to falcon tubes. The tubes were reversed 10 times.
9. After 5 minutes, 12 ml of the neutralized solution was added.
10. The mix was transferred to a column and vacuuming was started.
11. 9 ml binding buffer was added to the falcons and then transferred to a small column and vacuumed.

12. 12 ml wash solutions 1 and 2 were added accordingly. A 20 timer was started.
13. The columns were transferred to 50 ml falcon tubes.
14. 3 ml endotoxin-free water was added to tubes.
15. The falcons were centrifuged at 3000 RPM for 5 minutes at 4°C.
16. 300 µl sodium acetate buffer solution and 2100 µl 2-propanol were added.
17. The falcons were centrifuged at 4000 RPM for 60 minutes at 4°C.
18. The liquid was discarded, and 1.5 ml 70% ETOH was added.
19. The falcons were centrifuged at 4000 RPM for 20 minutes at 4°C.
20. Ethanol was discarded, and the tubes were left to dry for 15 minutes.

Tenth, transfection was done in the following steps:

1. 7 million plate cells were prepared 2 days before.
2. Cells were checked for confluency 3 times in different areas.
3. Victor was added according to the calculation sheet.
4. DJ was added according to the calculation sheet.
5. Helpers were added according to the calculation sheet.
6. 220 µl PEI was added and was shaken on vortex.
7. 5 ml fresh DMEM media was added and was shaken on vortex.
8. The samples were incubated for 15 minutes.
9. 3 ml of mixture was added to the plates.
10. The plates were moved in 8 shapes slowly.
11. The plates were incubated at 37°C for 48 hours.
12. Media was changed after 6–8 hours with 20 ml fresh Iscove's media with 5% FBS.

Eleventh, harvesting was done following transfection in the following steps:

1. Transfection was checked under a fluorescence microscope.
2. Petri dishes were vacuumed, and 10 ml of PBS 1X was added to the wall.
3. 20 ml PS1X was added and washed with pipette tip.
4. Washed solutions were transferred to 50 ml falcon tubes.
5. The falcons were centrifuged at 1000 RPM for 10 minutes at 4°C.

Twelfth, purification was done in the following steps:

1. 5 ml buffer A was added.
2. Falcon tubes were transferred to a water bath at 37°C for 5 minutes and then transferred to dry ice for 5 minutes. This procedure was repeated three times. In the second and third times, a 3-minute water bath was applied.
3. 1 µl benzonase nuclease was added to the tubes.
4. The tubes were incubated for 60 minutes in a water bath at 37°C.
5. The tubes were centrifuged at 4000 RPM for 30 minutes at 4°C.
6. After preparing the heparin column, the pump was run with water, then buffer A.
7. After centrifuging, supernatants were removed from the filter (0.22 µ Falcon filter).
8. The filtered falcon tube was added to the pump, and speed was decreased after 5 minutes and 30 seconds; next, unbound falcon was collected.
9. The pumps were turned off and the solution changed to wash buffer 1 (WB1).
10. WB1 was collected after 6 minutes.
11. The pumps were turned off and the solution changed to wash buffer 2 (WB2).
12. WB2 was collected after 6 minutes.
13. The pumps were turned off and the solution changed to elution.
14. The solution was changed to 50 ml Milli-Q water and the column was removed.
15. 20 ml ETOH 20% was passed from the pump.
16. Filter falcons were filled with 4 ml PBS and centrifuged at 2000 RPM for 2 minutes at 4°C.
17. PBS was discarded, and 3 ml elution was added to the tube.
18. The tube was centrifuged at 2000 RPM for 12 minutes at 4°C.
19. The tube was discarded, and the remaining elution was added.
20. The tube was centrifuged at 2000 RPM for 2 minutes at 4°C.
21. The previous remaining was transferred to flow 2 marked falcon.
22. 3 ml PBS was added and centrifuged at 2000 RPM for 25 minutes at 4°C.
23. 2 ml PBS was added and centrifuged at 2000 RPM for 20 minutes at 4°C.
24. The concentrated volume was transferred to a tube.

25. A 0.22 µ Falcon filter and a syringe filled with 5 ml PBS were prepared and then piston pressed up to 1 ml.
26. The sample was filled in a 1 ml syringe and the piston was pressed to get the filtered sample in a new tube.
27. The prepared sample was aliquoted in 0.5 ml tubes and stored in an −80 freezer.

After purification, the titers were checked using q-PCR (using Taqman probes) and making different dilutions. The Titer for TRPC4_AAV_U6_shRNA2_GFP was 4.03×10^{12}, and for AAV_U6_scramble_GFP was 3.56×10^{12}.

As a final step, primary hippocampal cell cultures (PLL,200,000) were infected with TRPC4 and scramble virus to verify the effect of virus and TRPC4 knockdown. RTq-PCR was performed to check TRPC4 mRNA expression.

2.2 Animal housing

Animal research permission (TVA) was acquired from the animal committee of Sachsen-Anhanlt (LANDESVERWALTUNGSAMT, Az. 42502-2-1388 DZNE, 203.m-42502-2- 1665 DZNE). For the experiments, 12 weeks (3 months old) C57BL/6JCrl mice were ordered from the animal house about 1 week before starting the experiments and transferred to the animal room at DZNE. The animals were housed together in plastic cages with closed circuit temperature-controlled ventilation and 12/12-hour light and dark phase. Mice had ad libitum access to food pellets and water. All cages, water bottles, and environment enrichment toys (running wheel) were cleaned, washed, and autoclaved before use for the animals.

2.3 Virus Injection and Surgery

Mice were weighed and anesthetized using ketamine and xylazine cocktail prepared in sterile tubes (ketamine 20 mg/ml + xylazine 2.5 mg/ml, 0.1ml/20 gr). Around 10 min after anesthetic injection, the head was fixed in the stereotaxy (Stoelting, standard stereotaxy, equipped with a standard arm and a high precision arm) using ear bars and nose clamp. The mouse head was checked for tilting and proper fixation. The head hair was totally removed and scrubbed using Betadine (Povidone-iodine) and Ethanol 70%.

A small incision was made using a scalpel, and the tissues were retracted gently. The skull position was checked to be horizontally level without tilting to the left or right. Bregma point was used as reference, and the injection sites were marked according to coordinates from Paxinous atlas (AP: −2.1, ML ± 1.7, DV: 1.1 and AP: −2.7, ML ± 2.5, DV: 1.5). The marked points were drilled with a 0.7 mm drill tip. Using a Hamilton neuro syringe (1701, 33g needle) and stereotaxic syringe pump (CHEMYX, NANOJET) to control injection speed and volume, the virus (TRPC4_AAV_U6_shRNA2_GFP or AAV_U6_scramble_GFP) was withdrawn after thawing the tube. The needle was slowly lowered to the target site. The injection speed was 100 nl/min, and 1 ul was injected at each site. The needle remained at the injection site for 3–5 minutes before retracting the needle from the injection site.

Next, the skin was closed using veterinary surgery glue. Painkiller was added to 100 ml of water bottle and a paper sign attached to the bottle, pointing that painkiller is in the water (Metamizole, 200 mg/kg). Moreover, following surgery, a subcutaneous painkiller was injected (Carprofen, 5 mg/kg). The animal was moved to a new cage with a free running wheel, and food pellets were added to the cage. Two new soft paper tissues were placed in the cage for bedding. Mice were controlled for recovery for a few hours in the surgery room and then transferred to the animal room. They were checked every day (for 3 days) for recovery and pain management.

Microdrive implants for *in vivo* electrophysiology were implanted on the right hemisphere and lateral to the virus injection site (AP: −2.1, ML ± 1.8, DV: 0.6). Four anchor screws and one ground screw were affixed to the skull. The implant was fixed with acrylic dental cement. To verify the target sites, post-mortem histology was performed after finishing all experiments.

2.4 Behavior

2.4.1. Spatial working memory task

Mice were handled for three days and then habituated in the T-maze apparatus (OHARA Ltd., Japan) for three more days right before starting the main experiment. To motivate mice for the reward, they were food deprived with the start of handling, and the

reward pellets were introduced to them before starting the main experiment. The animal's weight was maintained between 85% and 90% body weight before food deprivation.

After handling, T-maze habituation was performed for 3 days. The experiment was started 4 weeks after injection and continued for 10 days; each day comprised 10 trials (10 sample + 10 choice phases, overall 10 trials). Each trial started with a sample trial (forced trial). The T-maze software randomly assigns the left or right door to open. The start door will be open, and the mouse should go to the open arm and receive the reward. Following it, the animal returns to the start area and waits for 30 seconds (delay time). In the choice trial, after a delay time, both left and right arms will be open and the mouse should choose the opposite baited arm in the sample trial. The choice trial delay was 30 seconds, and to start the new trial, the delay was 45 seconds. After each experiment, the maze floor was cleaned with 10 percent ethanol and the walls with water. All experiments were performed in the light phase of the mice (Figure 2.4.1.1 & Figure 2.4.1.2).

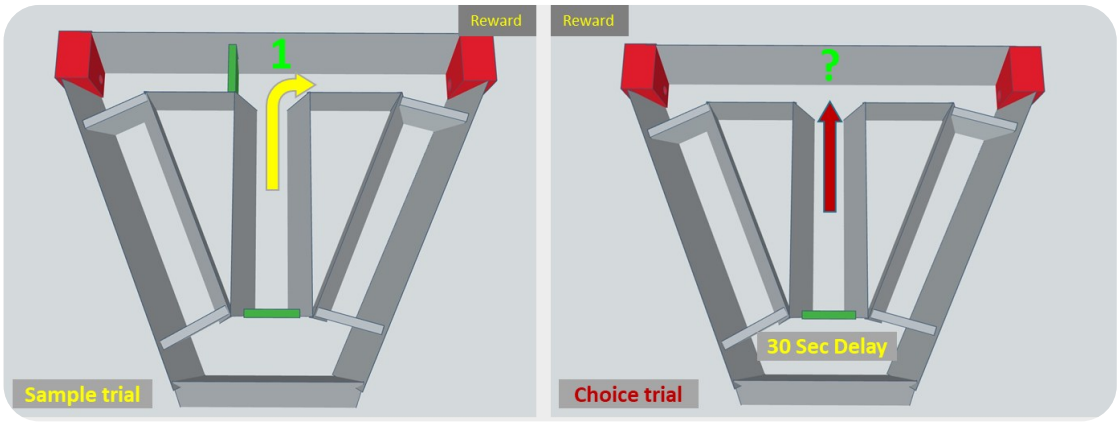

Figure 2.4.1.1: T-maze apparatus with software-controlled automated doors. **Left:** Mouse starts the sample trial with one open door (randomly chosen by software) and receives the reward at the red-colored reward area. **Right:** After returning to the start area via wayback stems, mouse waits for 30 seconds and then the door will be opened. At the end of the main stem, close to the bifurcation, the mouse should choose the opposite arm based on the baited arm in the sample trial.

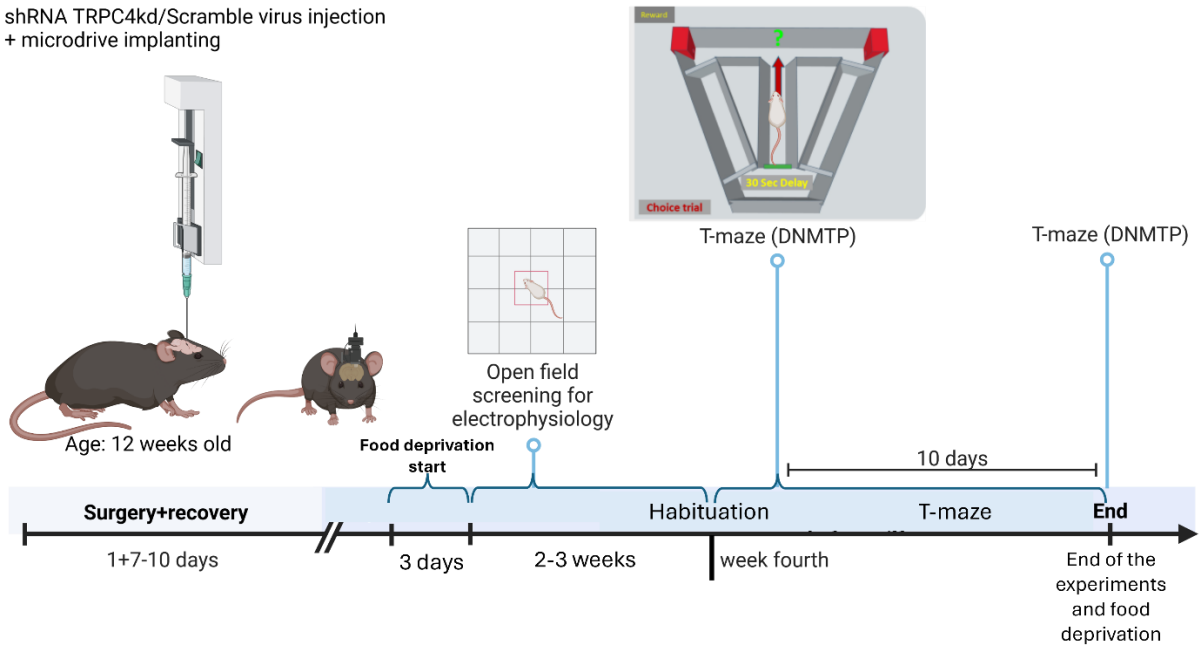

Figure 2.4.1.2: Timeline of behavioral tasks and *in vivo* electrophysiological recording. The timeline illustrates the sequence of experimental procedures performed on 12-week-old mice. Initially, the mice underwent surgery for virus injection and tetrode implantation. After a recovery period of 7–10 days, screening for electrophysiological recording commenced. Once the CA1 pyramidal layer was identified, the mice were habituated to the T-maze, followed by initiation of the T-maze task, which was conducted for 10 days. (11).

2.4.2. Novel environment and linear track

Four weeks postsurgery, the animals had become used to the reward pellets, which were introduced during the habituation phase prior to the initiation of the behavioral experiment. The animals were then exposed to a linear track (LT, measuring 70 cm in length and 10 cm in width) for the first time, allowing for an examination of their behavior in a novel context (see Figure 2.4.2.1).

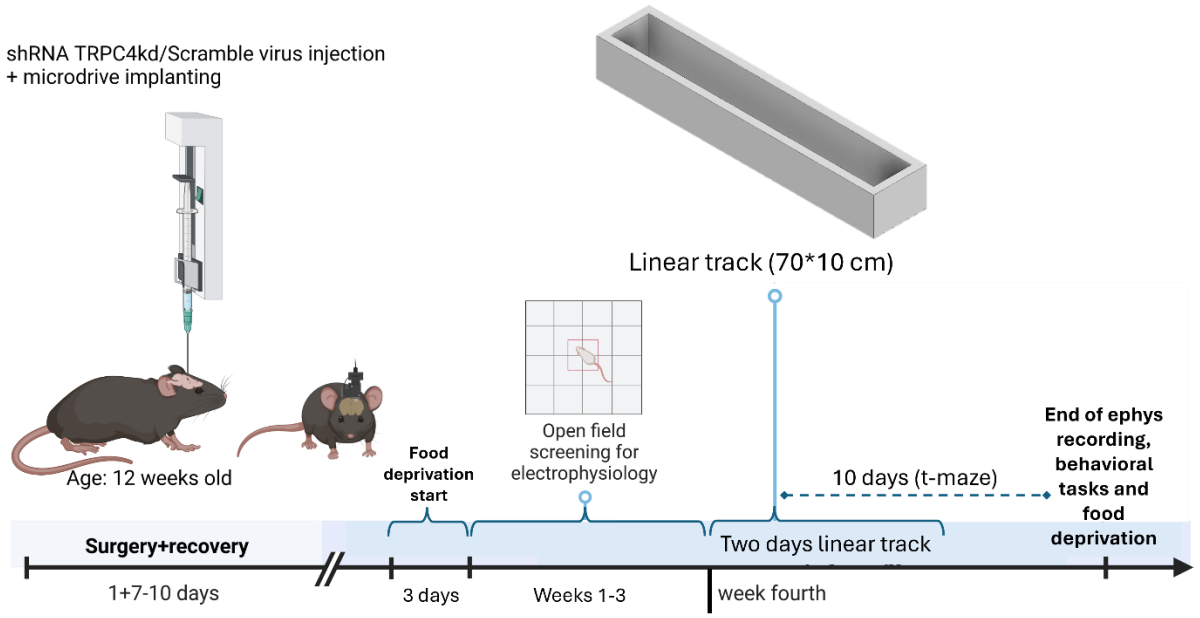

Figure 2.4.2.1: Experimental sequence for novel environment task and *in vivo* electrophysiological monitoring. The experimental sequence is depicted for 12-week-old mice, beginning with surgery for virus injection and tetrode placement. Following a 7-10-day postsurgical recovery interval, mice were subjected to electrophysiological screening to pinpoint the CA1 pyramidal layer. Upon successful localization, *in vivo* electrophysiological recordings were obtained from the CA1 region as the mice are introduced in a novel environment task (11).

2.5 Building Tetrodes and *In vivo* Electrophysiology Recording

Tetrodes were made using 12.5 µm Tungsten wire (California Fine Wire Co.). Next, Microdrive (AXONA) containing a single bundle of eight tetrodes (32 channels) was gold plated using nanoZ (White Matter LLC, USA) in gold solution to reduce the impedance to 150 kΩ.

Around 7–10 days after the surgery and after handling the animals, turning the screw and the screening of the neural activity to reach the CA1 pyramidal layer were started, and the tetrodes were lowered every day based on the screening results. For

the screening, an open field apparatus (30 × 30 cm, shielded and grounded) was used, and the signal was referenced and filtered between 400 and 8000 Hz. The data were recorded for 20 minutes to allow the animal to cover the whole arena. Next, the recorded data were clustered using Klustakwik, and the separated cells were checked to see if there were place cells and to also identify pyramidal cells and interneurons. At the end of each day, the screw was turned 1/4 of full turn on early days to lower the tetrodes, and with advancing the tetrodes, the screw turns were reduced to 1/8 and 1/16 of full turn to move the tetrodes slowly. Seeing place cells based on place field map, autocorrelation, firing frequency, and waveform characteristics was the criteria for reaching the pyramidal layer; at this step, turning the screw was stopped.

Before starting T-maze, electrophysiological recordings were performed in a linear track (LT) for 20 minutes. Next, T-maze habituation was started when tetrodes were very close to the pyramidal layer or they were in the layer. The habituation took 3–4 days. Then, electrophysiological recording and behavioral experiments were conducted together. The same T-maze protocol was applied for *in vivo* electrophysiology recording experiments.

Single unit activity and LFP were recorded using an *in vivo* electrophysiology setup (AXONA Ltd). In the main experiment days, data were recorded in raw mode with a sampling rate of 48000 Hz. The recorded raw data were then processed in Matlab software (MathWorks). Next, single unit data were band-passed (400–8000 Hz), referenced, and spikes were detected. The processed data were then clustered using KlustaKwik. Next, using Klusters software, manual clustering was performed. LFP data were band-pass filtered (2000 Hz) and then down-sampled to 2000 Hz and analyzed using a custom written script and Chronux toolbox. The power spectrums were calculated and averaged for the entire session. Moreover, T-maze data were divided into different segments using a custom-written script (Figure 2.5.1). The power spectrums were calculated and averaged for each segment based on correct and incorrect choices. The rest of the single unit and LFP analysis were done using the segmented data. Statistical analysis of the results was done using Matlab and SPSS (IBM).

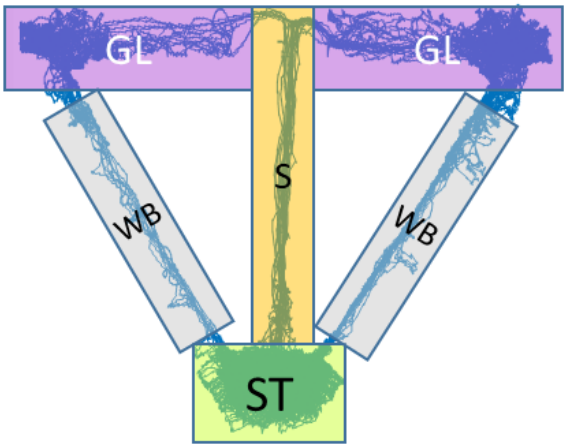

Figure 2.5.1: T-maze segments. T-maze data were divided into 6 different segments, including ST, S, GL, and WB. For the power spectrum density analysis, all three segments in the main stem were used.

Next, using a custom Matlab script, a data store for each session was created for further analysis of LFP and a single unit. Chronoux, the CMBH toolbox, and custom Matlab script were used to analyze LFP and cell classification and phase precession.

2.5.1 Power spectrum

The power spectral density (PSD) of the signal was calculated using Welch's method, a popular approach in spectral analysis. Welch's method was implemented in Matlab through the **`pwelch`** function. The **`pwelch`** function divides the signal into overlapping segments, windows each segment with a specified window function, and then computes the periodogram for each segment. The average of these periodograms forms the estimate of the PSD.

The **`pwelch`** function takes several parameters, including the input signal, the window size, the overlap between windows, and the number of FFT points. In this study, the sampling rate was 2000, with the frequency range set at 1–200 Hz. The resulting power spectrum provided a detailed view of the signal's power distribution over frequency, which was crucial for our subsequent analyses.

2.5.2 Theta-gamma coupling (Modulation index)

As mentioned before, theta-gamma coupling has been proposed as one of the working memory mechanisms. To calculate the theta-gamma coupling, the modulation index (MI) was calculated using a Matlab script developed previously based on Tort et al. (2010), which is described below. The MI could identify phase–amplitude coupling between two different frequency ranges: "phase modulating" (f_P) and "amplitude-modulated" (f_A) frequency bands (72).

The raw signal, $X_{raw}(t)$, is defined as an unfiltered signal, such as LFP. The MI is computed based on a phase-amplitude distribution generated through the following procedure:

1) Initially, $X_{raw}(t)$ undergoes filtration at the specified frequency ranges (f_P and f_A); the derived filtered signals are $X_{f_P}(t)$ and $X_{f_A}(t)$.

2) The phase time series of $X_{f_P}(t)$ (referred to as $\Phi_{f_P}(t)$) is acquired through the conventional Hilbert transform of $X_{f_P}(t)$. Similarly, the Hilbert transform is utilized on $X_{f_A}(t)$ to extract the amplitude envelope time series of $X_{f_A}(t)$ (referred to as $A_{f_A}(t)$). Subsequently, a composite time series ($\Phi_{f_P}(t)$, $A_{f_A}(t)$) is formulated to represent the amplitude of the f_A oscillation corresponding to each phase of the f_P rhythm.

3) Following this, the phases $\Phi_{f_P}(t)$ are categorized into bins, and the average of A_{f_A} across each phase bin is computed. The average A_{f_A} value at phase bin j is denoted as $\langle A_{f_A}\rangle_{\Phi_{f_P}}$(j).

4) Lastly, the mean amplitude $\langle A_{f_A}\rangle_{\Phi_{f_P}}$ is standardized by dividing each bin value by the total sum across the bins.

$$P(j) = \frac{\langle A_{f_A}\rangle_{\Phi_{f_p}}(j)}{\sum_{k=1}^{N}\langle A_{f_A}\rangle_{\Phi_{f_A}}(k)}$$

The quantity N represents the count of phase bins. Note that the normalized amplitude P exhibits properties akin to those of a discrete probability density function (pdf); specifically, *P(j)* is nonnegative for all *j* and the sum of *P(j)* for all bins equals 1.

$$P(j) \geq 0 \forall$$

$$\sum_{j=1}^{N} P(j) = 1$$

Despite P not being derived from a random variable, unlike the conventional pdf definition, I shall denote this function resembling a distribution as the "amplitude distribution." The phase–amplitude diagram is constructed by graphing *P* against the phase bin.

If no synchronization exists between the phase and amplitude of the frequencies (f_P and f_A) being analyzed, the amplitude distribution *P* across phase intervals will be uniform. In other words, the amplitude of f_A is consistent across all phases of the f_P oscillation. The presence of phase–amplitude coupling is indicated by the departure of the amplitude distribution *P* from uniformity in a phase–amplitude graph. To quantify this deviation, a measure was introduced based on the Kullback–Leibler (KL) distance, a statistical tool commonly used to assess differences between distributions (Kullback and Leibler, 1951) (112). The adaptation made in this study constrained the distribution distance measure to a range between 0 and 1. The MI proposed by Tort et al. (2010) in this context is a constant multiplied by the KL distance of *P* from the uniform distribution. Mathematically, the KL distance of a discrete distribution *P* from another distribution *Q* is formally defined as follows:

$$D_{KL}(P, Q) = \sum_{j=1}^{N} P(j) \log \left(\frac{P(j)}{Q(j)} \right)$$

The KL distance exhibits the characteristic that $D_{KL}(P, Q)$ is always ≥ 0, and $D_{KL}(P, Q)$ equals zero only when *P* is equal to *Q*, indicating identical distributions. Notably, the KL distance formula resembles the definition of Shannon entropy (H) for a distribution *P*, which is expressed as follows:

$$\mathrm{D_{KL}(P, Q)} \geq 0$$

$$D_{KL}(P, Q) = 0$$

$$H(P) = \sum_{j=1}^{N} P(j) \log[P(j)]$$

The KL distance is connected to the Shannon entropy through the following mathematical expression:

$$D_{KL}(P, U) = \log(N) - H(P)$$

The uniform distribution denoted as *U* is considered. Observe that the entropy value is maximum (*log(N))*, a condition met specifically by the uniform distribution when all bins *j* have *P(j) = 1/N*. Consequently, as *H(P) ≤log(N)*, the MI is calculated by dividing the KL distance between the observed amplitude distribution (*P*) and the uniform distribution (*U*) by *log(N)*. Therefore, the MI is calculated using the following formula:

$$MI = \frac{D_{KL}(P, U)}{\log(N)}$$

Hence, in cases where the average amplitude is evenly spread across all phases (i.e., P = U, indicating the absence of phase–amplitude coupling), the MI is equal to 0. The MI increases as the phase distribution deviates further from uniformity, a relationship that can be deduced through the KL distance. A maximum MI of 1 is achieved when the phase distribution is like a Dirac-like distribution, where *P(k)* = 1 for a specific bin *k* and *P(j)* = 0 for all other bins j. This scenario would signify an oscillation f_A that is confined to a single-phase bin of f_P and is absent in all other phase bins.

2.5.3 Spatial information

Spatial information is a quantitative analysis of the place fields. Spatial information refers to the degree to which the activity of a cell can be utilized to forecast the location of an animal. Skaggs et al. (1993) introduced a method for estimating the information rate I(R|X) concerning the relationship between firing rate R and position X (113). Cacucci et al. (2007) also used the same equation to calculate spatial information (114).

The information-rate formula is obtained by viewing a neuron as a "channel" in the information-theoretic context. Here, the input is the rat's spatial location, and the output is the spike train. In a brief time interval, the spike train can be considered a binary random variable, where the only potential outcomes are either spiking once or not spiking at all. The likelihood of spiking is influenced by spatial position. The occurrence of spiking can be denoted by a stochastic variable S, which takes a value of 1 when the cell spikes and 0 when it does not. If the surroundings are divided into distinct and non-overlapping sections, the spatial position can be described by an integer-based stochastic variable X, which indicates the index of the bin currently being occupied. In the field of information theory, the information transmitted by a discrete random variable X regarding another discrete random variable Y, which is equivalent to the mutual information of X and Y, is determined as follows:

$$I(Y|X) = \sum_{i.j} p(y_i|x_j) \log_2 \frac{p(y_i|x_j)}{p(y_i)} p(x_j)$$

In this context, x_j and y_i represent the potential values of *X* and *Y*, respectively, while $p(\,)$ denotes probability. If λ_i signifies the average firing rate when the rat is located in bin *j*, then the likelihood of a spike occurring within a short time interval Δt is:

$$P(S = 1|X = j) = \lambda_i \Delta t.$$

Furthermore, the total likelihood of a spike occurring is as follows:

$$P(S = 1) = \lambda \Delta t,$$

where

$$\lambda = \sum_j \lambda_j p_{j,}$$

with $p_j = P(X = j)$.

After substituting these terms into the equation for $I(Y|X)$ as mentioned above, the process involves applying basic algebraic operations, utilizing power series expansions of logarithmic functions, and retaining terms of lower order to obtain a discrete approximation of the equation.

2.6 Histology

Mice were anesthetized with ketamine and xylazine cocktail and transcardially perfused with cold PBS (4°C, 15 ml) and then with cold paraformaldehyde 4% (PFA, PH~7.4, 50 ml). Brains were removed and postfixed in PFA 4% at 4°C for 24 hours. After applying the cryoprotective protocol (1 day in sucrose 10%, 3 days in sucrose 30%), samples were embedded in cubic molds filled with O.C.T and then snap frozen. Next, the samples were transferred to a −80°C freezer for storage. The fixed samples were sectioned (hippocampus area) using a cryostat, and the slides were covered and mounted with mounting media. The brain section images were taken with a confocal (Zeiss, AxioImager M2) and mainly with fluorescence (Keyence, BZ-X710) microscope using 2.5x, 5x, and 40x objectives for virus expression in both experimental groups and for tetrodes trace in the hippocampus CA1 area.

2.7 Data analysis

Behavioral performance results were analyzed using Matlab (MathWorks) and SPSS (GEE, repeated measure ANOVA). Before analysis, data were checked for distribution and homogeneity tests. Statistical analysis of the electrophysiology results was done using Matlab and SPSS (IBM).

PSD between the groups was analyzed using an independent t-test. To compare sample and choice sessions in each group, and sample and choice sessions in correct and incorrect sessions as well, the Kruskal–Wallis test was used. Moreover, the Kruskal–Wallis test was employed to analyze correct and incorrect performance in sample and choice sessions. Dunn's post hoc tests were conducted between every pair of groups. Since multiple tests are being performed, the p-value was adjusted using the Bonferroni method.

The Mann–Whitney test was conducted for MI analysis between the groups. Linear regression was used to analyze MI in different segments of the T-maze for incorrect and correct choices. Linear regression was used for the correlation between MI and behavioral performance in each group.

For phase precession analysis, an independent t-test for the rho variable and circular statistics (median test) was used for phase analysis of all cells. For phase precession-positive cells, Wilcoxon signed rank was conducted for rho and slope comparison. The Watson–Williams test was used to analyze phase change between the groups in phase precession cells. Start area, main stem, and goal area rho and slope were analyzed using an independent t-test. The spike phase was analyzed using circular statistics (circular mean test).

Significance level $\alpha<0.05$ (* $p<0.05$, ** $p<0.01$, *** $p<0.001$) was used for all statistical analysis. Results are depicted as means ± SEM or median for nonparametric data analysis.

I wrote the script for different T-maze segment data analysis. The main functions were used from CMBHOME and the Chronux toolbox. The persistent firing analysis script was written by Antonio Reboreda.

2.8 Analysis Using Machine Learning

Building upon other analysis for oscillation PSD difference and cell activity properties, machine learning techniques were employed using the Machine Learning Toolbox with an Optimizable K-Nearest Neighbors (KNN). Optimizable KNN is a variant of the classic KNN algorithm that introduces additional parameters and techniques to enhance its performance and adaptability. In the standard KNN algorithm, predictions are made based on the majority class (for classification) or the average value (for regression) of the 'k' nearest neighbors of a given data point, where 'k' is a user-defined constant. However, this approach can be limited by its sensitivity to the choice of 'k' and the presence of noise or irrelevant features in the data.

Optimizable KNN addresses these limitations by incorporating optimization techniques into the model. One common approach is to use cross-validation to find the optimal value of 'k' that minimizes the prediction error. Additionally, optimizable KNN may employ feature selection or extraction methods to identify the most relevant features, reducing dimensionality and improving both the efficiency and accuracy of the algorithm. Another aspect of optimization in KNN involves the use of different distance

metrics. While the Euclidean distance is commonly used, optimizable KNN may explore other metrics such as Chebyshev, Correlation, City block, Cosine distance, Mahalanobis, Hamming, Jaccard, Minkowski, and Spearman distance. This can lead to better separation of classes or more accurate regression predictions. Furthermore, optimizable KNN can benefit from advanced weighting schemes, where the influence of each neighbor on the prediction is weighted based on its distance to the target data point. This can help mitigate the impact of less relevant neighbors and improve the overall performance of the model.

In summary, an optimizable KNN enhances the classic KNN algorithm by incorporating optimization techniques for parameter selection, feature engineering, distance metric learning, and neighbor weighting. These improvements make optimizable KNN a more robust and effective tool for both classification and regression tasks, particularly in complex datasets with high dimensionality or noise.

Chapter 3 Results

3.1 Development of TRPC4 shRNA Virus and Verification

In this study, I used the TRPC4 shRNA virus to study the role of TRPC4 in spatial working memory. After developing the virus for this purpose, which was mentioned in the method section, the effect of the shRNA virus on TRPC4 expression was verified in primary hippocampal cell culture (PLL, 200000) using RT-qPCR. The cell cultures were divided into three groups (Control, Scramble, and TRPC4) and infected using scramble and TRPC4KD shRNA. The cell cultures were incubated at 37°C for 14 days. After 14 days, cells were collected and RNA was isolated from cells, and RT-qPCR was done to assess the TRPC4 expression in the groups. Gel electrophoresis was performed to confirm RNA extraction. A significant difference was observed in TRPC4 expression between TRPC4-14 and the two groups, Scramble-14 and Control-14 (CTRL) (ANOVA with Sidak post-hoc, p = 0.003 and p = 0.042, respectively) (Figure 3.1.1). This result shows that TRPC4 expression decreased in the TRPC4 group compared to the scramble and control groups, confirming the knockdown effect of TRPC4 shRNA.

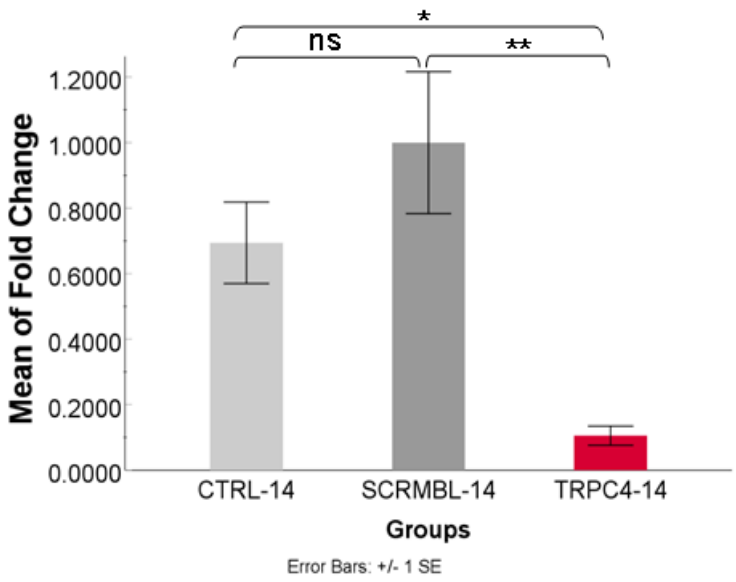

Figure 3.1.1: Fold change in TRPC4 expression in primary hippocampal cell cultures. TRPC4 expression was verified using RT-qPCR on day 14 (n = 5 for control, n = 5 for scramble, n = 5 for TRPC4KD; *=p<0.05, **=p<0.01).

3.2 Behavioral Performance of TRPC4-KD Mice

To study behavioral impairment of TRPC4 knockdown, a hippocampus-dependent T-maze task was used to assess the spatial working memory performance. "Scramble" represents the group with scramble shRNA virus (control) and “TRPC4KD” represents the group with TRPC4 shRNA virus injection (experiment). Rats and mice like to alternate for the novel goal arm. Alternating represents the motivation of an animal to explore the environment and locate food (115). The spatial working memory task (DNMTP) was started 4 weeks after bilateral virus injection. Seven mice were assigned to each behavioral group. For electrophysiological experiments, seven mice per group were assigned, and one mouse was excluded from scramble (ephys groups). For purely studying the effect of TRPC4 knockdown on behavior, I did only the behavioral T-maze task as the first step. Next, electrophysiological recording was started after observing working memory impairment in the pure behavioral groups. Then, behavioral results of microdrive-implanted animals were added with pure behavioral results. The time course of the percentage of the correct trials illustrates that the control animals (scramble) learn to alternate in choice phases and improve their performance compared to the first day of trial. In contrast, the TRPC4KD group performance was lower and failed to improve. The scramble group had significantly higher performance than the TRPC4 group. A significant difference existed between groups on days four, six, eight, and ten (Figure 3.2.1).

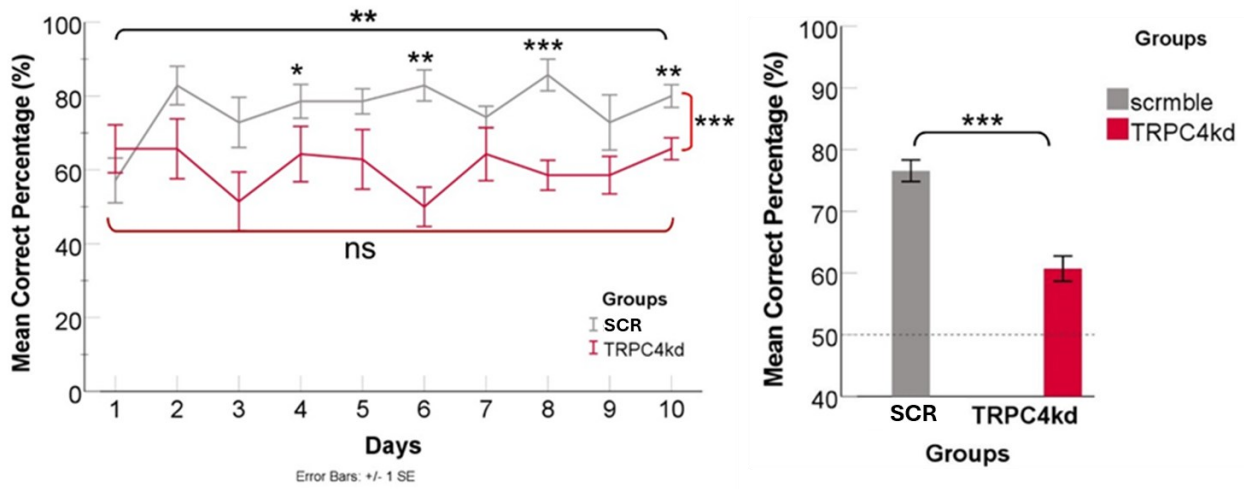

Figure 3.2.1: Mean correct performance of scramble and TRPC4KD. **Left:** Mean performance of the groups per day (day one mean ± SEM = 58.571 ± 5.832, day ten mean ± SEM = 80.0 ± 3.030, n = 7 for scramble; day one mean ± SEM = 65.714 ± 5.832, day ten mean ± SEM = 65.714 ± 3.030, n = 7 for TRPC4KD). Group mean comparison (two-way ANOVA, $p<0.001$). Single-day comparison four, six, eight, and ten (Bonferroni, $p=0.024$, $P=0.006$, $p<0.001$, $p=0.003$ respectively). Day one and ten comparison (one-way ANOVA, $p = 0.008$ for scramble, $p = 1.000$ for TRPC4KD). **Right:** Mean performance the groups (mean ± SEM = 77.0 ± 2.247, n = 7 for scramble, mean ± SEM = 59.7 ± 3.815, n = 7 for TRPC4KD). * SCR: Scramble group.

Moreover, behavioral data of microdrive-implanted animals for *in vivo* recording were added to pure behavioral data (Figure 3.2.2). The scramble group demonstrated significantly higher performance than the TRPC4KD group (ANOVA, $p<0.001$) (Figure 3.2.2). Comparison of days between groups showed significant differences on days two, three, four, six, seven, eight, nine, and ten (Figure 3.2.2).

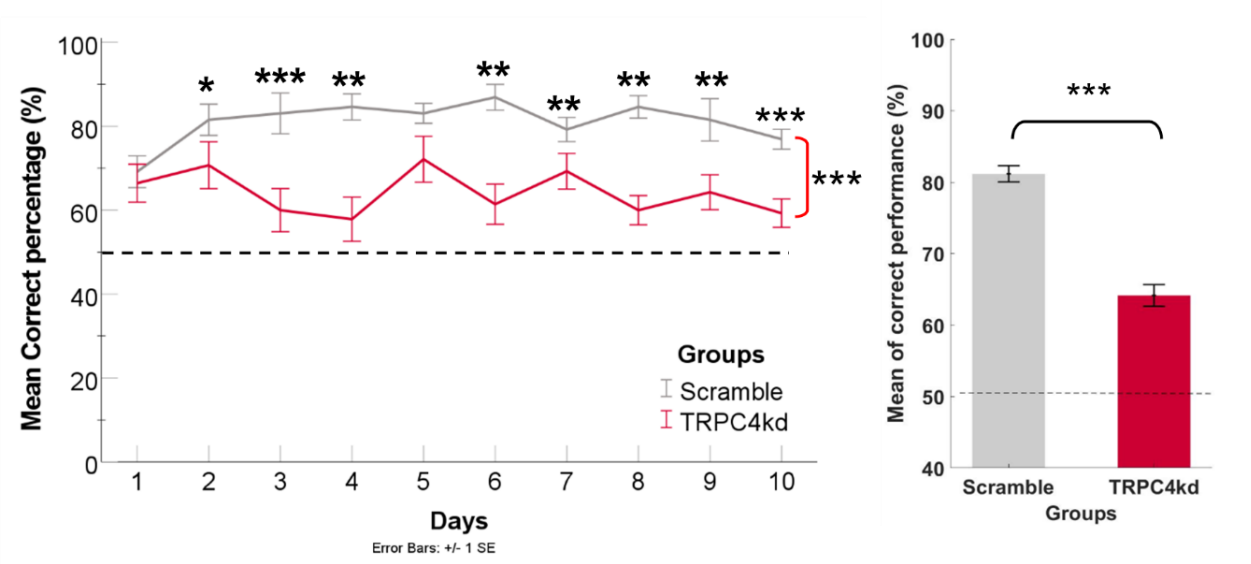

Figure 3.2.2: Mean correct performance of scramble and TRPC4KD. **Left:** Mean performance of the groups per day (two-way ANOVA, Bonferroni, $p<0.001$ between the groups, $p=0.030$ for day two, $p<0.001$ for day three, $p=0.010$ for day four, $p=0.010$ for day six, $p=0.006$ for day seven, $p=0.003$ for day eight, $p=0.002$ for day nine, $p<0.001$ for day ten). **Right:** Mean performance of the groups (mean ± SEM = 81 ± 1.07, n = 13 for scramble, mean ± SEM = 64.0 ± 1.41, n = 14 for TRPC4KD).

The spatial working memory task performance was evaluated over the first two days for both groups. The aim was to study task paradigm learning. In the scramble group, a notably improved performance was observed by the end of the first day, which was successfully retained on the second day (panels A and B of Figure 3.2.3). Conversely, the TRPC4KD group exhibited a more erratic, zigzag pattern of learning, with performance dropping on the subsequent day (panels C and D of figure 3.2.3). This difference in learning patterns between the groups highlights the potential impact of TRPC4KD on spatial working memory processes. It also demonstrates the learning of the task paradigm in scramble.

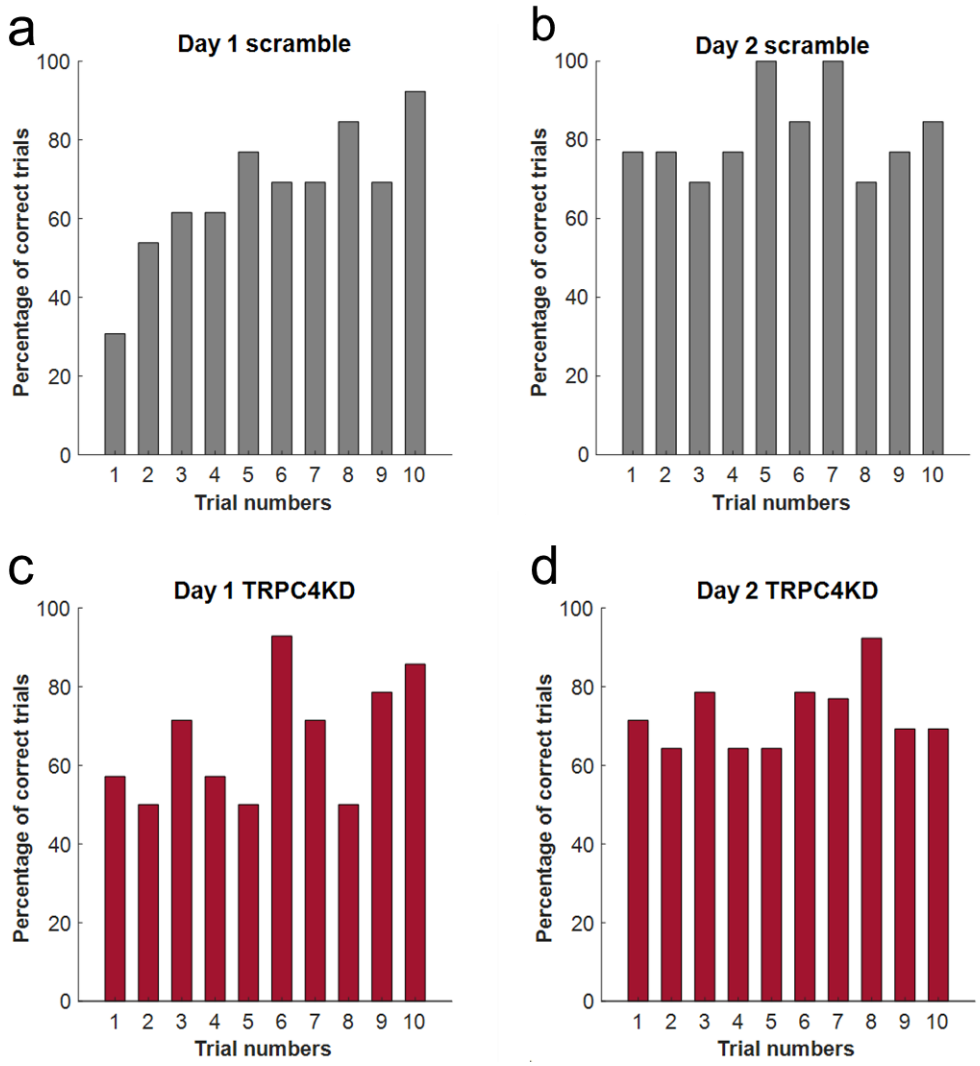

Figure 3.2.3: First two days of the spatial working memory task performance in both groups. **A & B:** Improvement in performance by the end of the first day and retention of the task paradigm on the second day in the scramble group. **C & D:** TRPC4KD group showing a zigzag pattern of learning with a drop in performance on the next day (n = 13 for the scramble, n = 14 for the TRPC4KD).

3.3 LFP Analysis

3.3.1 Power spectrum density analysis

LFP represents the postsynaptic activity of local neurons. As mentioned in Chapter One, LFP could correlate with memory processes and different behaviors. Oscillations including theta (6–12), beta (15–29 Hz), low gamma (30–55 Hz), and high gamma (65–100 Hz) are correlated with memory functions such as encoding, consolidation, and retrieval. Thus, LFP analysis could provide insights into brain oscillations in an interested region related to the animal's current engaged task and its performance. LFP and single unit data were recorded simultaneously during a spatial working memory task (T-maze, DNMTP). To measure the PSD mean in the groups, all trial means were calculated separately.

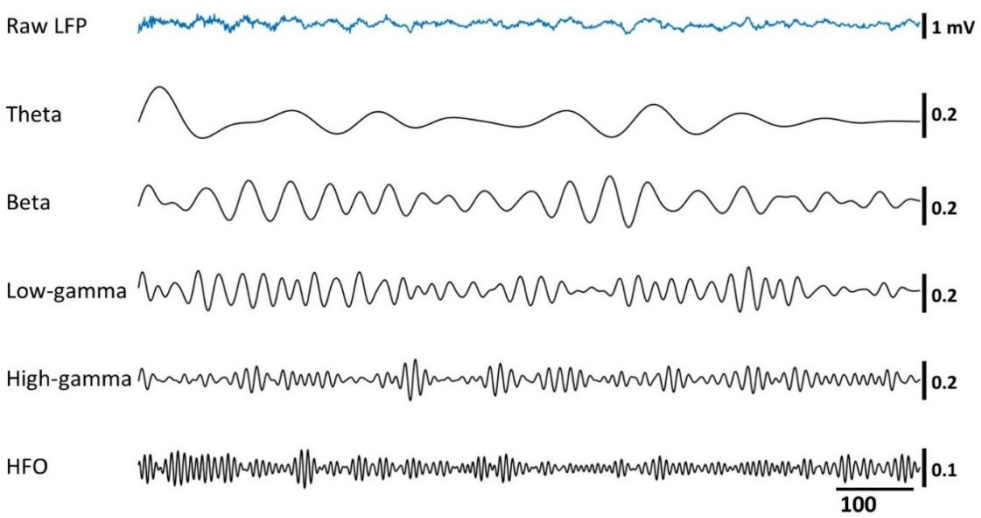

Figure 3.3.1-A: Local field potential (LFP) and a band-pass filtered LFP showing various oscillatory patterns such as theta (6–12 Hz), beta (15–29 Hz), low gamma (30–55 Hz), high gamma (65–100 Hz), and high-frequency oscillations (100–150 Hz).

The mean power spectrum comparison between groups showed no differences for theta, beta, low gamma, and high gamma frequency (Figure 3.3.1 & 3.3.2). Notably, the power spectrum depends on various factors, such as the experimental group, signal

amplitude, and animal movements. Next, to study in detail the power spectrum change in the T-maze segments, the recorded electrophysiology data were divided into segments including start (ST), main stem (S), and goal area (GL).

Furthermore, LFP data were filtered based on the main group (scramble or TRPC4kd), T-maze segments, trial performance (correct or incorrect), and session type

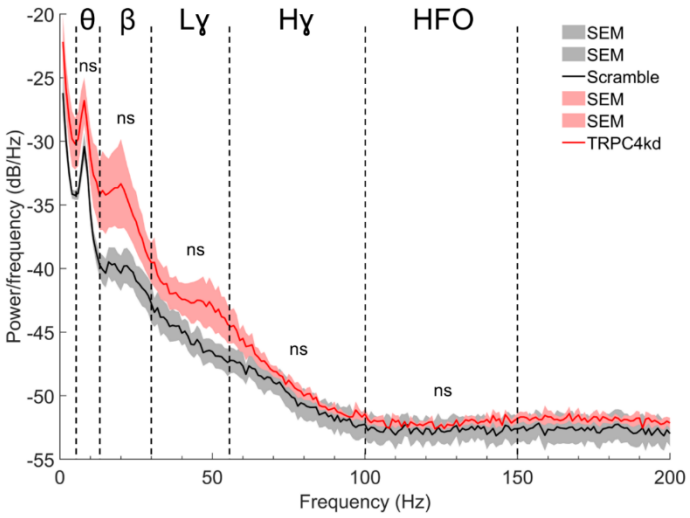

Figure 3.3.2: Power spectrum (0–200 Hz) mean of LFP in scramble and TRP4kd groups recorded from the CA1 layer of mice. Power spectrum density between groups was analyzed using the area under the curve for each specific frequency range. Theta: 7–12 Hz, Beta: 15–29 Hz, Low gamma: 30–55 Hz, High gamma: 65–100 Hz, High frequency oscillation (HFO): 100–150 Hz. No significant differences were observed in oscillation bands between the groups (Mann–Whitney Exact (2-tailed), p=0.534 for theta area; t-test two-sided, p=0.563 for beta area; t-test two-sided p, p=0.915 for low gamma area; t-test two-sided, p=0.547 for high gamma area; t-test two-sided, p=0.0666 for HFO area; scramble n = 6; TRPC4KD, n = 7). The shaded area represents ± 1 SEM. ns: not statistically significant

(sample or choice). The LFP data of all sorted groups underwent statistical analysis utilizing the Kruskal–Wallis test followed by Dunn's post hoc test for group comparisons. The results revealed a statistically significant difference between the groups ($p < 0.001$, total n=57764). However, upon conducting Dunn's post hoc pairwise group comparison

for each oscillation band, no significant differences were observed between the groups within individual frequency bands. This suggests that while an overall significant distinction existed among the groups based on the LFP data, the specific oscillation bands did not display significant variations when comparing the groups individually. These findings highlight the nuanced nature of the group differences across different frequency oscillations, emphasizing the importance of comprehensive statistical analyses in elucidating distinct patterns within complex neural data (Figures 3.3.3, 3.3.4, 3.3.5, 3.3.6, 3.3.7, and 3.3.8). Despite statistical analysis, the beta oscillation difference between the main groups was noticeable (Figures 3.3.6, 3.3.7, and 3.3.8). Beta oscillations are involved in novelty and elevated in exploration, but locomotion has no effect on it (72). The change in beta oscillation power may be related to the exploration of the animal.

Building upon the previous analysis, machine learning techniques were employed using the Machine Learning Toolbox with an optimizable KNN. Specifically, PSD data of beta oscillations during the stem (sample and choice phases) were leveraged to predict the main groups, distinguishing between the "scramble" and "TRPC4kd" groups. The power spectrum of beta oscillations was calculated for all trials. The area under the curve for beta oscillations, trial phase (sample or choice), and performance (correct or incorrect) were used as features for training the machine learning model. Data from a total of 13 mice were used, and sample sizes were adjusted to ensure equal representation in each group. The main groups (scramble and TRPC4KD) served as predictors in the trained model. Notably, a subset comprising 15 percent of the data was reserved for testing purposes. The predictive model achieved an impressive accuracy rate of 84.3%, indicating a robust capability to differentiate between the two main groups based on the beta oscillation patterns (Figures 3.3.9 and 3.3.10 left). This outcome underscores a significant distinction in beta oscillations between the "scramble" and "TRPC4kd" groups, suggesting that these neural frequency patterns play a pivotal role in characterizing and potentially distinguishing the underlying neural mechanisms associated with each group. The ROC curves (Figure 3.3.10 left) are depicted with two operating points, each with an area under the curve (AUC) value of 0.9045. This AUC

value is a measure of the model's ability to discriminate between the two classes, with a value closer to 1 indicating a more accurate model. The ROC curve plots the true positive rate (TPR) against the false positive rate (FPR) at various threshold settings. The TPR (Figures 3.3.9 and 3.3.10 left) represents the proportion of actual positives that are correctly identified, while the FPR represents the proportion of actual negatives that are incorrectly identified as positive. The first operating point (class) has a TPR of 90.7% and an FPR of 9.3%, while the second operating point has a TPR of 77.8% and an FPR of 22.2%. These points suggest that the model is more sensitive to the positive class at the first operating point, potentially making it a better choice if the priority is to minimize false negatives.

In summary, the ROC curves illustrate the trade-off between the model's sensitivity and specificity, providing a visual representation of the model's performance across different thresholds. The AUC values of 0.9045 for both operating points indicate that the model has good discriminative power. The successful prediction rate of 84.3% underscores the discriminative power of beta oscillation patterns in elucidating the differences between the "scramble" and "TRPC4kd" groups. This high prediction accuracy indicates a robust relationship between the beta oscillations observed in the CA1 area at the stem and the experimental groups under investigation.

To verify the accuracy of the trained network, the response feature was randomized 1000 times, and the trained network was used to test the accuracy of randomized data (Figure 3.3.10 right). Furthermore, the distribution of accuracy from randomized data was compared to the main accuracy of the network (sample T-test, ($p<0.001$)). The statistical analysis reveals a significant difference in prediction accuracy compared to the prediction accuracy of randomized data, confirming the trained network performance.

Beta oscillations are associated with the synchronization of neural activity and communication between brain regions involved in memory tasks. In the context of working memory, beta oscillations are believed to facilitate the maintenance and manipulation of information over short time intervals (116). Studies have suggested that

the coupling of hippocampal beta oscillations with other brain regions supports the encoding and retrieval of information in memory-guided decision-making (117).

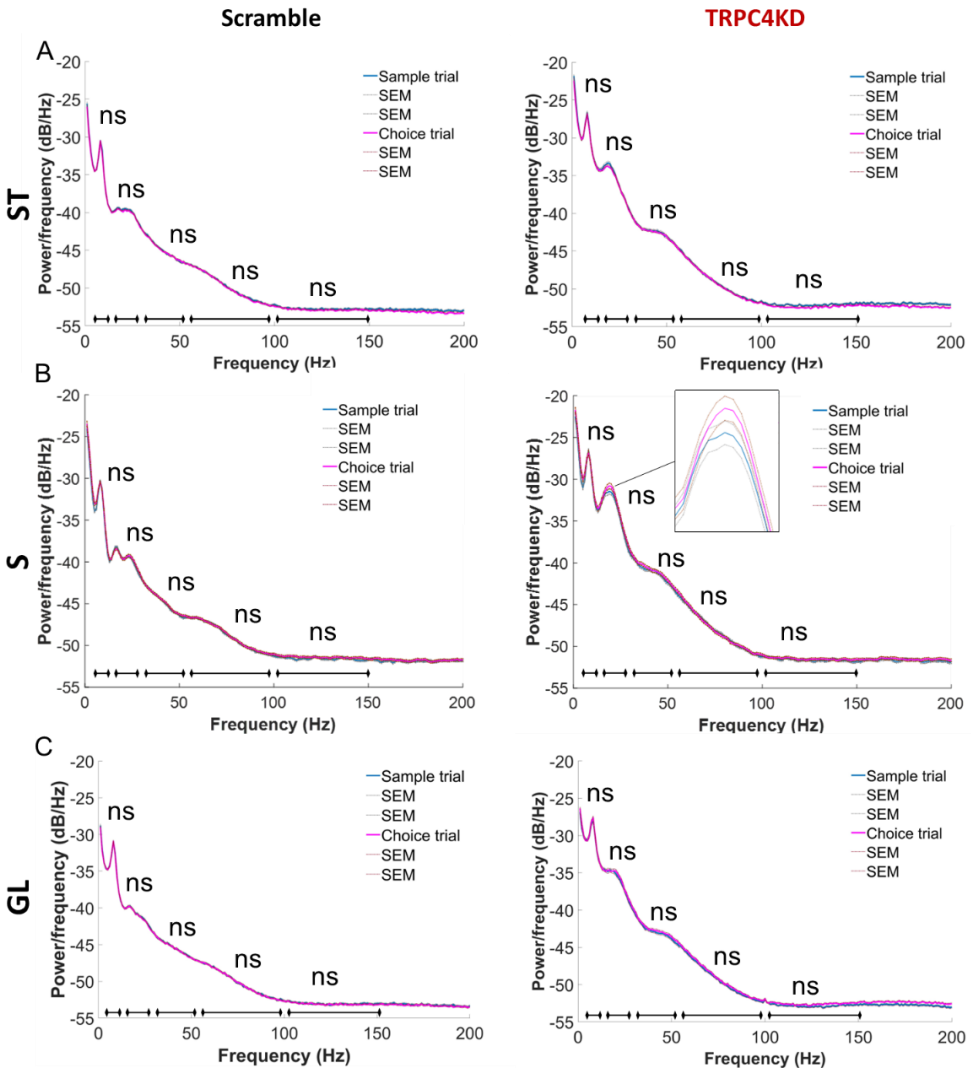

Figure 3.3.3: Power spectrum (0–200 Hz) of LFP recorded from CA1 of mice in T-maze segments comparing sample and choice phases. The black divider lines on the X-axis show divided frequency bands. **A:** left: Power spectrum in the ST segment between sample and choice phases for scramble. Right: Power spectrum in the ST segment between the sample and choice phases for TRPC4kd. **B:** left: Main stem power spectrum between sample and choice phases in scramble. Right: Main stem power spectrum between the sample and choice phases in TRPC4kd. **C:** left: Goal area power spectrum between sample and choice phases in scramble. Right: Goal area power spectrum between the sample and choice phases in TRPC4kd. n = 590 for scramble and n = 696 for TRPC4KD in each defined frequency range. The dashed lines represents ± 1 SEM. ns: not statistically significant.

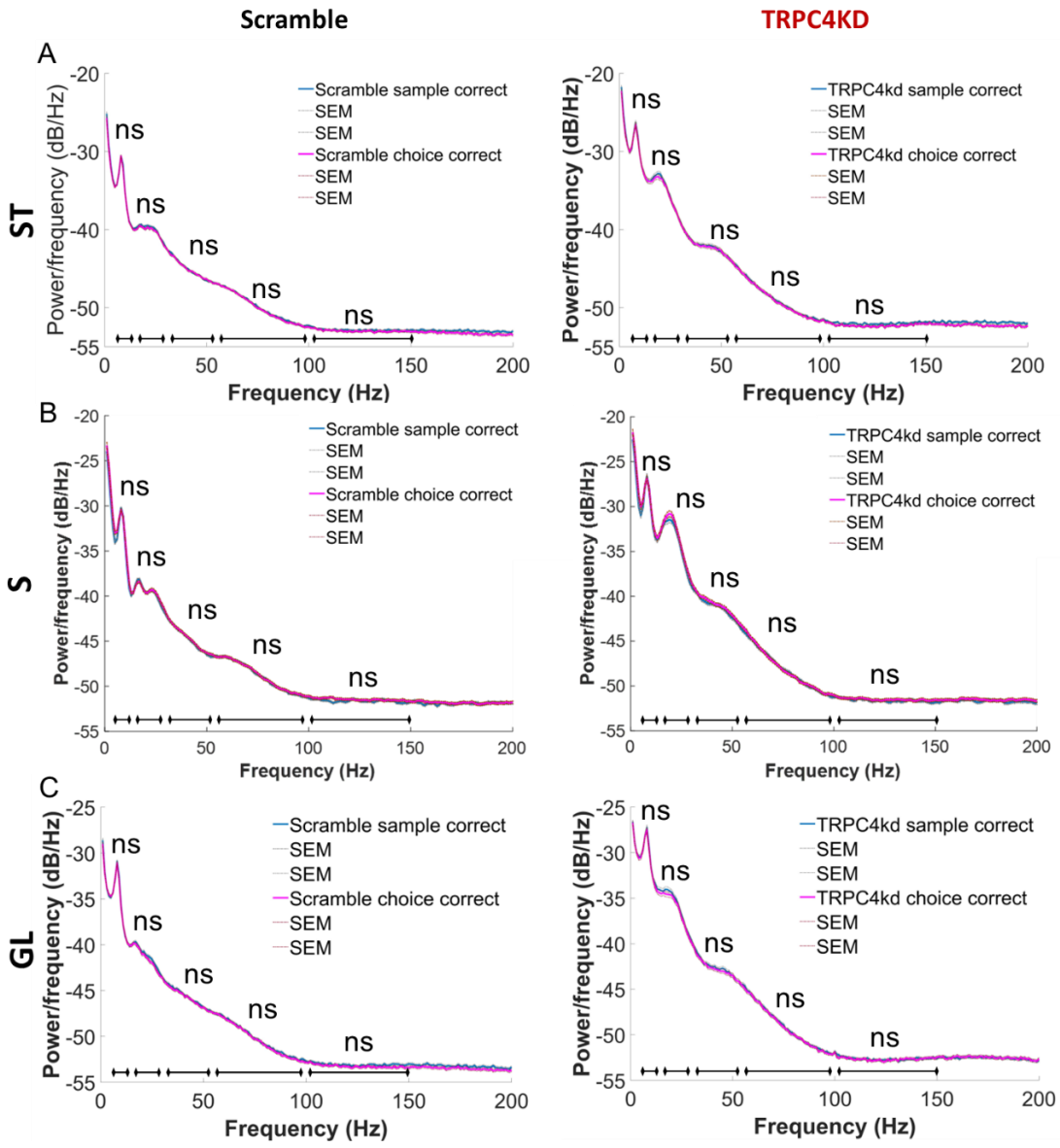

Figure 3.3.4: Power spectrum (0–200 Hz) of LFP recorded from CA1 of mice in T-maze segments comparing sample correct and choice correct phases. The black divider lines on the X-axis show divided frequency bands. **A:** left: Power spectrum in the ST segment between the sample correct and choice correct phases for scramble. Right: Power spectrum in the ST segment between the sample correct and choice correct phases for TRPC4kd. **B:** left: Main stem power spectrum between the sample correct and choice correct for scramble. Right: Main stem power spectrum between the sample correct and choice correct phases in TRPC4kd. **C:** left: Goal area power spectrum between the sample correct and choice correct phases in scramble. Right: Goal area power spectrum between the sample correct and choice correct phases in TRPC4kd. n = 500 for scramble and n = 478 for TRPC4KD in each defined frequency range. The dashed lines represents ± 1 SEM. ns: not statistically significant.

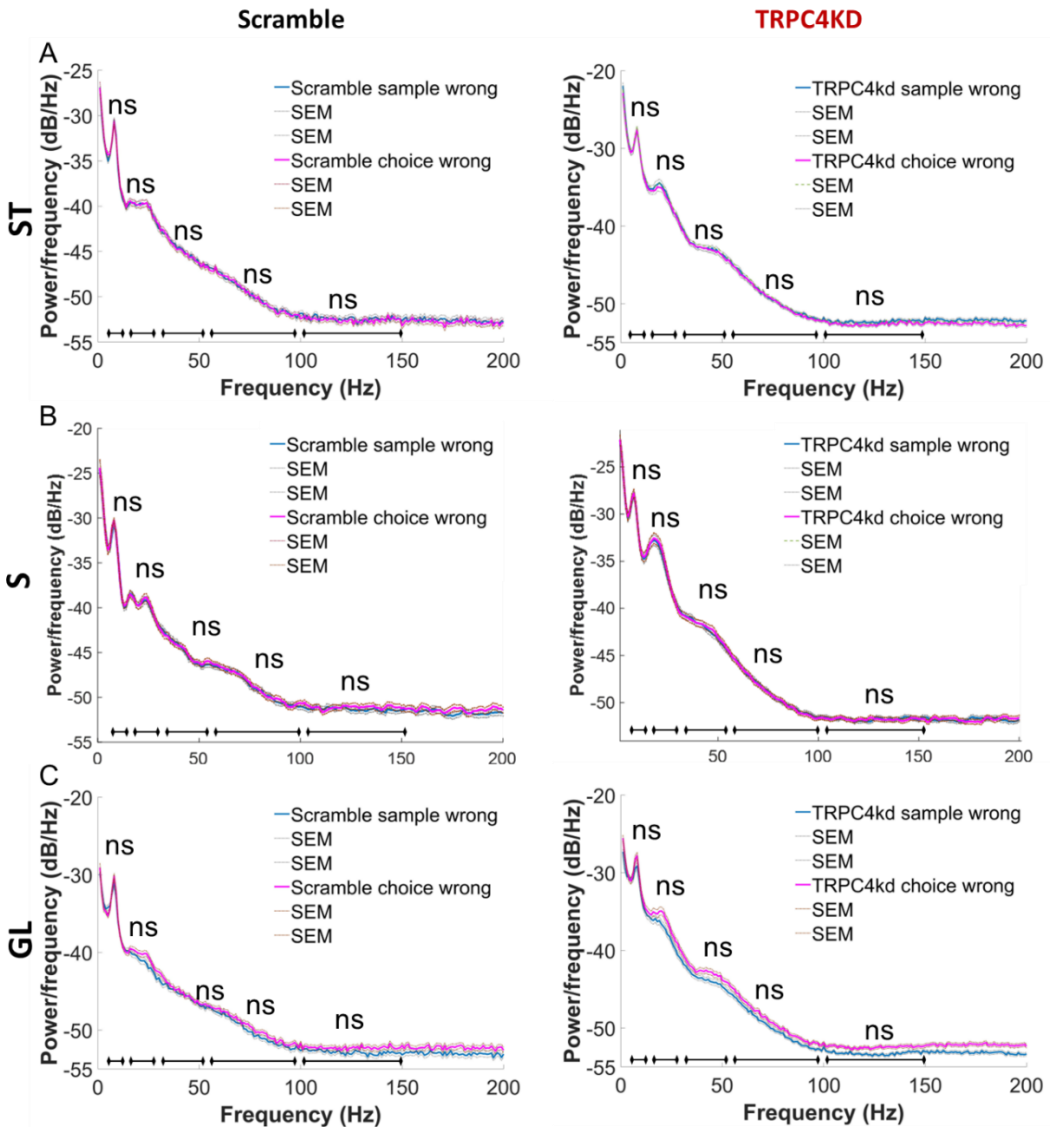

Figure 3.3.5: Power spectrum (0–200 Hz) of LFP recorded from CA1 of mice in T-maze segments comparing sample incorrect and choice incorrect phases. The black divider lines on the X-axis show divided frequency bands. **A:** left: Power spectrum in the ST segment between the sample incorrect and choice incorrect phases for scramble. Right: Power spectrum in the ST segment between the sample incorrect and choice incorrect phases for TRPC4kd. **B:** left: Main stem power spectrum between the sample incorrect and choice incorrect phases for scramble. Right: Main stem power spectrum between the sample incorrect and choice incorrect phases in TRPC4kd. **C:** left: Goal area power spectrum between the sample incorrect and choice incorrect phases in scramble. Right: Goal area power spectrum between the sample incorrect and choice incorrect phases in TRPC4kd. n = 90 for scramble and n = 218 for TRPC4KD in each defined frequency range. The dashed lines represents ± 1 SEM. ns: not statistically significant.

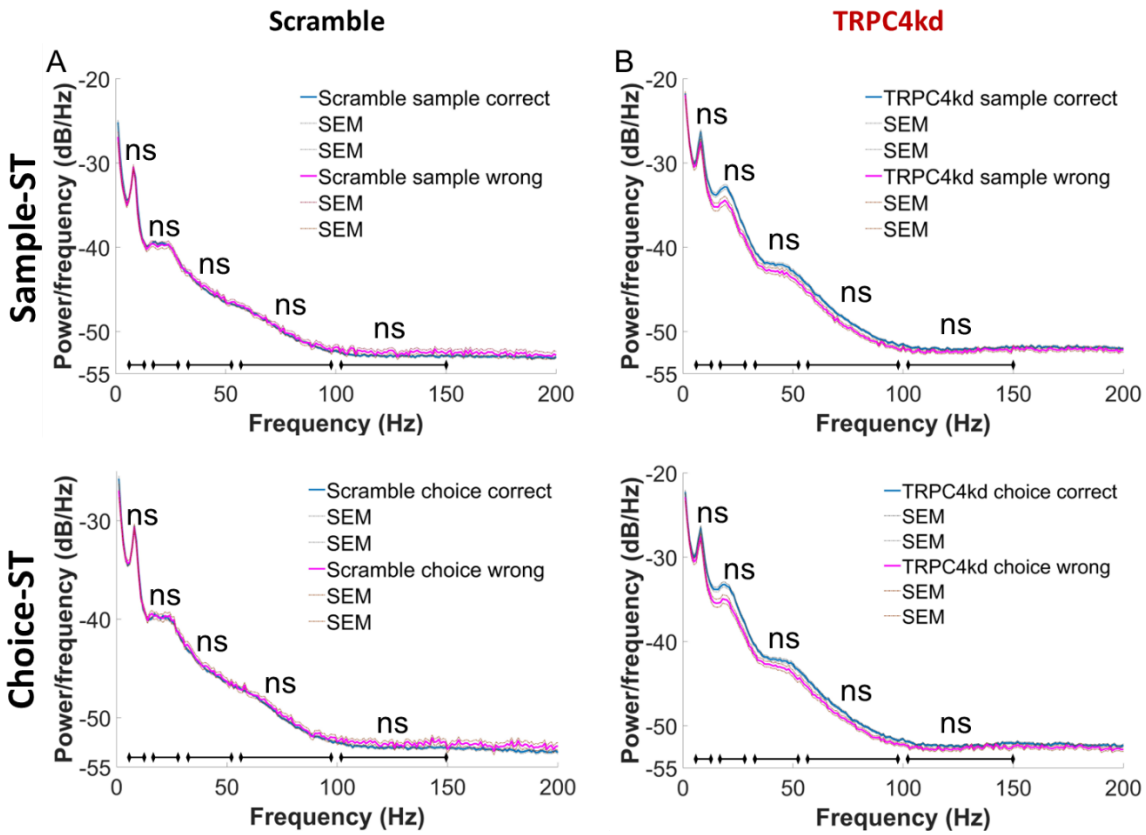

Figure 3.3.6: Power spectrum (0–200 Hz) of LFP recorded from CA1 of mice in T-maze ST (start) segment comparing sample correct versus sample incorrect and choice correct versus choice incorrect phases. The black divider lines on the X-axis show divided frequency bands. **A-top & bottom:** power spectrum comparison between the sample correct versus sample incorrect for scramble (top) and power spectrum comparison between the choice correct versus choice incorrect for scramble (bottom). **B- top & bottom:** power spectrum comparison between the sample correct versus sample incorrect for scramble (top) and power spectrum comparison between the choice correct versus choice incorrect for scramble (bottom). n = 500 for correct scramble trials, n = 90 for incorrect scramble trials, n = 478 for correct TRPC4KD trials, and n = 218 for incorrect TRPC4KD trials in each defined frequency range.

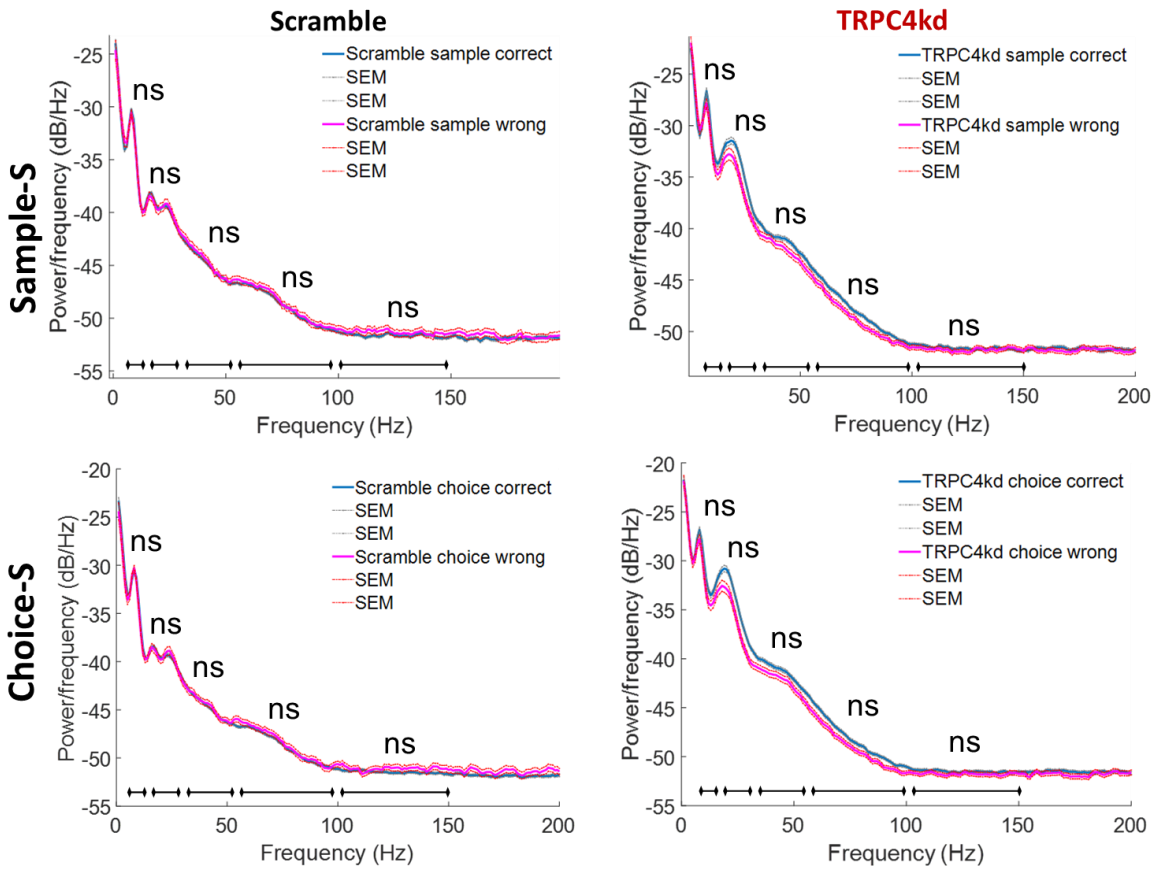

Figure 3.3.7: Power spectrum (0–200 Hz) of LFP recorded from CA1 of mice in T-maze S (stem) segment comparing the sample correct versus sample incorrect and choice correct versus choice incorrect phases. The black divider lines on the X-axis show divided frequency bands. **A-top & bottom:** power spectrum comparison between the sample correct versus sample incorrect for scramble (top) and power spectrum comparison between the choice correct versus choice incorrect for scramble (bottom). **B- top & bottom:** power spectrum comparison between the sample correct versus sample incorrect for scramble (top) and power spectrum comparison between the choice correct versus choice incorrect for scramble (bottom). n = 500 for correct scramble trials, n = 90 for incorrect scramble trials, n = 478 for correct TRPC4KD trials, and n = 218 for incorrect TRPC4KD trials in each defined frequency range.

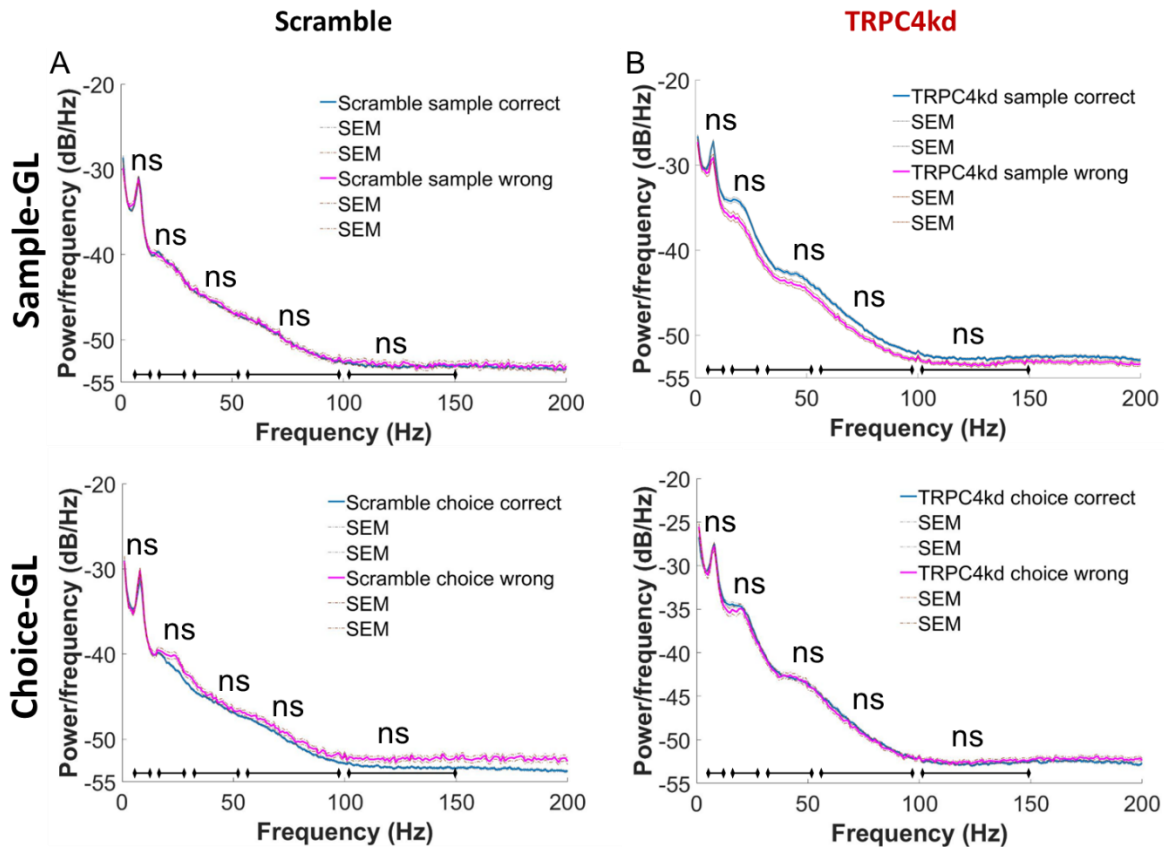

Figure 3.3.8: Power spectrum (0–200 Hz) of LFP recorded from CA1 of mice in T-maze GL (goal) segment comparing the sample correct versus sample incorrect and choice correct versus choice incorrect phases. The black divider lines on the X-axis show divided frequency bands. **A-top & bottom:** power spectrum comparison between the sample correct versus sample incorrect for scramble (top) and power spectrum comparison between the choice correct versus choice incorrect for scramble (bottom). **B- top & bottom:** power spectrum comparison between the sample correct versus sample incorrect for scramble (top) and power spectrum comparison between the choice correct versus choice incorrect for scramble (bottom). n = 500 for correct scramble trials, n = 90 for incorrect scramble trials, n = 478 for correct TRPC4KD trials, and n = 218 for incorrect TRPC4KD trials in each defined frequency range.

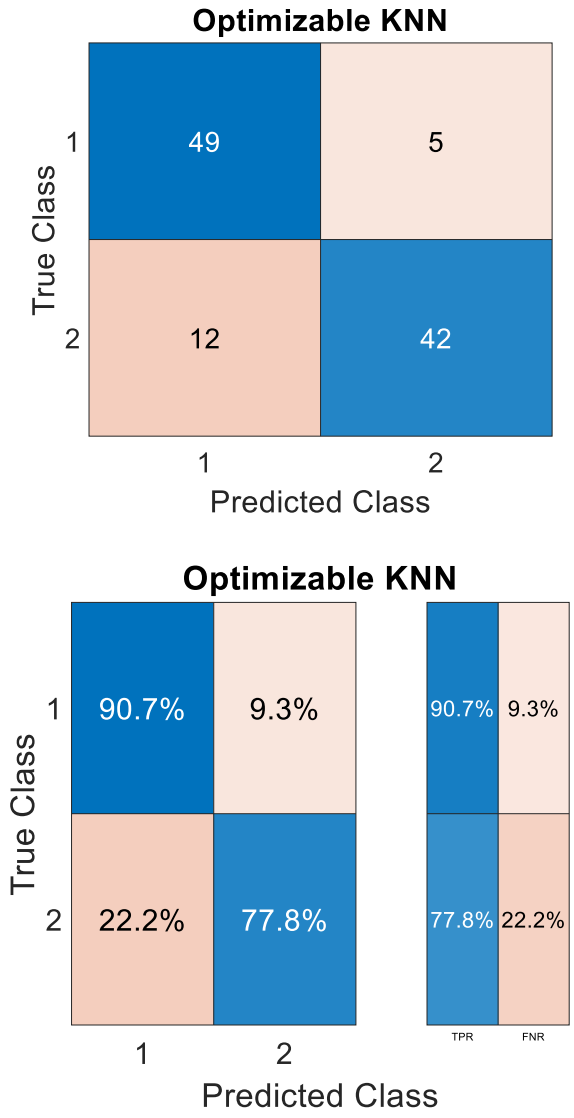

Figure 3.3.9: Confusion matrix for the experimental group prediction (scramble or TRPC4KD) based on beta oscillations. Data were classified using a weighted KNN. **Top:** The columns show the predicted classes and rows show the true classes. Variable one represents the scramble, and number two represents TRPC4KD. Blue color shows true groups versus orange depicting incorrect predicted groups. **Bottom:** Percentage calculation for true and predicted observations calculated using the top figure. **Bottom-Right:** True positive rates (TPR) and false negative rate (FNR) values for each group.

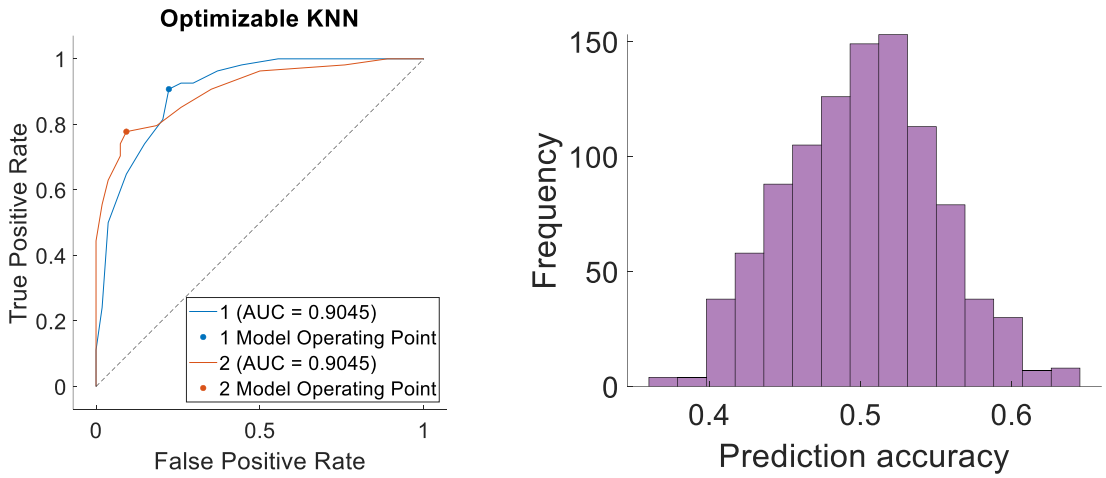

Figure 3.3.10: Left: The receiver operating characteristic (ROC) curves for the model's two operating points, highlighting the area under the curve (AUC) as a measure of the model's discrimination ability. The blue line shows the true positive rate (TPR) versus the orange line depicting the false positive rate (FPR). **Right:** Prediction accuracy of 1000 randomized prediction feature obtained from a trained network (Optimizable KNN) compared to obtained original accuracy 84.3% (sample T-test, ($p<0.001$).

3.3.2 Theta-gamma coupling (Modulation Index)

In Section 1.4.3, the role of theta and gamma oscillations in information processing was highlighted. As mentioned before, theta-gamma coupling has been proposed as one of the working memory mechanisms. To measure this coupling, the MI was calculated using a Matlab script developed previously based on the description in Chapter 2.5.2. The MI could identify phase–amplitude coupling between two different frequency ranges: “phase modulating” (f_P) and “amplitude- modulated” (f_A) frequency bands. Theta-gamma coupling change could also be visually controlled by plotting filtered LFP data (Figures 3.3.2.1 and 3.3.2.2).

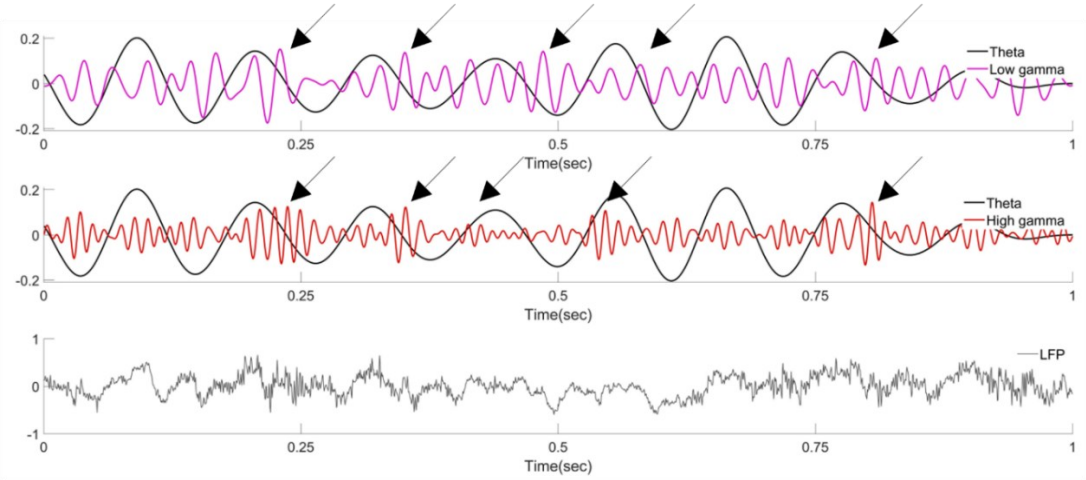

Figure 3.3.2.1: An example from the scramble filtered LFP showing the comparison of low gamma and high gamma amplitudes relative to theta phases. The arrows indicate the peak amplitudes of gamma oscillations within each theta cycle.

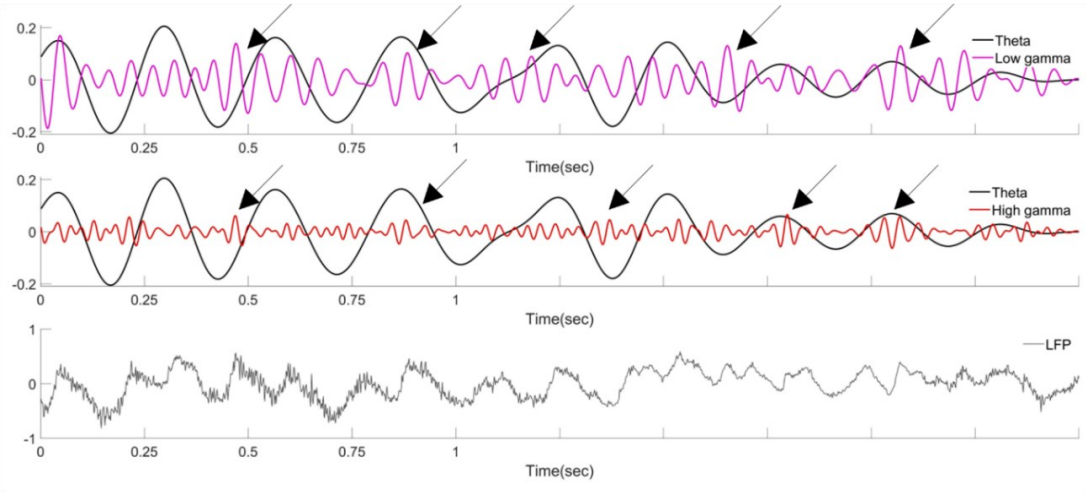

Figure 3.3.2.2: An example from the TRPC4KD filtered LFP demonstrating the comparison of low gamma and high gamma amplitudes relative to theta phases. The arrows indicate the peak amplitudes of gamma oscillations within each theta cycle. Low gamma and high gamma phases markedly differed from those of scramble.

MI was computed across all datasets and averaged for each group. Significantly higher MI values were observed between theta phase and high gamma frequency (65–100 Hz) in the scramble group compared to TRPC4KD. Furthermore, MI values were lower in the low gamma oscillations band (30–55 Hz) for TRPC4KD compared to Scramble (Figure 3.3.2.3). These results suggest a pronounced impairment in theta-gamma coupling within the TRPC4KD group, potentially elucidating the decline in working memory performance seen in this group when compared to the scramble.

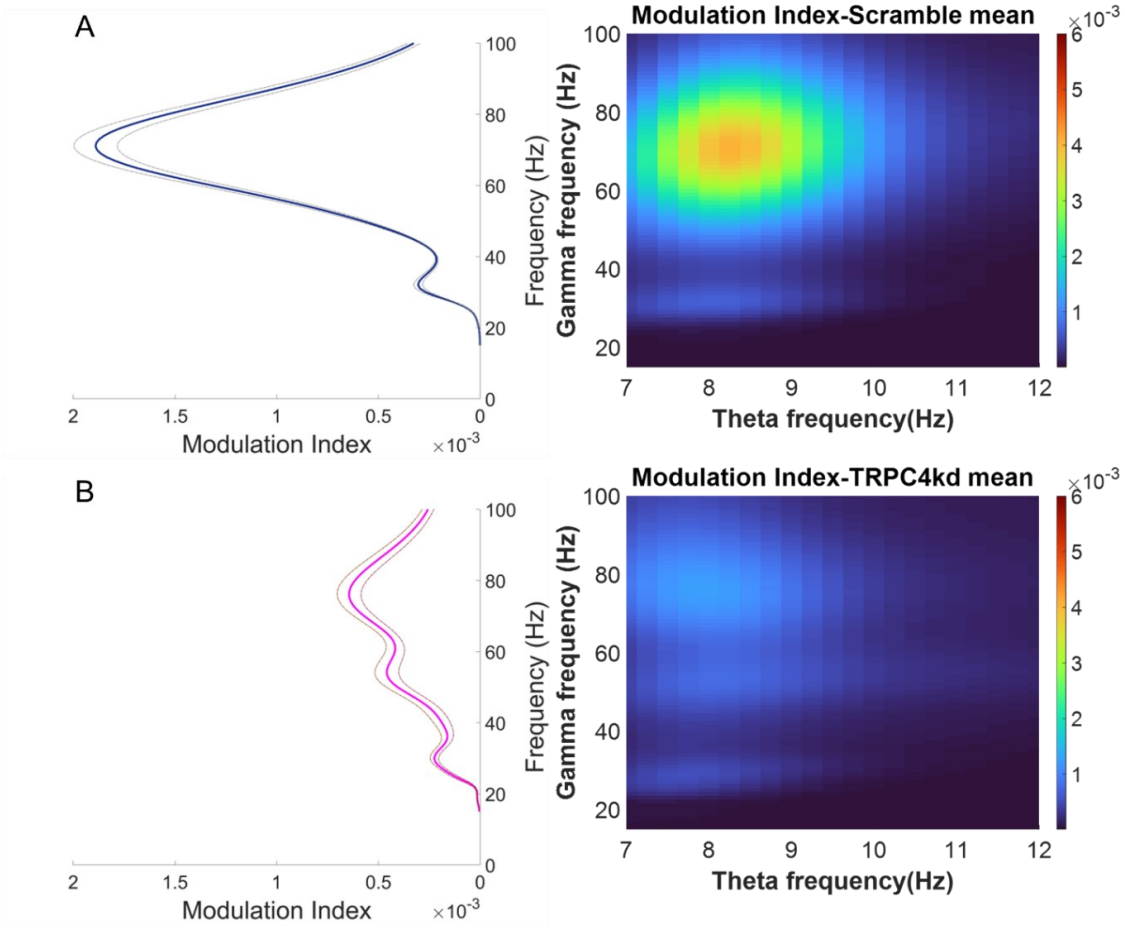

Figure 3.3.2.3: Averages compared between the scramble and TRPC4KD. A: The Scramble group exhibited a high MI within the high gamma frequency range. B: The TRPC4KD group displayed lower MI than the scramble (Mann-Whitney U Exact (2-tailed), $p < 0.001$, $n = 60$ for scramble and $n = 70$ for TRPC4KD).

The subsequent step involved plotting the theta-gamma power-phase analysis to determine the theta phases where gamma oscillations exhibited higher power. The theta-gamma power phase was averaged for each group, revealing that the scramble group displayed elevated power in both low gamma and high gamma frequencies during specific theta phases. In contrast, TRPC4KD showed no distinct theta phase-locked gamma power during the spatial working memory task (Figure 3.3.2.4). This power phase analysis further supports our MI findings, indicating a relationship between gamma power and specific theta phases regarding TRPC4KD. Additionally, the most potent gamma oscillation power occurred at different theta oscillation phases compared to the scramble.

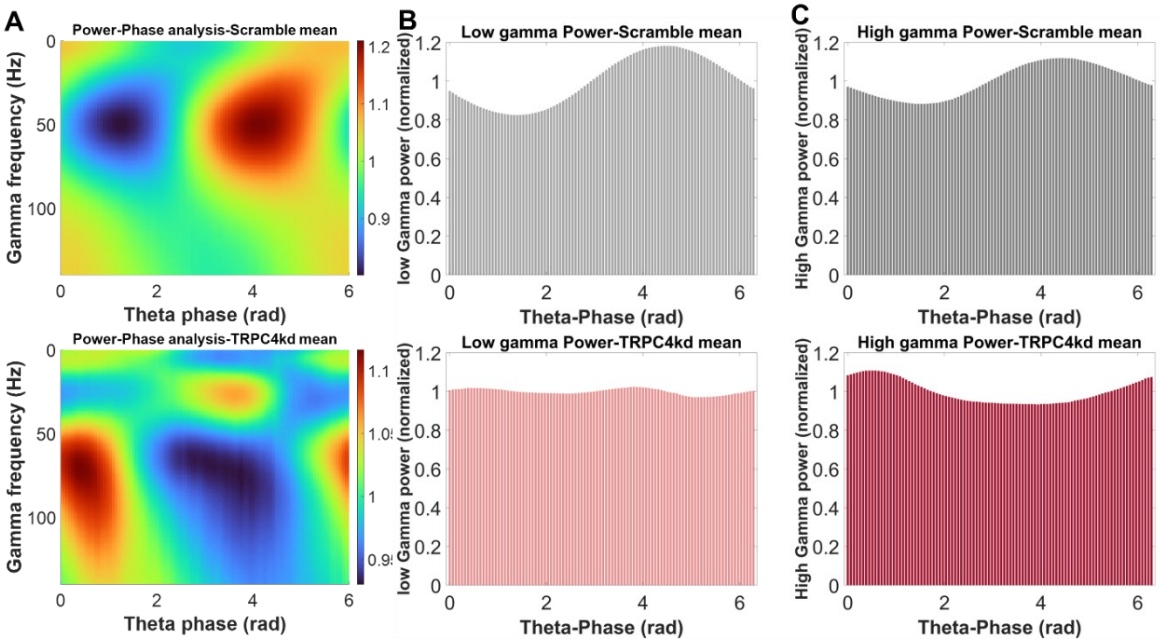

Figure 3.3.2.4: Average theta-gamma power-phase analysis results for the groups. **A-top:** Average power-phase analysis for the scramble group. **A-bottom:** Average power-phase analysis for TRPC4KD. **B:** Histogram showing the count of low gamma oscillation power during theta phase for the scramble (top) and TRPC4KD (bottom) groups. **C:** Histogram displaying the count of high gamma oscillation power during theta phase for the scramble (top) and TRPC4KD (bottom) groups, respectively.

The MI was computed in the Start (ST) and Goal (GL) regions to evaluate potential discrepancies between the sample, and choice phases in correct and incorrect

trials individually, employing the Kruskal–Wallis test, followed by post hoc Dunn's test with Bonferroni adjustment (Figure 3.3.2.5–8). The objective of this analysis was to emphasize the pivotal phase of theta-gamma coupling during working memory tasks. No significant variances were detected in the high gamma, and HFO frequency bands for the scramble in the start and goal areas (Figure 3.3.2.5–6). Only low gamma oscillations demonstrated a significant difference between the sample and choice phases in start and goal area for correct trials (Figure 3.3.2.5–6, $p=0.002$ for start area and $p<0.001$ for goal area). These findings suggest a lack of substantial associations between MI in high gamma frequency across segments, and task performance within the examined task phases. Low gamma MI change in correct trials may indicate a CA3 input role in task performance.

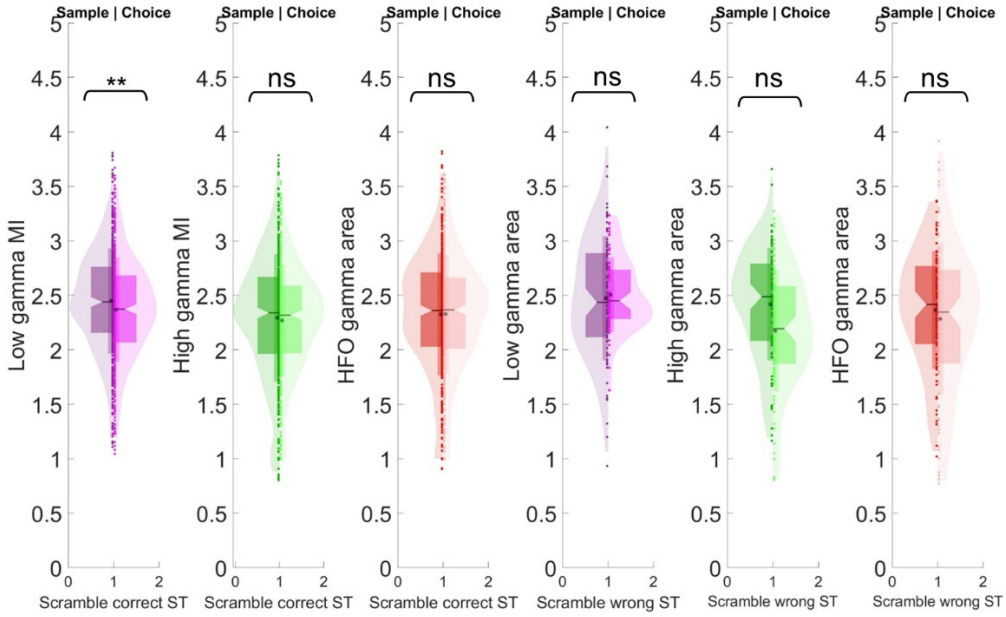

Figure 3.3.2.5: MI average in three frequency ranges in correct (first three column) and incorrect (second three column) of the sample and choice phases (left side of each figure vs right side of each figure) in the scramble group. MI in start (ST) correct trials showed no significant difference. There was a significant difference in the start (ST) incorrect trial MI in high gamma oscillations (e). n = 510 for correct and n = 90 for incorrect scramble ST. ns: not significant. *: mean. horizontal line: median

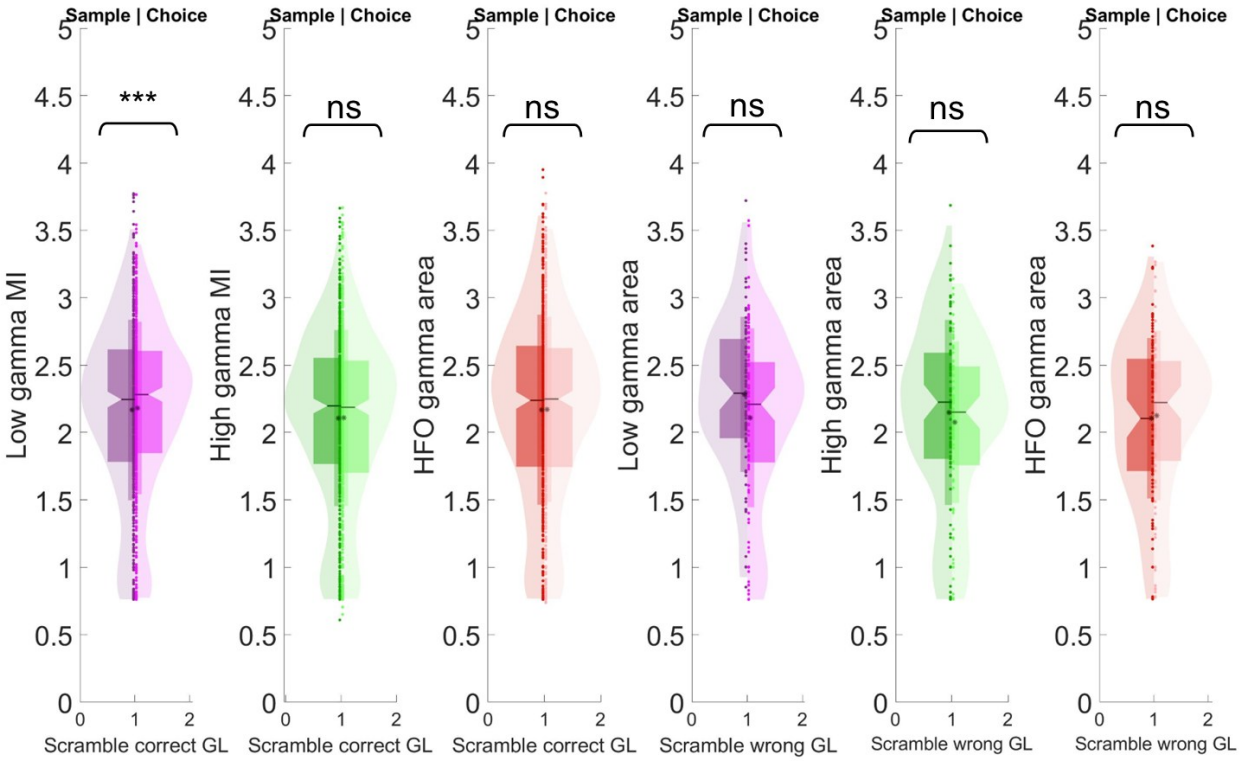

Figure 3.3.2.6: MI average of three oscillations bands in correct (first three column) and incorrect (second three column) of the sample and choice phases (left side of each figure vs right side of each figure) in the scramble group. MI in goal (GL) correct and incorrect trials showed no significant difference. n = 510 for correct and n = 90 for incorrect scramble GL. ns: not significant. *: mean horizontal line: median

Despite the overall decrease in MI in TRPC4KD, no significant alterations were observed in the ST and GL for both correct and incorrect trials (Figure 3.3.2.7–8). Like the scramble condition, no significant changes were noted in the low gamma, high gamma, and HFO frequency bands for TRPC4KD in the start and goal regions. The outcomes in the start and goal areas reveal a decline in theta-gamma coupling within the T-maze segments, particularly in the high gamma oscillation bands, mirroring trends seen in the comodulogram plots (Figure 3.3.2.3). These results indicate a general decrease in MI without significant associations with specific segments or trial phases.

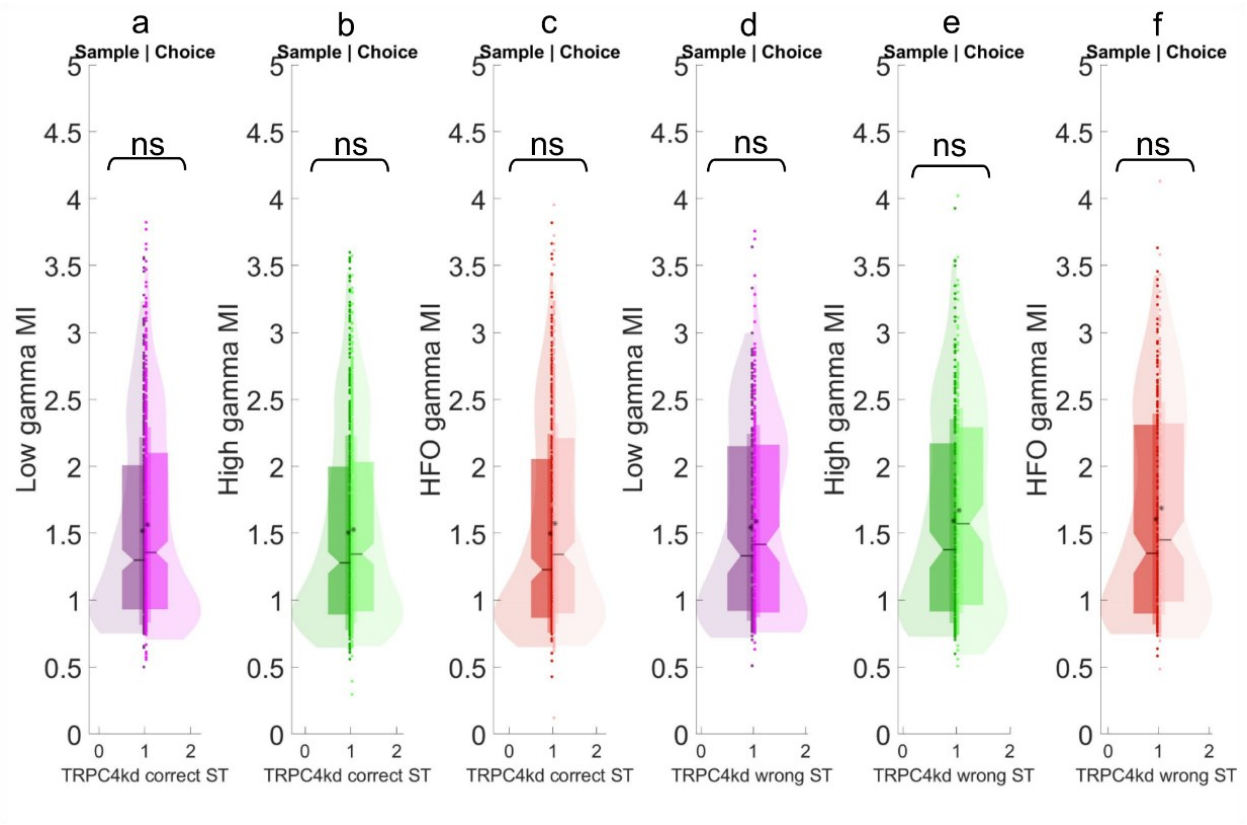

Figure 3.3.2.7: MI average of three oscillation bands in correct and incorrect sample and choice phases (left side of each figure vs right side of each figure) in the TRPC4KD group. No difference existed in ST correct/incorrect trials MI. n = 478 for correct and n = 218 for incorrect TRPC4KD ST. *: mean horizontal line: median

Furthermore, MI data were analyzed based on the animal trajectory (sample ST to the sample GL, sample GL to choice ST, and choice ST to choice GL) and trial performance (correct or incorrect). The aim was to determine whether MI changes occurred in different segments and the possible correlation with working memory involvement. No difference was observed between MIs in T-maze segments during the sample and choice phases in both groups (Figure 3.3.2.9). Interestingly, pairwise comparisons of high gamma MI between the scramble and TRPC4kd groups unveiled significant disparities in both trial phases within the ST and GL segments (Figure 3.3.2.10). These

findings could elucidate the link between theta-gamma coupling and the relative working memory performance observed in these distinct groups.

A correlation analysis was conducted to assess the relationship between performance and the MI in both the scramble and TRPC4KD groups (Figure 3.3.2.11). The results indicate a correlation between animal performance and MI in both groups (R square change = 0.150, adjusted R2 = 0.144, $p < 0.150$). The goal was to assess whether a link exists between theta-gamma coupling and working memory performance. The analysis showed a correlation between task performance and MI for both groups and overall performance and MI as well. This indicates that theta-gamma coupling plays an essential role in working memory function and consequently affects performance.

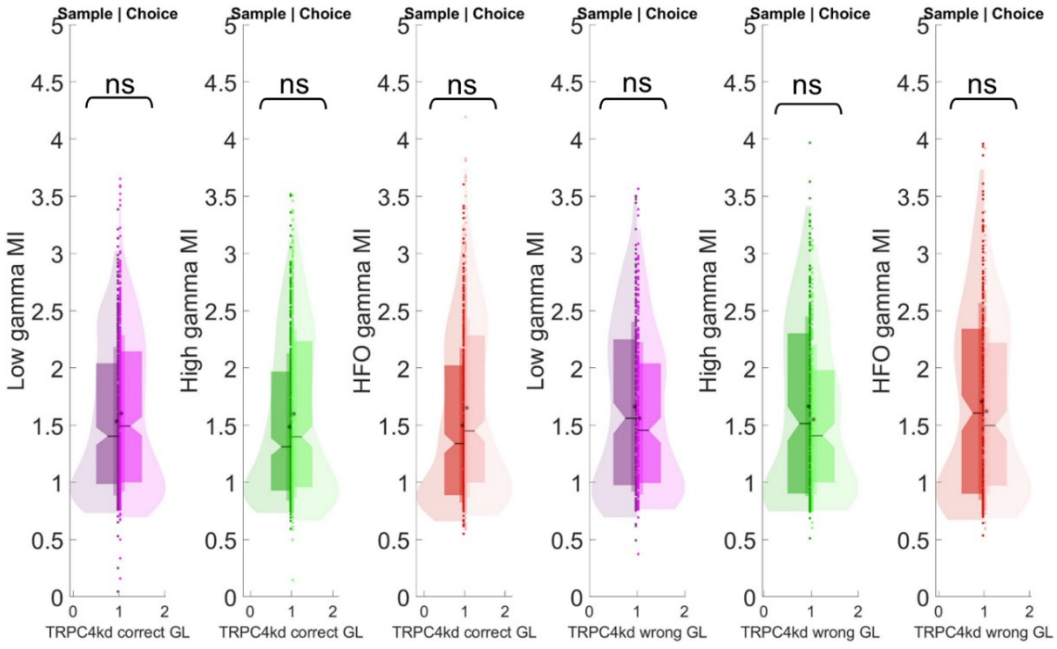

Figure 3.3.2.8: MI average in correct/incorrect sample and choice phases (left side of each figure vs right side of each figure) in the TRPC4KD group. MI HFO oscillations in goal (GL) correct phases showed a significant difference (linear regression, p=0.003). n = 478 for correct and n = 218 for incorrect TRPC4KD GL. *: mean horizontal line: median

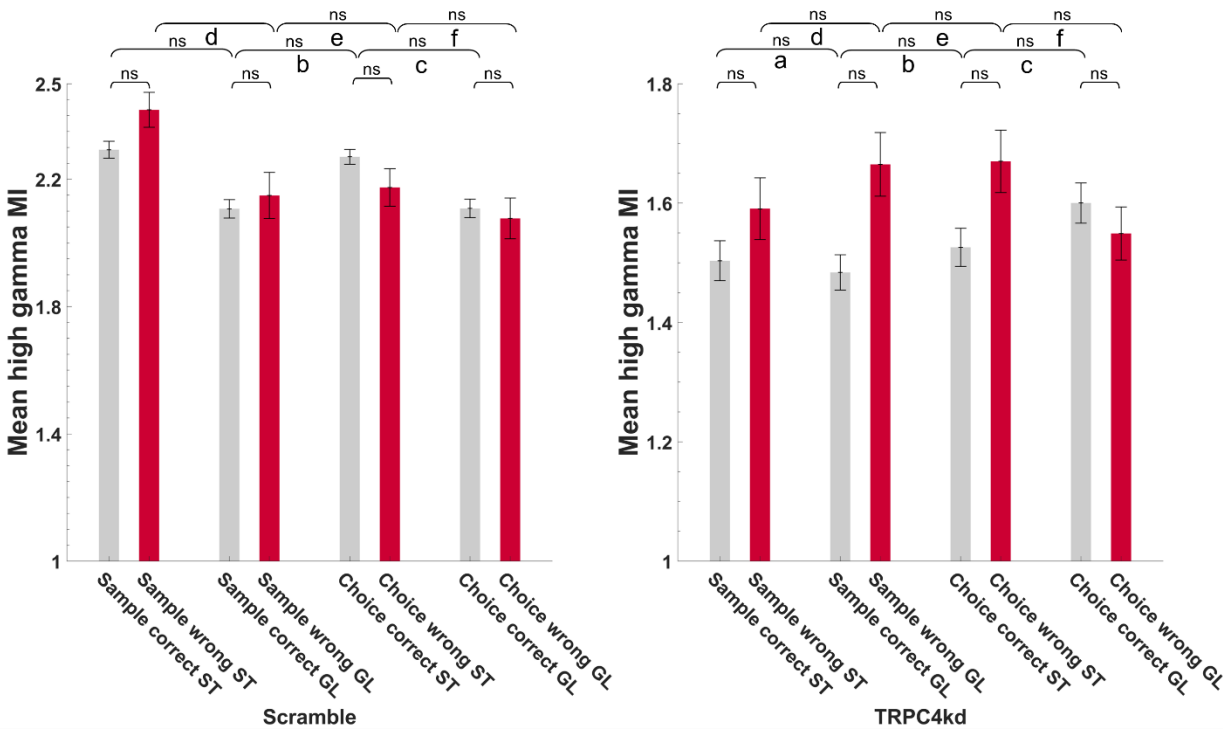

Figure 3.3.2.9: The average MI within the high gamma oscillation range is compared in the segments temporally visited in the scramble (left) and TRPC4KD (right). MI values in correct trials were contrasted with those in incorrect trials and other temporally relevant segments within the Start (ST) and Goal (GL) regions. n = 510 for correct and n = 90 for incorrect scramble sample/choice ST/GL. n = 478 for correct and n = 218 for incorrect TRPC4KD sample/choice ST/GL. ns: no significance observed in the comparisons made.

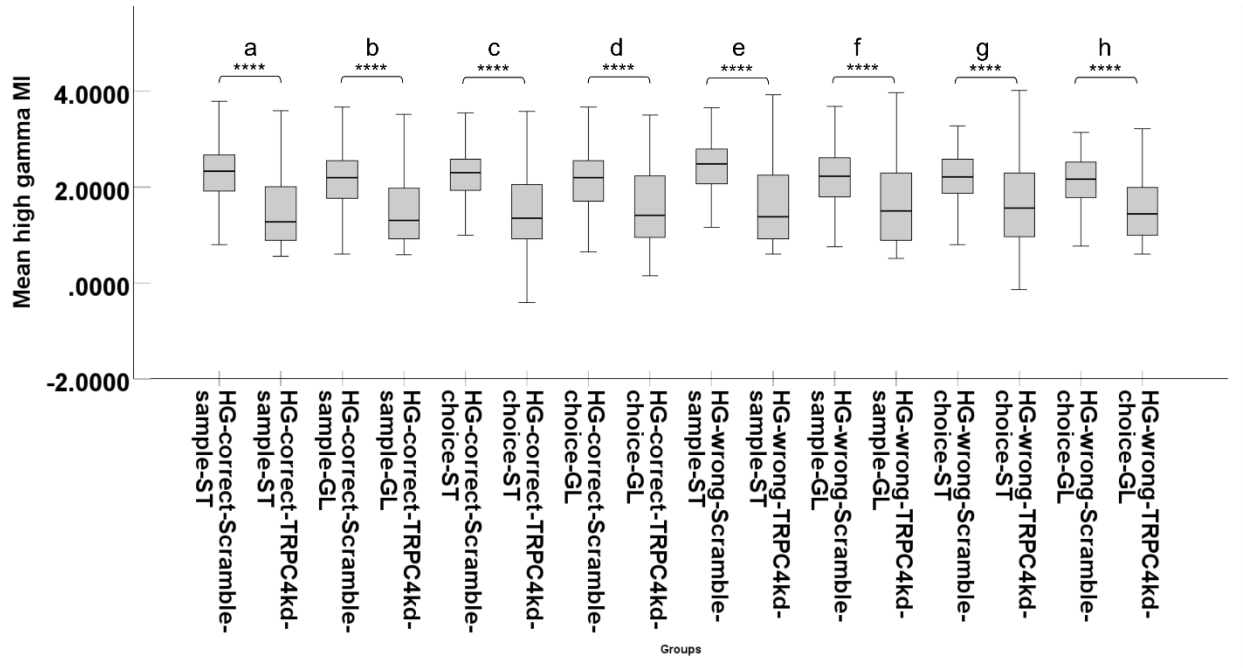

Figure 3.3.2.10: The average MI in the high gamma oscillation range for pairwise comparison between scramble and TRPC4KD groups along the animal trajectory in the T-maze. A pairwise post-hoc Dunn test revealed significant differences between each pair of identical scramble and TRPC4KD groups within the ST and GL areas during both sample and choice phases, as well as correct and incorrect performances (Kruskal–Wallis test followed by post-hoc Dunn's test, with significance levels denoted as a: $p < 0.0001$, b: $p < 0.0001$, c: $p < 0.0001$, e: $p < 0.0001$, f: $p < 0.0001$, g: $p < 0.0001$, and h: $p < 0.0001$, respectively; n = 510 correct and n = 90 incorrect scramble. n = 478 for correct and n = 218 for incorrect TRPC4KD).

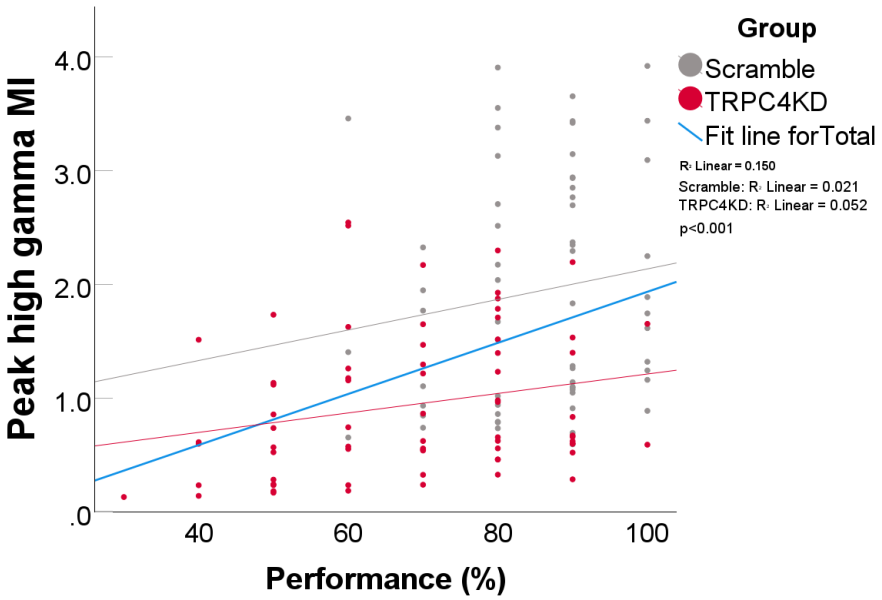

Figure 3.3.2.11: A correlation analysis showing the relationship between performance and MI in both the scramble and TRPC4KD groups (R square change=0.150, p<0.001, n=130). The gray and red lines represent the correlation for the scramble and TRPC4KD groups (R^2=0.021, p=0.271, n=60 for scramble, R^2=0.052, p<0.001, n=70 for TRPC4KD) respectively, while the blue line illustrates the overall correlation for both groups.

3.3.3 MI and its relationship with speed

In the discussion of MI findings, the relationship between the performance of the animals and their running speed was investigated by employing partial correlation to discern the impact of speed on the high gamma amplitude and its subsequent effect on the MI measurements. The partial correlation analysis indicated a positive correlation between performance and running speed while controlling for theta and high gamma amplitude, specifically for the scramble condition on the entire T-maze (Table 3.3.3.1 top; r(26) = 0.156, p = 0.429). When the same analysis was conducted for the TRPC4KD group, a significant positive correlation between performance and speed was observed, controlling for high gamma and theta amplitude (Table 3.3.3.1 bottom; r(31) = 0.434, p = 0.012). This suggests that the experimental group showed a stronger

correlation between running speed and performance than the control group. Additionally, this correlation implies that, despite the higher speed in the experimental group, the theta-gamma coupling analysis was not influenced by theta and gamma amplitude and, thus, not by speed.

Correlations-scramble

Control Variables			e	Mean_Speed
Mean_Theta1 & Mean_HG1	Performance	Correlation	1,000	0,156
		Significance (2-tailed)		0,429
		df	0	26
	Mean_Speed	Correlation	0,156	1,000
		Significance (2-tailed)	0,429	
		df	26	0

Correlations-TRPC4KD

Control Variables			Performance	Mean_Speed
Mean_Theta2 & Mean_HG2	Performance	Correlation	1,000	0,434
		Significance (2-tailed)		0,012
		df	0	31
	Mean_Speed	Correlation	0,434	1,000
		Significance (2-tailed)	0,012	
		df	31	0

Table 3.3.3.1: The results of partial correlation analyses examining the relationships between performance with running speed, theta and high gamma amplitudes. The partial correlation coefficients (r) and their associated p-values are presented for each pair of variables, including running speed, theta amplitude, and high gamma amplitude. **Top:** Partial correlation for the scramble group (n = 30). **Bottom:** Partial correlation for TRPC4KD (n = 35). The analysis controls for potential confounding factors to isolate the unique contribution of each variable to performance.

Notably, MI is inherently insensitive to the absolute amplitude of gamma oscillations when evaluating phase–amplitude coupling (118). This characteristic is particularly advantageous, as it ensures that the MI quantifies the strength of coupling independent of the overall signal magnitude. This property of MI is crucial for the current analysis, as it allows me to focus on the coupling dynamics without the potential biases that could be introduced by variations in signal amplitude.

3.4 Single Unit Analysis

3.4.1 Spatial information

Following the clustering process, single-unit data were manually inspected and curated using Klusters software (Lynn Hazan). Putative pyramidal cells were initially filtered based on their firing frequency, with only cells exhibiting a firing rate of above 1 Hz (Figure 3.4.1.2-3) or 0.1 Hz (Figure 3.4.1.4-5) and less than 5 Hz included in the analysis. Subsequently, the cells were segregated according to their respective experimental groups. After the outliers were removed, spatial information was computed and subsequently smoothed to investigate potential differences in place cell activity between the groups. Spatial information quantifies the extent to which pyramidal cells exhibit location-specific firing. Moreover, firing rates of the cells were calculated for both groups (Figures 3.4.1.1 & 3.4.1.2 & 3.4.1.4). A significant difference in spatial information was observed between the two groups, whereas no significant difference was detected in firing rates (Figure 3.4.1.3, Mann–Whitney U test, $p < 0.001$). However, when the cells were filtered in the range of 0.1-5 Hz, a significant difference in firing rates was detected as well (Figures 3.4.1.5, Mann–Whitney U test, $p < 0.001$). These findings highlight the impact of TRPC4 knockdown on the spatial information of pyramidal cells in the TRPC4KD group, as well as on firing rates when using different cell filtering criteria.

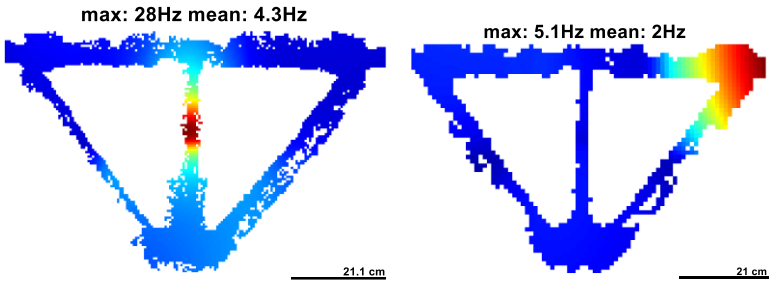

Figure 3.4.1.1: An example of a rate map and spatial information. Warmer colors show a higher rate of activity in the location **Left:** Rate map of place cell in scramble. **Right:** Rate map of a place cell in TRPC4KD.

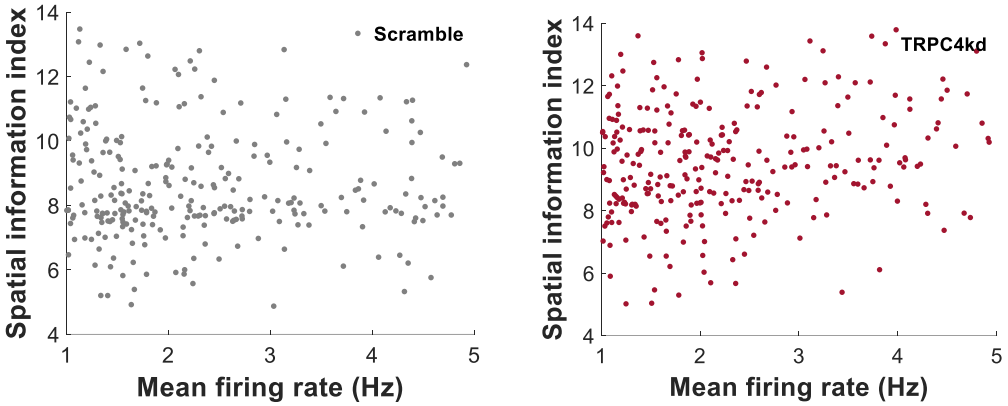

Figure 3.4.1.2: Scatter plots illustrating the relationship between spatial information and mean firing rate (Hz) for cells in control and experimental group (cells filtered above 1 Hz). Both plots indicate an inverse correlation, where cells with higher spatial information tend to have lower firing frequencies within the typical range of pyramidal cell activity. **Left panel:** Scramble group. **Right panel:** TRPC4KD group.

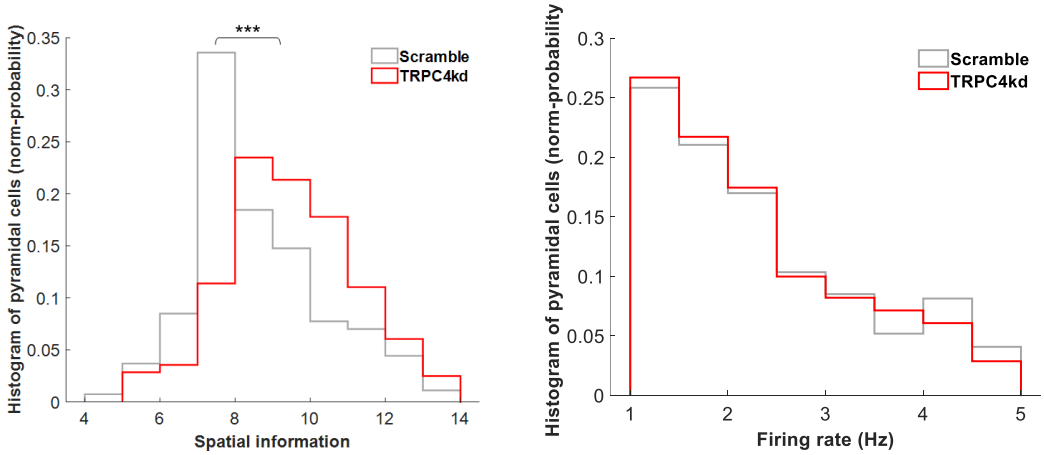

Figure 3.4.1.3: Histograms comparing the spatial information (left panel) and firing rates (right panel) of pyramidal cells between the scramble and TRPC4KD. **Left:** A significant difference in spatial information was observed between the scramble and TRPC4KD groups (Mann–Whitney U test, $p < 0.001$, n=271 for scramble, n=281 for TRPC4KD). **Right:** No significant difference in firing rates was detected between the groups (Mann–Whitney U test, $p = 0.554$, n=271 for scramble, n=281).

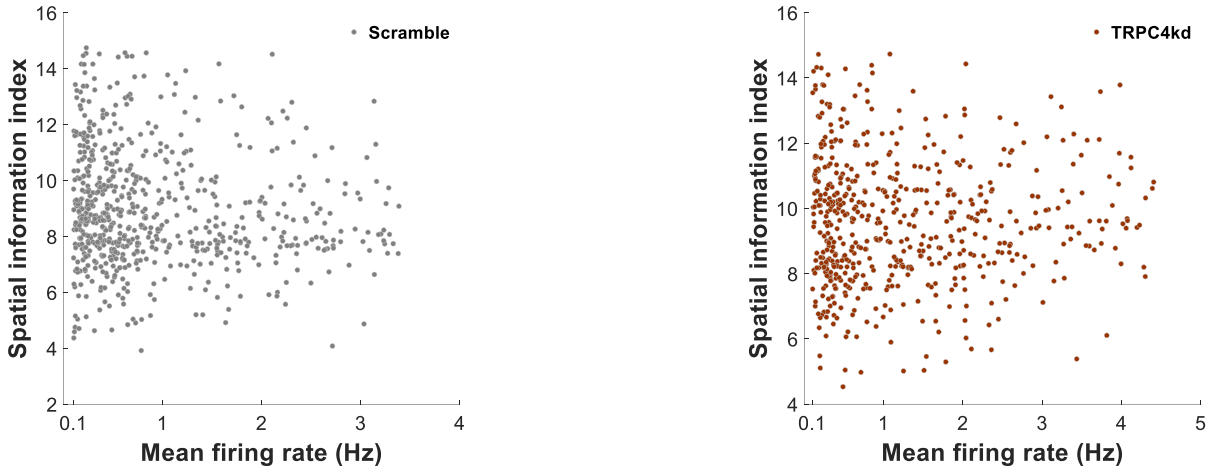

Figure 3.4.1.4: Scatter plots illustrating the relationship between spatial information and mean firing rate (Hz) for cells in control and experimental group (cells filtered above 0.1 Hz). Both plots indicate an inverse correlation, where cells with higher spatial information tend to have lower firing frequencies within the typical range of pyramidal cell activity. **Left panel:** Scramble group. **Right panel:** TRPC4KD group.

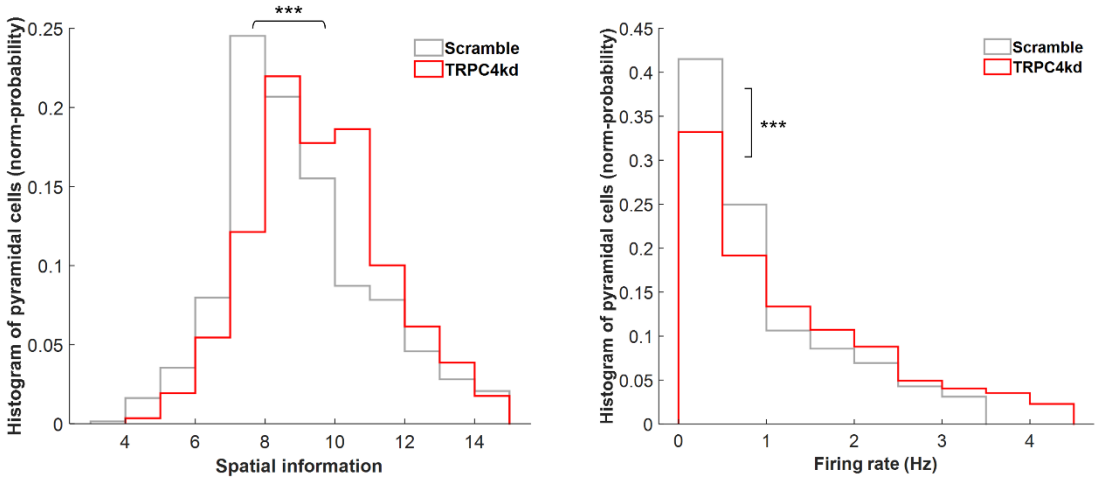

Figure 3.4.1.5: Histograms comparing the spatial information (left panel) and firing rates (right panel) of pyramidal cells between the scramble and TRPC4KD. **Left:** A significant difference in spatial information was observed between the scramble and TRPC4KD groups (Mann–Whitney U test, $p < 0.001$, n=677 for scramble, n=569 for TRPC4KD). **Right:** Significant difference in firing rates was detected between the groups (Mann–Whitney U test, $p < 0.001$, n=677 for scramble, n=569 for TRPC4KD).

3.4.2 Phase precession

Phase precession was defined as the correlation between theta phase of spikes and the position or time inside the firing field. Phase precession encodes behavior-dependent variables beyond just position, such as goal location. The theta phase of spike changes and shifts from early phases to the trough of theta when the animal enters the place field. The correlation between spike and theta phase (rho) and the slope of the correlation will show whether a cell has phase precession or not. To measure phase precession, the rho (circular-linear regression coefficient between theta phase and spike) was calculated (Figure 3.4.2.1). The theta phases were filtered according to three main locations in the T-maze, including the start, main stem, and goal (phase precession in a specific location). Only spike phase histograms of entire T-maze were plotted to give an overall view of the mean phase in scramble compared to TRPC4KD (Figure 3.4.2.2). Spikes theta phases differed between groups. The mean direction was 204.3° in scramble and 294.7° in TRPC4KD. Phase precession cells were chosen based on linear-circular correlation p value significance. The phase precession cell phase (291.8°) in TRPC4KD was different from scramble (230.1°) (Figure 3.4.2.3). Different firing phases may indicate impairment in phase precession and subsequently may affect other procedures involved, such as LTP/LTD and STDP.

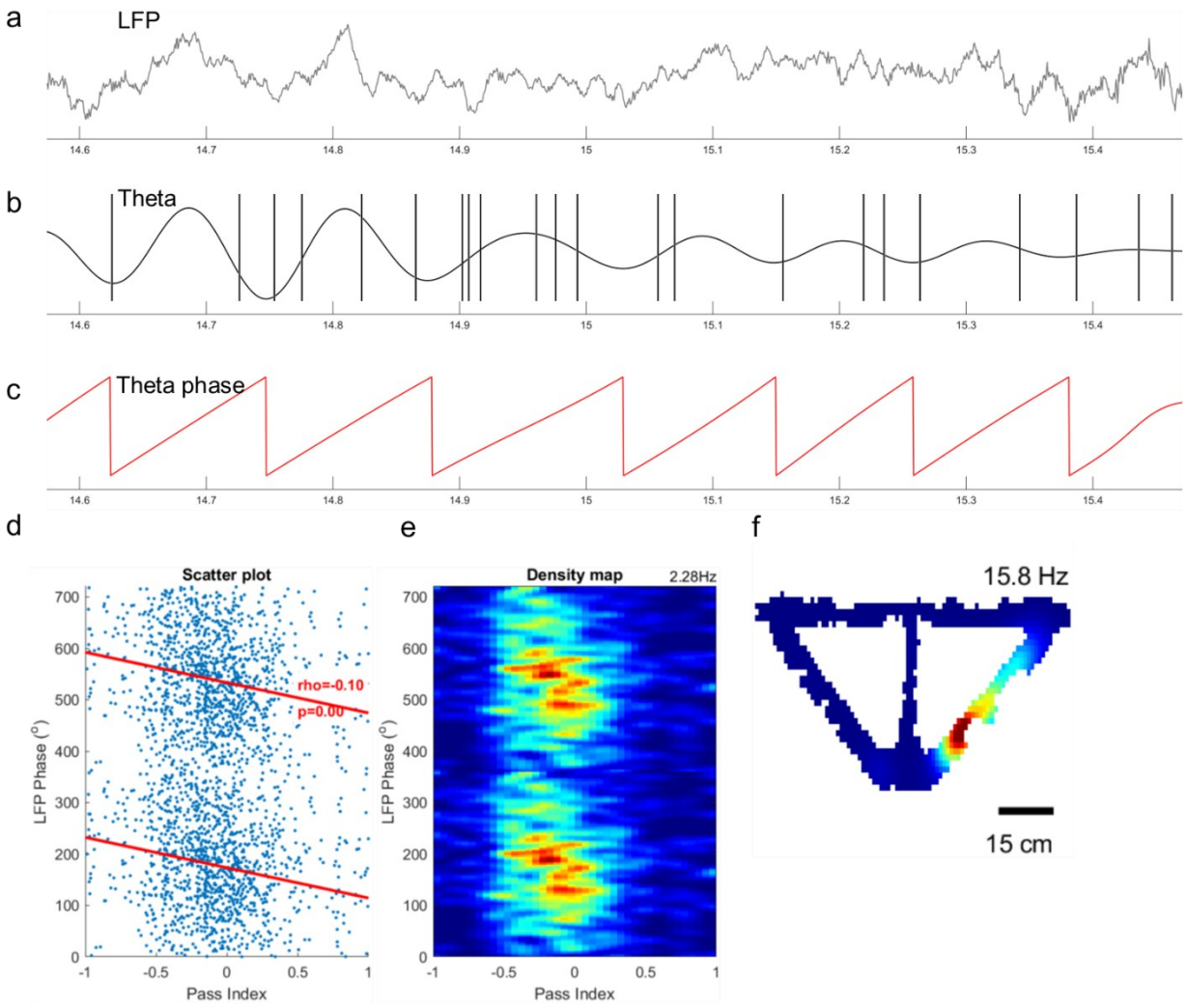

Figure 3.4.2.1: An example of phase precession calculation. A: LFP data B: Bandpass filtered theta oscillation and overlapped vertical lines represent spike time in theta oscillation. C: Calculated theta phase. D: Scatter plot of the pass index and theta phase in phase precession. The red line shows the correlation and slope. E: Density map theta phase versus pass index in phase precession. F: rate map of the related cell.

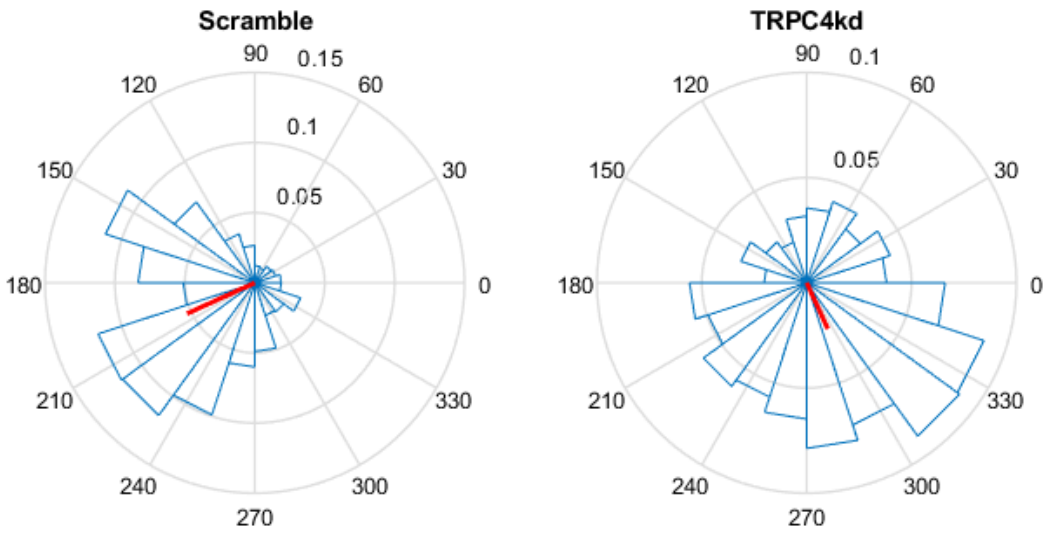

Figure 3.4.2.2: Theta phase of all spikes in both groups. The mean direction of the spike theta phase in scramble differed from that of the TRPC4KD (circular median test, p=0.0).

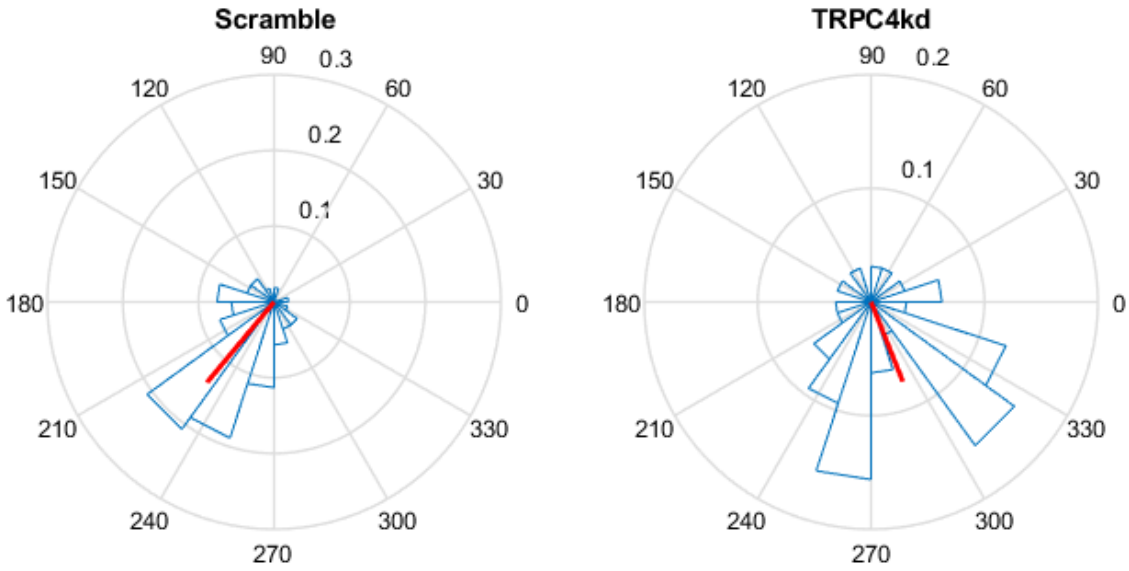

Figure 3.4.2.3: Theta phase of the spikes in the phase precession cells in both groups. The mean direction of spike theta phase in scramble differed from that of the TRPC4KD (Watson-Williams test, p=0.0001).

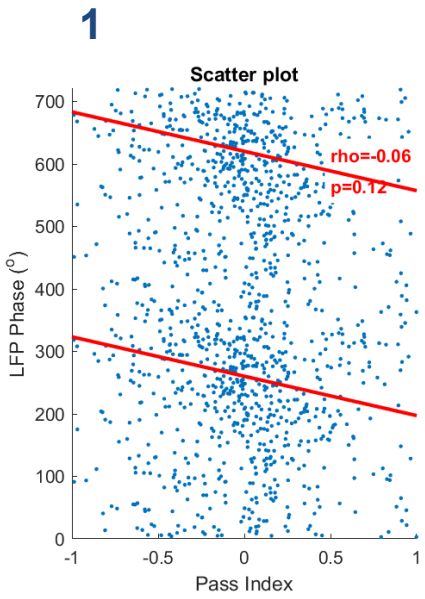

36122317

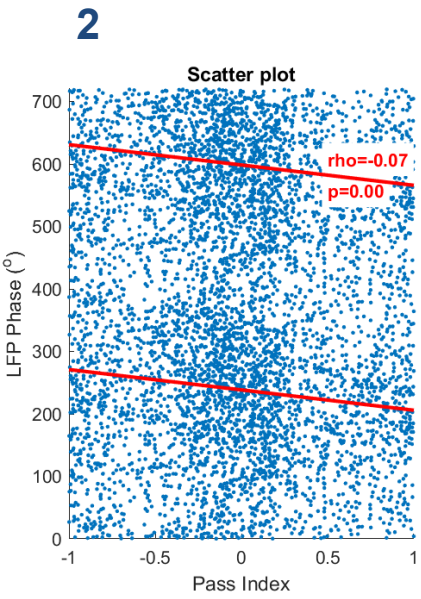

36132321

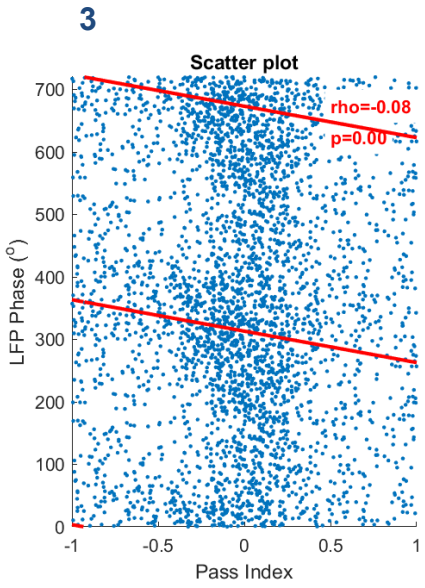

36132322

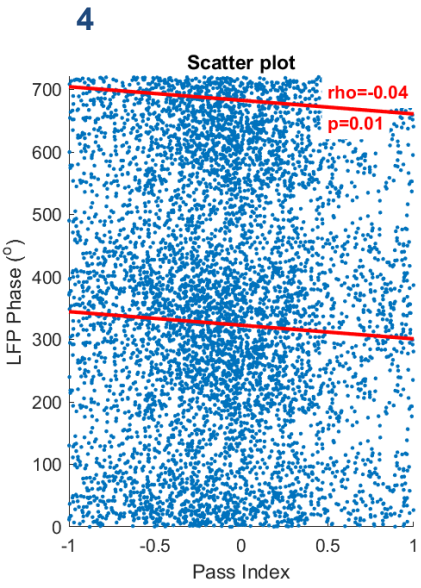

36192413

Figure 3.4.2.4: Examples of phase precession cells illustrating the relationship between spike theta phases and pass index (animal position) in T-maze, showing a negative correlation. Each point represents the theta phase of a spike event relative to the animal's position (pass index) as it navigates the maze. The red line represents the linear-circular correlation between spike theta phases and the pass index in T-maze.

The slope, rho, and theta phase were calculated using spiking dataset and LFP for whole T-maze (Figure 3.4.2.4–5). Rho depicted a non significant difference between the two groups (Figure 3.4.2.5).

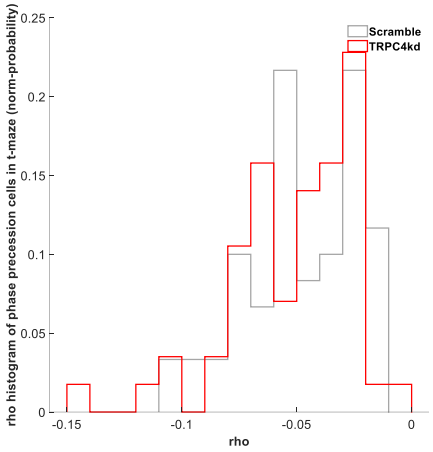

Figure 3.4.2.5: The rho histogram for phase precession cells in the T-maze. The rho histogram of phase precession cells in both groups in T-maze (Independent t-test, p=0.51139, n=60 for scramble, n=57 for TRPC4KD).

The slope of the correlation between spiking and theta phase is negative when a significant correlation exists. Spiking starts at the earliest phase of theta and shifts to the trough of theta when the firing rate is at peak (119).

Theta phase of pyramidal cells in the main stem

We then investigated whether the theta phase of neuronal spiking differed between control and KD groups across different areas of the T-maze. However, analyzing phase precession accurately is challenging when the maze is subdivided into sections, as this can truncate place fields. Therefore, I focused solely on the theta phase of spiking in the following sections. The main stem is one of the most important location in this task, since the animal needs to make a decision at the end of the stem. A histogram of spike theta phase was plotted to examine potential changes in phase for cells in both groups (Figure 3.4.2.6). The mean phase differed between the groups. However, no significant difference existed in phase precession cells. Comparing the overall phase histogram with phase precession cells illustrates that phase precession cell activity was very close

to the trough of theta in scramble and even in TRPC4KD, but the mean resultant length was smaller in TRPC4KD, depicting a more uniform phase distribution than scramble directional distribution.

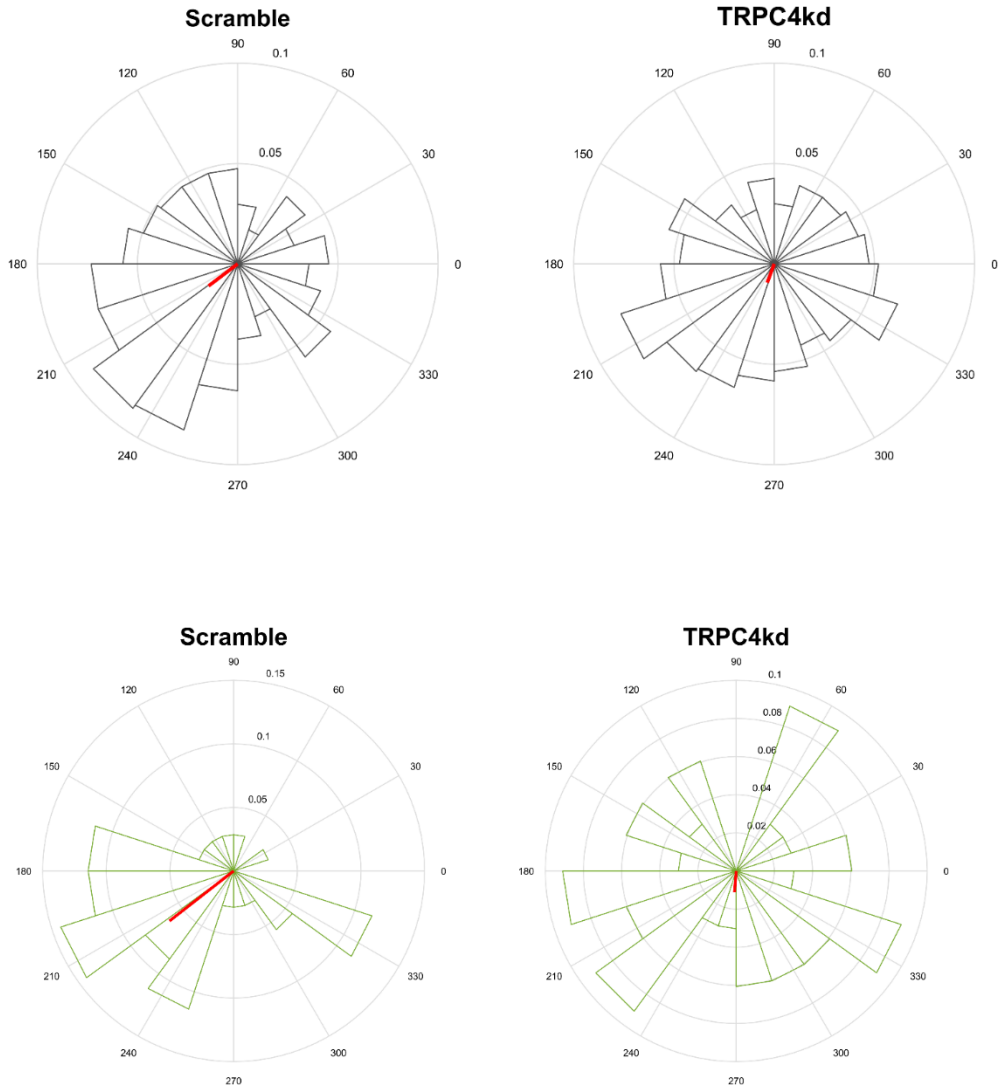

Figure 3.4.2.6: Histogram of spike phases in the main stem **Top:** Histogram of all cell's spike's phase in the main stem. There was a significant difference between the mean phase of TRPC4KD with scramble (circular mtest, h=1). **Bottom:** Histogram of phase precession cell spike's phase in the main stem. There was no significant difference between the mean phase of TRPC4KD with scramble (circular median test, p= 0.9943; mean resultant length, r=0.4476 for scramble; mean resultant length, r=0.1231 for TRPC4KD).

Start and goal area spikes in the theta phase

Phase precession was calculated for cells active in the start or goal areas to compare any differences in phase precession with the main stem between the groups. In the start area, no difference existed in the spike theta phase of phase precession cells. However, the mean phase of all cells differed between the groups (Figure 3.4.2.7).

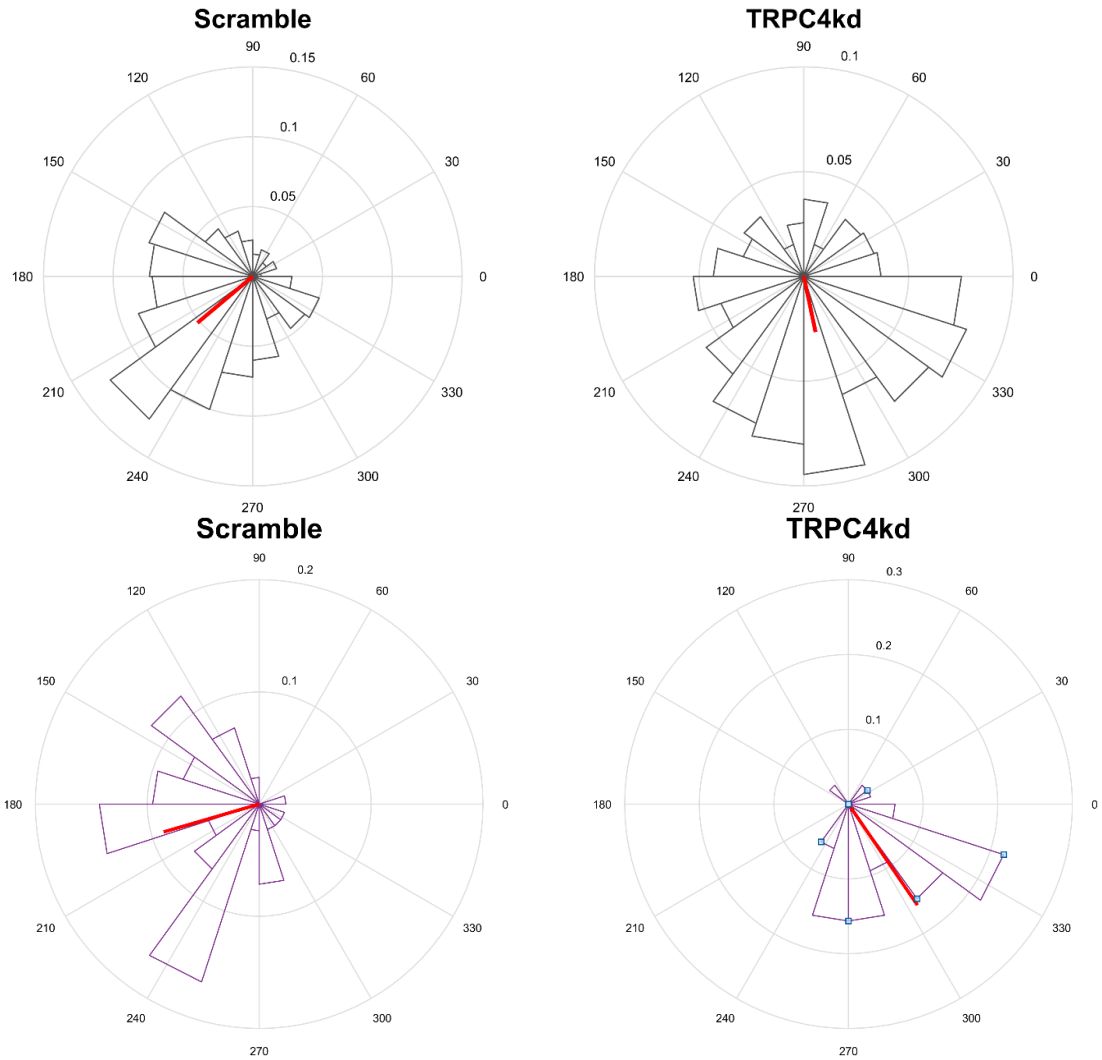

Figure 3.4.2.7: Spike theta phase histogram in the starting area. **Top:** Spike theta phase histogram of all cells. Mean phase comparison showed a significant difference (circular mtest, h=1). **Bottom:** Spike theta phase histogram of phase precession cells. No significant difference existed between the groups (Watson Williams test, p=0.4080).

Similar to the start area, spike phase was plotted for all cells and phase precession cells in goal area (Figure 3.4.2.8). This indicates that the mean theta phase differed across all segments between the groups. However, the theta phase of phase precession cells in all segments shows no significant difference between the groups. Furthermore, the results indicate that TRPC4 knockdown affected CA1 pyramidal cells without specifically impacting phase precession cells.

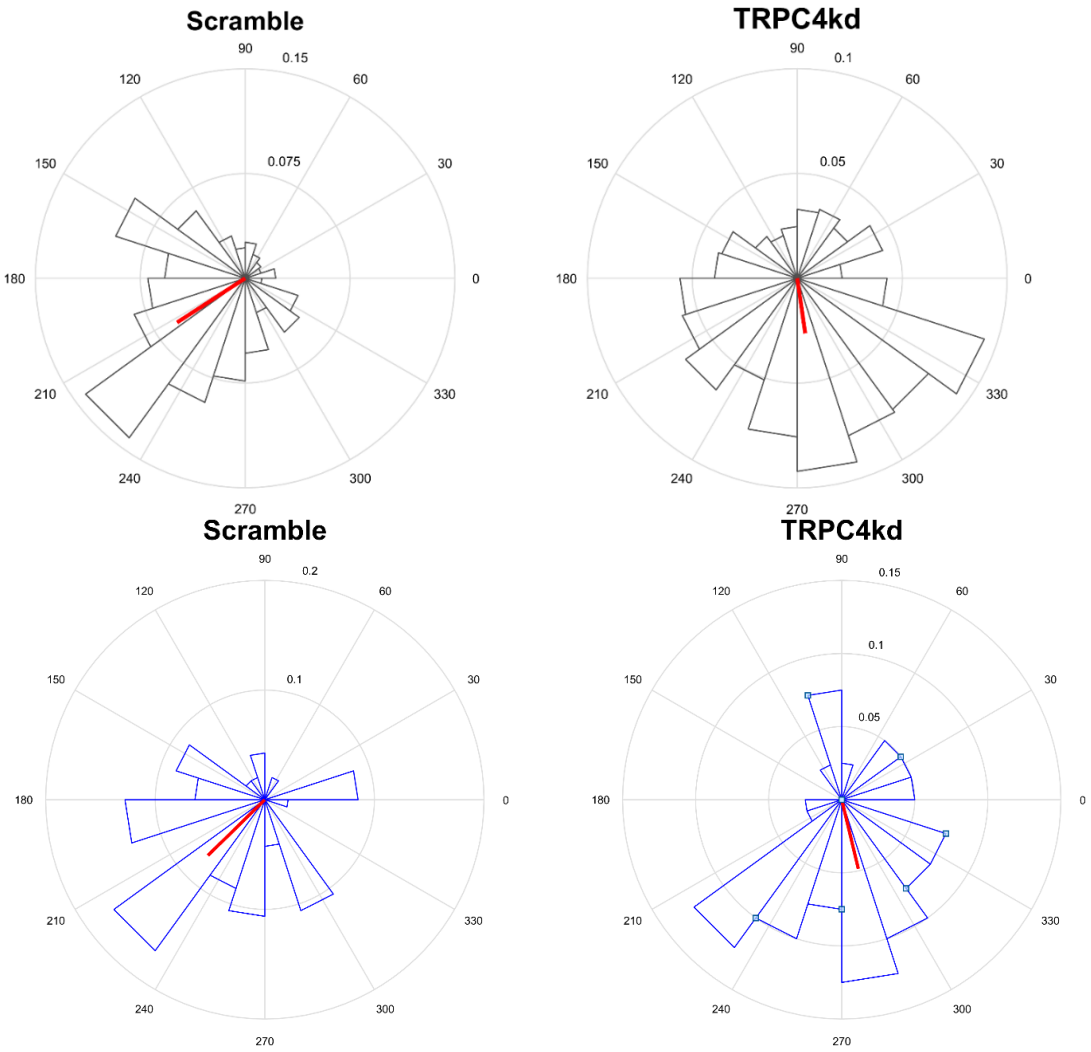

Figure 3.4.2.8: Spike theta phase histogram in the goal area. **Top:** Spike theta phase histogram of all cells. The mean phase comparison showed a significant difference (circular mean test, h=1). **Bottom:** Spike theta phase histogram of phase precession cells. No significant difference existed between the groups (Watson–Williams test, p= 0.7631).

3.4.3 Persistent firing

To investigate the existence of persistent firing as one of the mechanisms involved in working memory during the delay period of the task, the firing rate of all recorded cells was calculated (1 sec bins of delay/average frequency of whole trial). Firing rate was calculated separately for the sample and choice phases when the animals were in the start area. The Masuda et al. (2020) method was used to sort the cells (120). The ratio of delay freq/ trial freq was calculated for each trial, and an overall average was obtained for each trial type (sample, choice). Then, a randomized distribution was built 1000 times by scrambling the time intervals between spikes and calculating the same ratio delay freq/trial freq for each iteration. The original value was compared to the randomized distribution: if the value is above the top 10%, the cell is considered activated; if the value is below the bottom 10%, the cell is labeled as suppressed; between those two boundaries cells are considered nonresponsive; next, the z-scored peak firing rates of the cells were calculated (Figure 3.4.3.1). The results showed that scramble depicted a greater increase or decrease in the firing rate than TRPC4KD (Figure 3.4.3.2). This shows a significant change in the firing properties of TRPC4KD (Wilcoxon rank sum test, $p<0.001$) which may play a role in working memory impairment (Figure 3.4.3.3). Moreover, raster plot examples with firing rate plotted show the spiking patterns during the delay period (Figure 3.4.3.4 & Figure 3.4.3.5). The results show an increase in firing rate, and raster plots verify the increase in firing rate during the delay period.

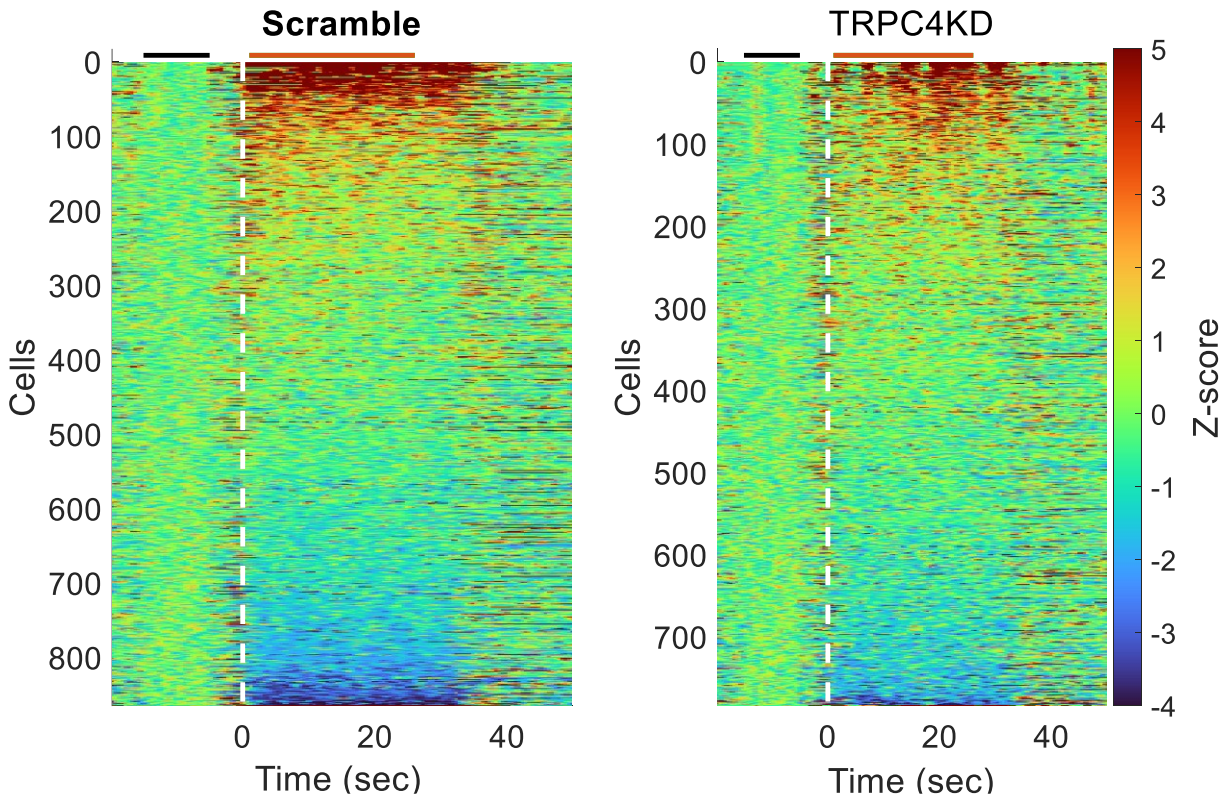

Figure 3.4.3.1: Z-scored peak firing rate of cells in delay period sorted based on firing rate. The top 10 percent cells are shown in red at the top, and the bottom 10 percent cells are shown in blue at the bottom. **Left:** Peak firing rate of cells for scramble. The dashed line shows the delay time. **Right:** Peak firing rate of cells for TRPC4KD.

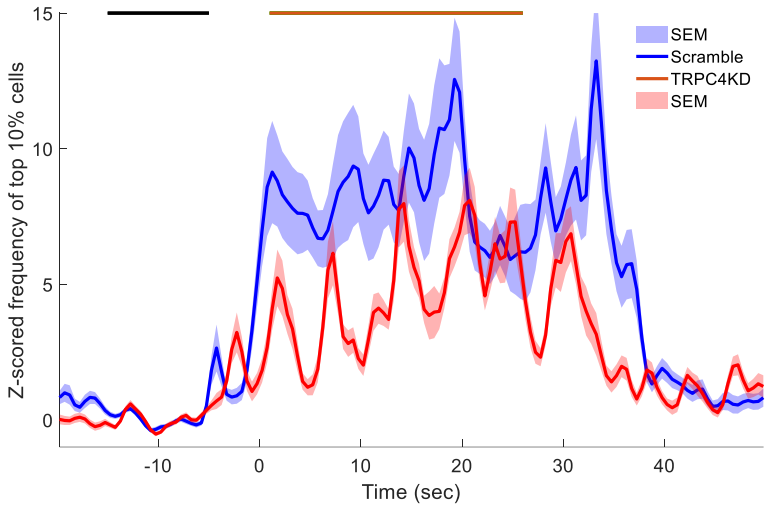

Figure 3.4.3.2: Z-scored firing rate of top 10% cells in the delay phase in the start segment for both groups. Black horizontal line: base line; Orange horizontal line: analyzed duration;

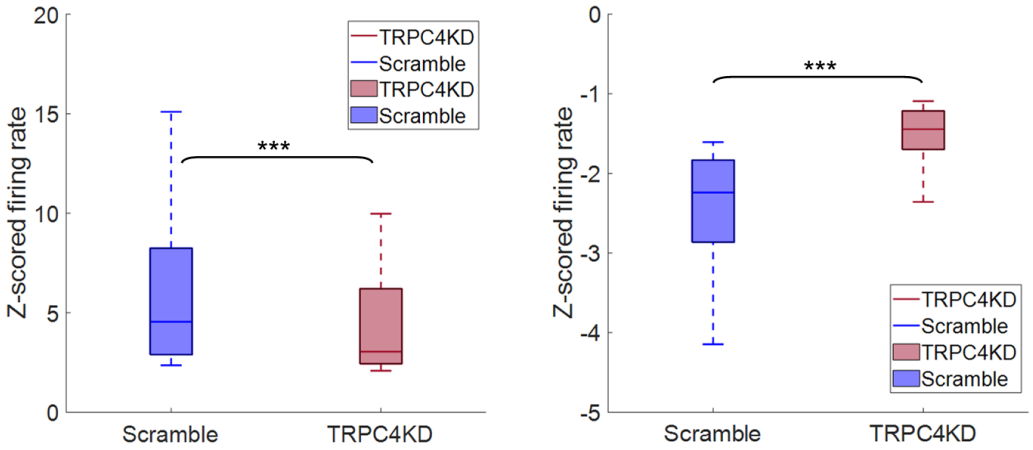

Figure 3.4.3.3: Z-score firing rate of the classified cells in the delay phase in the start segment. **Left:** Top 10% cells z-scored firing rate comparison between the groups (Wilcoxon rank sum test, $p<0.001$, n = 87 for scramble and n = 78 for TRPC4KD). **Right:** Z-scored firing rate comparison of bottom 10% for scramble and TRPC4KD (Wilcoxon rank sum test, $p<0.001$, n = 86 for scramble and n = 78 for TRPC4KD); Blue: scramble; Red: TRPC4KD;

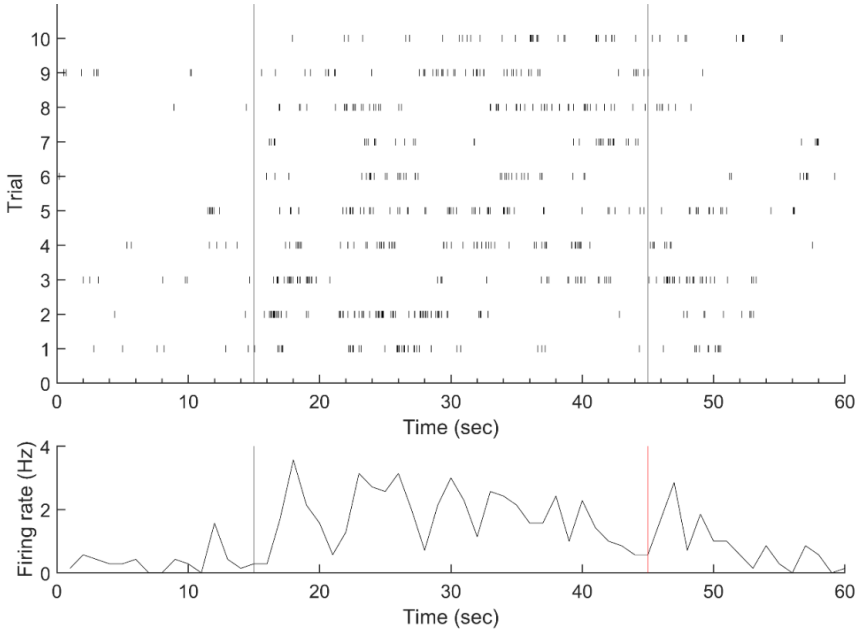

Figure 3.4.3.4: Top: An example raster plot of the delay activated cell during delay period for scramble. Bottom: Cell firing frequency during the delay period.

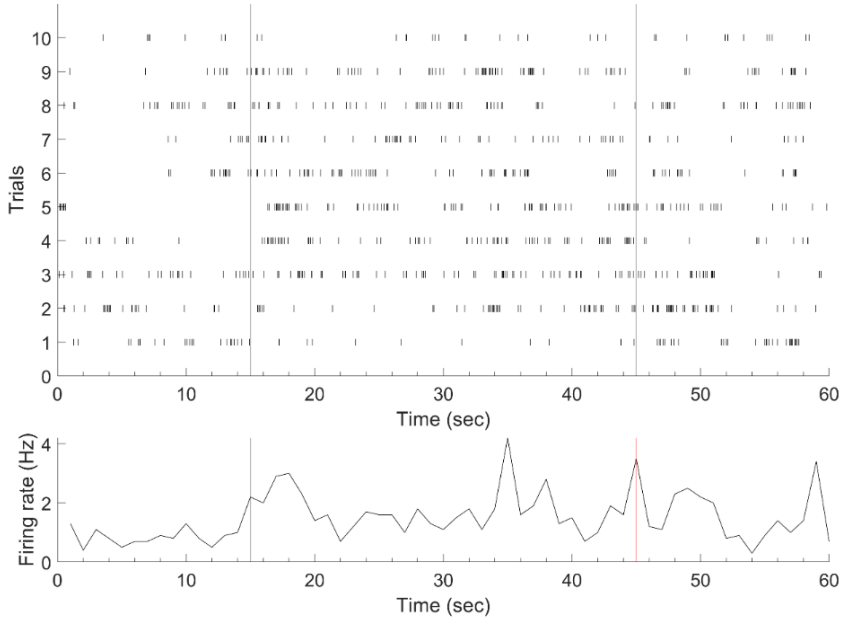

Figure 3.4.3.5: Top: An example raster plot of the delay activated cell during delay period for TRPC4KD. Bottom: Cell firing frequency during the delay period.

Number of each classified cell type was calculated and normalized to determine if the number of cells were changed from sample phase to choice phase (Figure 3.4.3.6). In both groups, the number of cells decreased in the choice phase compared to sample phase. However, the chi-square test result depicted no significant difference in scramble (Figure 3.4.3.6 A and B). In contrast, delay activated and delay suppressed depicted a decrease in TRPC4KD. The normalized count of cells in the choice phase showed a significant difference compared to the sample phase in TRPC4KD (chi-square test, p= 0.0014) (Figure 3.4.4.7 C and D). This suggests that different cells were active in the start area during the sample and choice phases, indicating that distinct circuits may be involved in working memory.

Neuronal activity before delay, during delay, and after delay was analyzed and plotted as a control to investigate if the delay activated cell phenomenon particularly happened in the start area (Figure 3.4.3.7 A & B). As can be seen, the top 10 percent neuronal activity in the return arm and main stem depicts a similar activity in both scramble and TRPC4KD (Wilcoxon rank sum test, p=0.06260 for return arm, p=0.09471 for main stem). Despite this, the delay area demonstrated a significant increased activity in scramble compared to TRPC4KD (Wilcoxon rank sum test, p<0.001). This indicates that the difference in activated cells between the three segments of the T-maze was highly specific to the delay area.

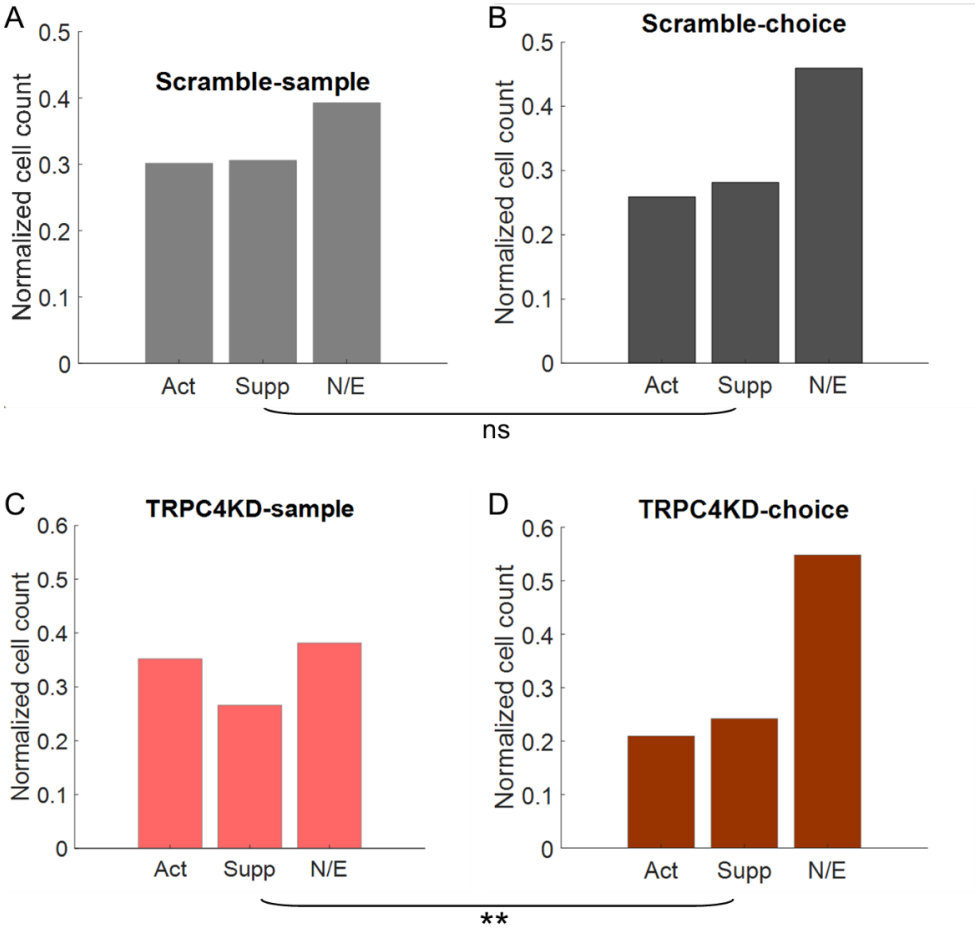

Figure 3.4.3.6: Classification and count of start area cells across task phases in both groups. **A:** Normalized count of cells in the sample phase of the task for the scramble group. **B:** Normalized count of cells in the choice phase of the task for the scramble group. A chi-square test was conducted to assess the relationship between cell activity in the sample and choice phases, indicating no significant difference in cell type counts between the phases. **C:** Normalized count of cells in the sample phase of the task for the TRPC4KD group. **D:** Normalized count of cells in the choice phase of the task for the TRPC4KD group. A chi-square test revealed a significant difference in cell activity between the phases for the TRPC4KD group ($p = 0.0014$, $n = 899$ for scramble sample/choice and $n = 744$ for TRPC4KD sample/choice).

Act: Delay activated; Sup: Delay suppressed; N/E: Others

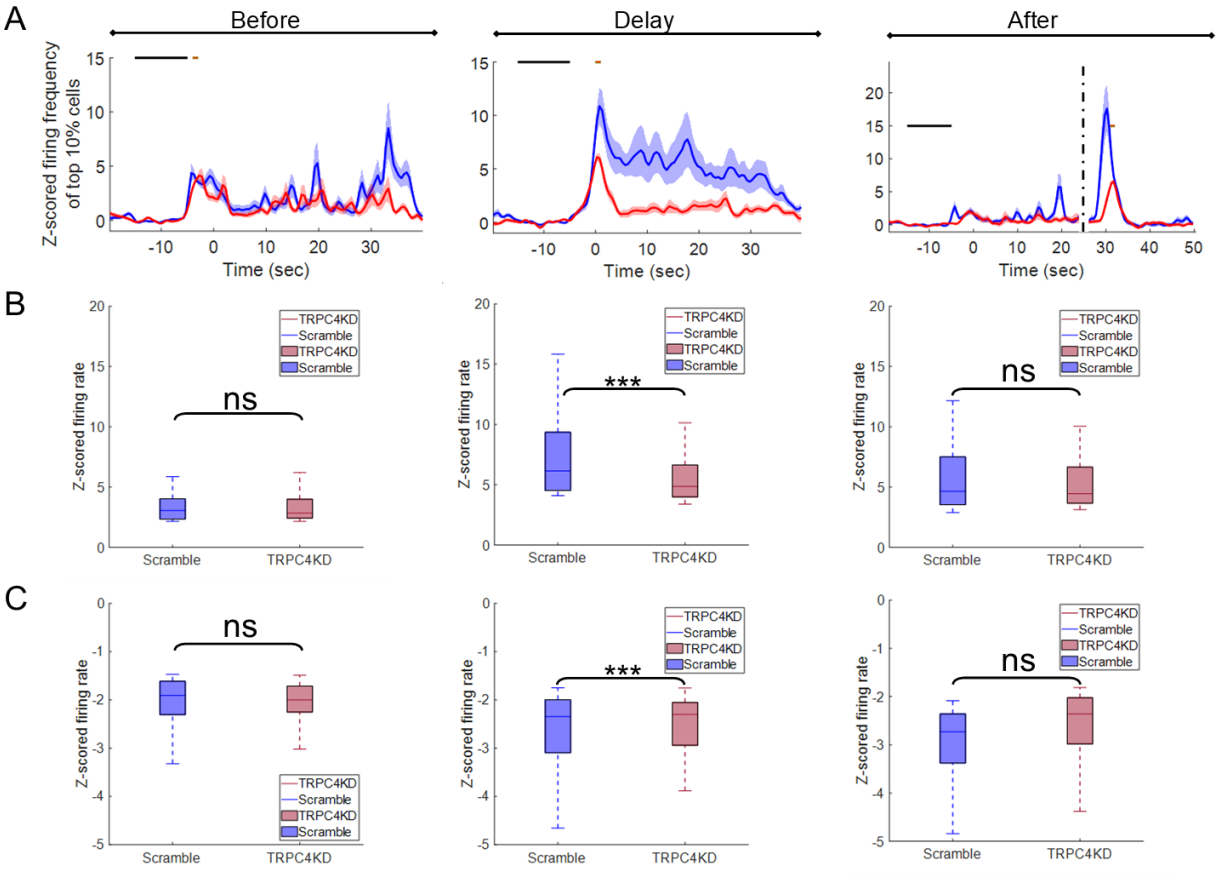

Figure 3.4.3.7: Neuronal activity in return arm, start area and main stem in the choice phase. **A:** Z-scored firing rate of two groups in choice phase in three different segments of the T-maze. The blue line represents scramble and the red line shows TRPC4KD. **B:** Z-scored firing rate of top 10 percent cells in return arm, start and main stem of both groups in choice phase. Only the delay period (start) demonstrated a significant difference between scramble and TRPC4KD (Wilcoxon rank sum test, *P<0.001,* n = 87 for scramble and n = 78 for TRPC4KD). **C:** Z-scored firing rate of bottom 10 percent cells in return arm, start and main stem of both groups in choice phase. Like the top 10% cells in delay period (start), a significant difference can be seen between scramble and TRPC4KD (Wilcoxon rank sum test, *P<0.001,* n = 86 for scramble and n = 78 for TRPC4KD). ns: not significant

3.5 Beta Oscillation Impairment in a Novel Environment

LFP power was measured to study the link and correlation between LFP and encoding in novelty. The LFP data were recorded at the CA1 pyramidal cell layer in the linear track for 20 minutes, and data were analyzed to compare the first and last five minutes of the task. Time-frequency analysis was performed to investigate the power of beta oscillations variation by time. A reduction in beta oscillation power can be seen in the last five minutes of the task compared to the first five minutes for the scramble (control) (Figure 3.5.1). Despite a decrease in beta oscillations for scramble, beta

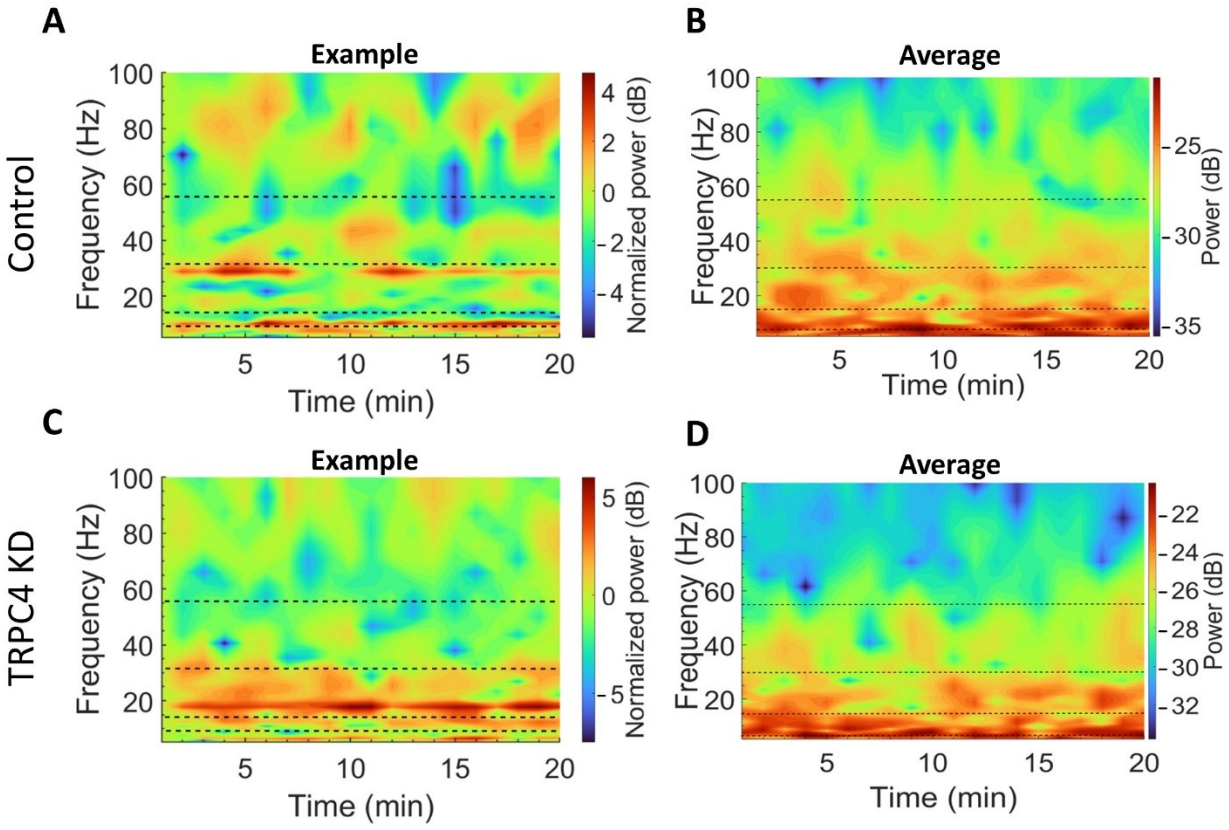

Figure 3.5.1: Time-frequency analysis of LFP. **A,B:** Example and average spectrograms, respectively, from the scramble. **C,D:** Example and average spectrograms, respectively, from the TRPC4 KD. Spectrograms of individual examples (A,C) are normalized to the power at the first minute.

oscillations demonstrated no reduction in power for TRPC4KD. Furthermore, to verify such a decrease, the power of each oscillation band in the first and the last five minutes of the task were compared (Figure 3.5.2 A–D). The analysis depicted that the theta power was raised in the scramble but not in the TRPC4KD when the first and the last five minutes were compared (paired t-test, $p<0.001$ for scramble and $p=0.305$ for TRPC4KD) (Figure 3.5.2 E). A similar comparison depicted that the beta and low-gamma power decreased in the scramble during the LT exposure, while the TRPC4KD preserved the power at these bands (beta, paired t-test, $p<0.05$ for scramble, $p=0.059$ for TRPC4KD) (low-gamma, paired t-test, $p<0.05$ for scramble, $p=0.134$ for TRPC4KD) (Figure 3.5.2. F and G). Unlike beta and low gamma, high gamma and HFO band power showed no significant change in either group (high-gamma, paired t-test, $p=0.630$ for scramble, $p=0.419$ for TRPC4 KD; HFO, paired t-test, $p=0.371$ for scramble, $p=0.873$ for TRPC4 KD) (Figure 3.5.2 H and I). Finally, we analyzed the running speed of the mice in the corresponding two five-minute sections (paired t-test, $p<0.05$ for the scramble, $p<0.05$ for TRPC4 KD) (Figure 3.5.2 J). In both groups, a significant decrease in running speed was observed, indicating that the lack of modulation in the TRPC4 KD group is not purely due to different behavior compared to the scramble control group. These results indicate that TRPC4KD impaired the modulation of theta, beta, and low-gamma oscillations in the hippocampal CA1 area during novelty exposure.

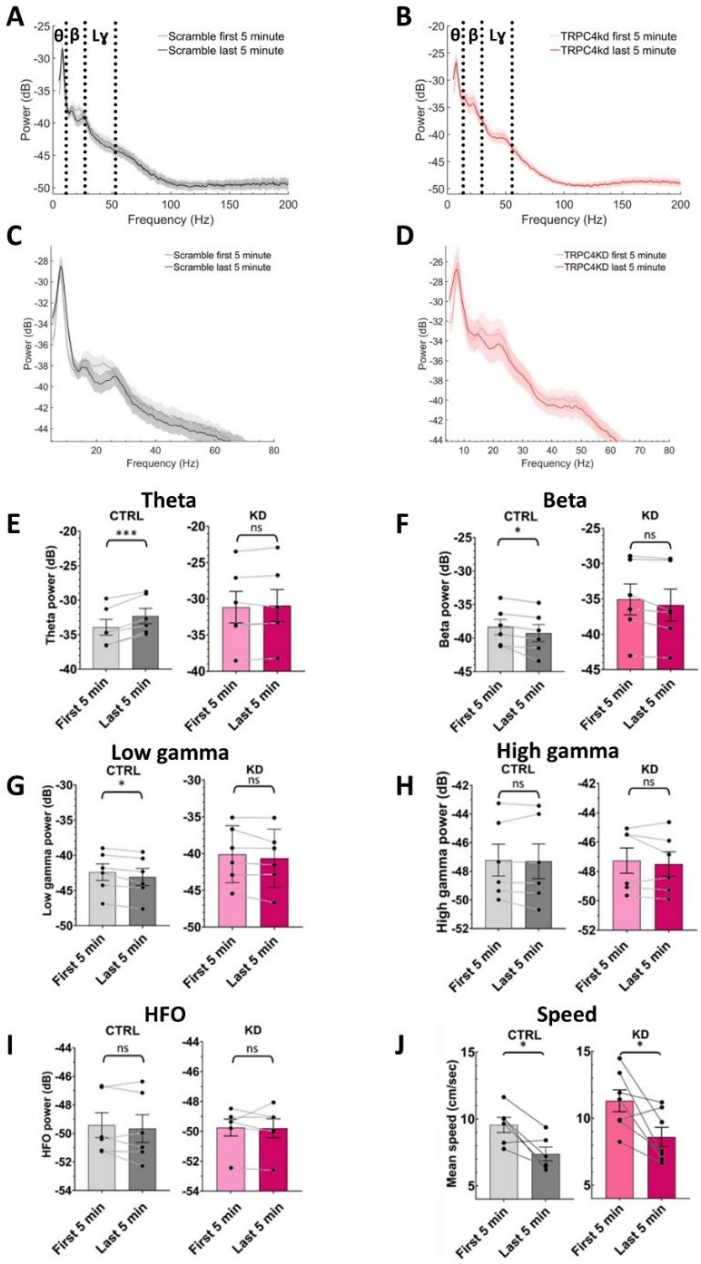

Figure 3.5.2: Comparison of the first and last 5 min of the LT task. **A:** Mean power spectra in the first 5 min and last 5 min for the scramble group. **B:** Mean power spectra in the first 5 min and last 5 min for the TRPC4 KD group. **C and D:** Rescaled power spectra shown in A and B. **E:** Theta oscillations (paired t-test, $p<0.001$ for scramble and $p=0.305$ for TRPC4 KD). **F:** Beta oscillations (paired t-test, $p<0.05$ for scramble, $p=0.059$ for TRPC4 KD). **G:** Low gamma oscillations (paired t-test, $p<0.05$ for scramble. $p=0.134$ for TRPC4 KD). **H:** High gamma oscillations (paired t-test, $p=0.630$ for scramble, $p=0.419$ for TRPC4 KD). **I:** High frequency oscillations (paired t-test, $p=0.371$ for scramble, $p=0.873$ for TRPC4 KD). **J:** Mean of speed during the first five and last five min of the task (paired t-test, $p<0.05$ for scramble, $p<.05$ for TRPC4 KD). In all panels, scramble: n=6; TRPC4 KD, n=6.

3.6 Histology

After finishing the experiments, the animals were perfused and brain samples were sectioned as described in the methods chapter. Next, using a fluorescence microscope, the expression of the virus was checked for all animals, and a map of expression in the brain was prepared based on the correctly injected animals (Figure 3.6.1 and figure 3.6.2). The site of recording for implanted animals was controlled using a fluorescence microscope (Figure 3.6.3).

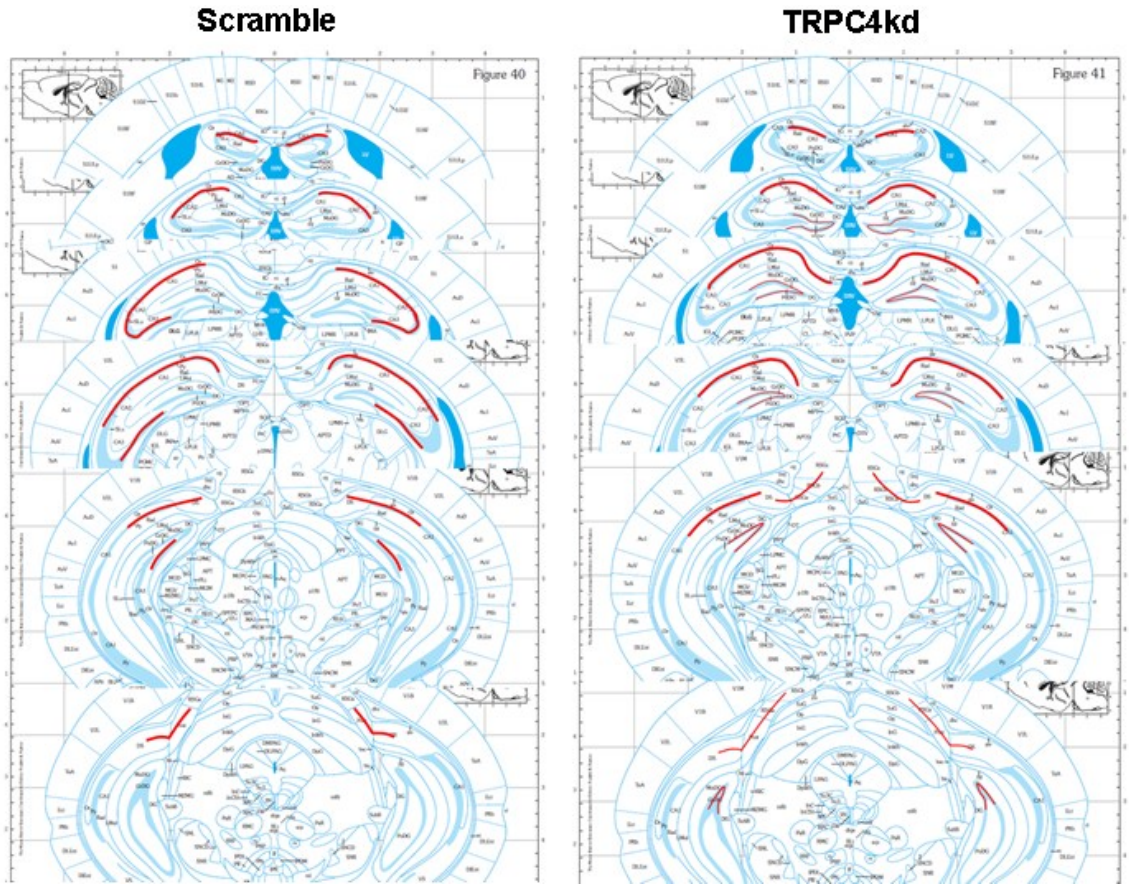

Figure 3.6.1: shRNA scramble and TRPC4KD virus expression in the groups in the coronal plane highlighted in red. **Left:** scramble virus expression in coronal view. **Right:** TRPC4KD expression in coronal view.

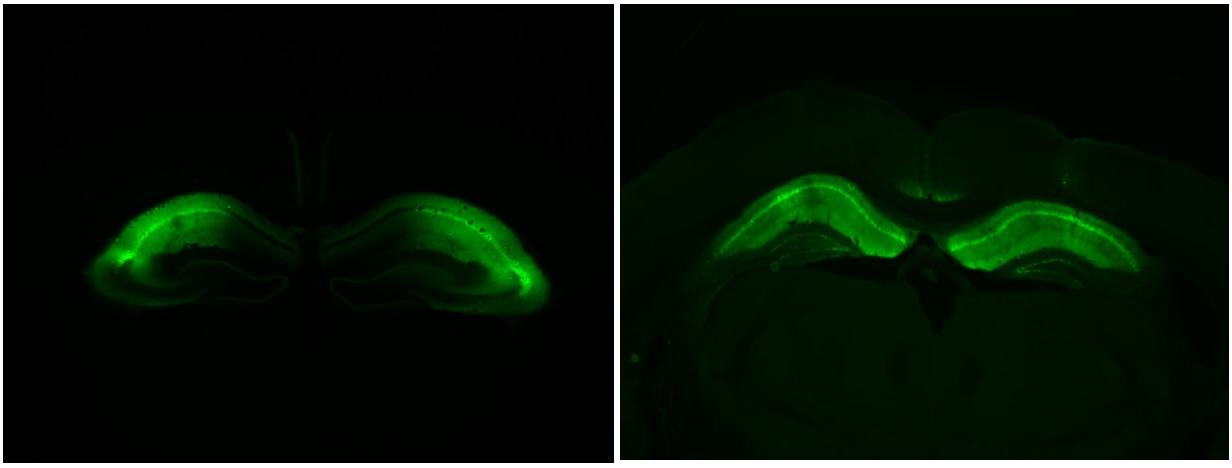

Figure 3.6.2: shRNA expression in the mouse hippocampus coronal sections. **Left:** Scramble virus expression in the hippocampus coronal section. **Right:** TRPC4 shRNA expression in the hippocampus coronal section.

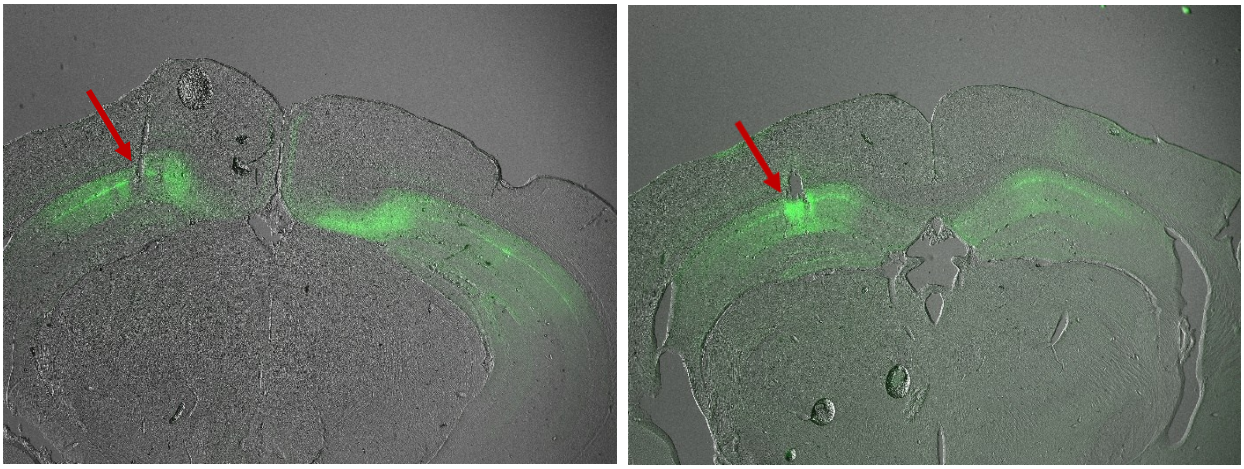

Figure 3.6.3: Microdrive implant control. The tetrode tip lesion is visible on the left side of the figures **Left:** Tetrode recording site in scramble **Right:** Tetrode recording site in TRPC4KD

A minor leakage of virus expression was observed in the DG, which might raise concerns about its impact on the behavioral data. According to the TRPC4 RNA expression map in mice from the Allen Institute (Figure 3.6.4), TRPC4 is predominantly

expressed in the CA1 region, as indicated by the color intensity, compared to the DG. This suggests that any potential leakage of the virus into the DG would have a minimal impact on the results.

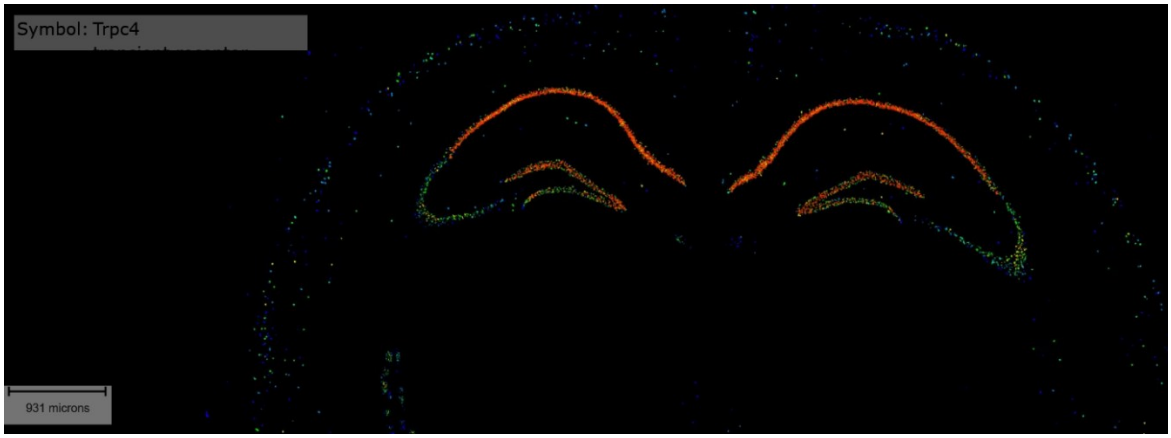

Figure 3.6.4: TRPC4 expression in mouse hippocampus coronal section; image adopted from online Allen atlas. The average expression intensity ranges from blue (low intensity) through green to red (high intensity) (53).

Chapter 4 Discussion

4.1 Working Memory T-maze

The aim of this project was to study the role of TRPC4 in working memory and whether it affects the working memory and through which mechanisms, such as persistent firing, theta-gamma coupling, or a consortium of involved mechanisms. In the present project, I demonstrate that CA1 hippocampal TRPC4 is involved in spatial working memory performance. For this purpose, shRNA TRPC4 was developed to knock down TRPC4 in the CA1 area. The effect of shRNA virus on TRPC4 expression was verified using RT-qPCR in cell culture, reducing TRPC4 gene expression successfully (Figure 3.1.1 & Figure 3.1.2). shRNA TRPC4 was then injected into both hemisphere CA1 areas to study the effect of TRPC4 knockdown in CA1 in spatial working memory. T-maze task utilizing the delayed non-matching to position (DNMTP) protocol was used to assess working memory performance, which was reduced significantly in TRPC4KD compared to scramble (Figure 3.2.1 & Figure 3.2.2). This indicates the effect of TRPC4 knockdown on working memory impairment.

Next, the recorded electrophysiological data using implanted tetrodes were analyzed to study the electrophysiological changes in LFP and single cell levels and find out possible mechanisms involved in impairment in working memory. In the main stem of the T-maze segments, a PSD analysis revealed higher power in the beta oscillation band, as determined by machine learning classification (Figure 3.3.9). This finding suggests a potential role for beta oscillations in the neural processes associated with navigating the T-maze. In contrast, other oscillations, such as theta, low gamma, and high gamma, did not exhibit any significant differences between the conditions. This selective change in beta power and an increase in correct trials (Figure 3.3.7) may indicate a specific effect of TRPC4 on LFPs.

Theta-gamma coupling was measured using the MI. Theta-gamma coupling is proposed as one of the main mechanisms involved in working memory, with higher MI correlating with better performance. The data show a statistically significant correlation between MI and working memory. The mean MI in scramble was higher in high gamma

frequency compared to that of TRPC4KD (Figure 3.3.2.3). Moreover, power phase analysis demonstrated a theta phase-specific increase in low gamma and high gamma frequencies in scramble, while no theta phase-related elevation in low and high gamma power was noted for TRPC4KD (Figure 3.3.2.4). In addition, MI analysis in T-maze segments according to trajectory order (including the start and goal area) and trial performance (correct/incorrect) showed no change in MI in high gamma frequency (Figure 3.3.2.9). However, group comparison of high gamma oscillations in start and goal segments in the sample and choice phases revealed a significant difference for both correct and incorrect trials (Figure 3.3.2.10) (Kruskal–Wallis test followed by post-hoc Dunn's test, with significance levels denoted as a: $p < 0.0001$, b: $p < 0.0001$, c: $p < 0.0001$, e: $p < 0.0001$, f: $p < 0.0001$, g: $p < 0.0001$, and h: $p < 0.0001$, respectively). These results indicate that theta-gamma coupling was impaired in TRPC4KD, and it influences the working memory function.

Single unit analysis was started by calculating spatial information for pyramidal cells. Spatial information depicted significant differences between the groups (Figure 3.4.1.3). Moreover, the firing rate of the pyramidal cells showed no difference (1-5 Hz) between scramble and TRPC4KD. Both effects may originate from TRPC4 knockdown in TRPC4KD.

As the next step, the phase precession in the cells for entire T-maze was analyzed. It is well known that place cells show phase precession with theta oscillation phase, and it is related to time or location. However, the mechanism controlling phase precession is unclear. The spike theta phase analysis (part of phase precession analysis) exhibits differences in the mean theta phase of spikes between the groups (Figure 3.4.2.3). This indicates a unidirectional distribution for TRPC4KD. The change in spike phase could affect LTP/LTD and STDP, and this could consequently modulate memory function and performance.

As the last step, the start area was chosen to study the existence of persistent firing during the delay period of the task. Based on Masuda et al. (2020), the cells were classified into delay activated, delay suppressed, and not modulated cells. Scramble presented a greater increase or decrease in firing rate than TRPC4KD (Figure 3.4.3.1

and Figure 3.4.3.2). After z-scoring the data, scramble showed a stronger firing rate than TRPC4KD during delay in start segment, unlike in return arm or main stem (Figure 3.4.3.3, Figure 3.4.3.7). The firing rate change was not the same as previous persistent firing works in the PFC. Persistent firing cells should show consistent firing during the delay period, which was not the case in my delay period data. Hence, there was no strong evidence supporting persistent activity during the delay period in the start area, although the main challenge to interpret the results is that persistent activity needs to be distinguished from place cell activity. Unlike other brain areas such as the PFC, in the hippocampus, place cells are the active cells (may support persistent firing) engaged in location-associated activity, providing an internal map that supports hippocampus-dependent spatial memory tasks (121).

The working memory performance of TRPC4KD mice in the T-maze was impaired, and they were unable to improve their performance compared to the scramble group over the course of the experiment. The behavioral results illustrate that TRPC4KD impairs working memory performance. The results were similar to the studies by Bröker-Lai and colleagues (51) on *Trpc1/4/5*$^{-/-}$ mice and Lepannetier and colleagues (122) on Trpc1$^{-/-}$ mice. Another study reported spatial memory impairment in IL-10 KO mice. They found that TRPC4 and TRPC5 were decreased in the hippocampus (123). Downregulation of TRPC6 in the DG impaired spatial memory in Y-maze (124). In this project, I used shRNA TRPC4KD instead of the general knockout mice used in studies by Bröker-Lai and colleagues (51), Lepannetier and colleagues (122), and Huo and colleagues (123). The shRNA allows the local knockdown of the target gene expression in the interested brain region. Moreover, in this study, the spatial working memory task and *in vivo* electrophysiology recording were combined, whereas in the other studies, *in vivo* electrophysiology recording was done in an open field or during sleep.

PSD analysis (Figure 3.3.9) revealed a difference in beta oscillation band power, with such changes linked to memory functions and novelty. The power of beta oscillations increases as spatial selectivity develops in place cells (81). These oscillations can synchronize the firing of hippocampal neurons (81). Additionally, they are associated with the activity of the mid-PFC and the posterior parietal cortex.

Gamma frequency as a key player of theta-gamma modulation was the focus of memory studies, and its role became clear and functional in different types of memory. Notably, gamma power increases during the delay period of working memory in humans (92). Moreover, studies on monkeys and humans reported elevated gamma power and spike-gamma coherence in the hippocampus during successful encoding of a LTM task (92). Gamma oscillations are produced by an ensemble of mechanisms and mainly rely on fast spiking basket cells and gamma-aminobutyric acid $(GABA)_A$, α-amino-3-hydroxy-5-methyl-4-isoxazolepropionic acid (AMPA) receptor mediated excitation. Gamma oscillations in CA1 are generally controlled by entorhinal input and CA3 (125). Yamamoto et al. (2014) and Axmacher et al. (2010) (102) reported that high gamma oscillations synchronized with mEC are required for succeeding in spatial working memory tasks. A study on the hippocampus-PFC revealed that hippocampus gamma input was required for successful cue encoding and memory performance (126,127). Gamma power was elevated specifically in the main stem and the coherence between CA1–CA3 as well (125). Another study proposed that gamma oscillations between two connected areas were involved in information transfer (128). In contrast, a study on rats reported that the gamma power during learning of item–context association tasks was not correlated with performance (129). However, dual-site recording may be required to distinguish the effects of entorhinal and CA3 inputs in CA1. Linking a specific frequency range to behavior is challenging, yet the network activity in CA1 during the working memory task reflects this relationship. Ample evidence supports the pivotal role of gamma oscillations in working memory function.

Theta-gamma coupling has been demonstrated to be an essential mechanism in retaining working memory information (92). The evidence came from Miller (1956) showing that working memory has a limited capacity around 7 ± 2 objects (130). The theta-gamma proportion correlated with memory capacity (131).The gamma cycle might be the key player in setting the working memory limit (98). MI results corroborated those of Lepannetier et al. (2018), although MI was measured in REM sleep. Moreover, in my study, a positive correlation existed between working memory performance and MI (Figure 3.3.2.11). A study on rats reported that theta-gamma comodulation could predict

memory retrieval performance in episodic memory (132). Another study demonstrated a positive correlation between MI and memory performance (129). The key change in the results is gamma oscillations, which affect theta-gamma coupling. Gamma oscillations in CA1 are generally controlled by entorhinal input and CA3. Various studies in animals and humans have related the hippocampus circuits to memory. Axmacher and et al. (2010) (133) reported that theta–beta/gamma coupling markedly increased in the delay period of the working memory task (133). Tort and colleagues (129) also reported that theta-gamma interplay works as memory code. Sufficient studies have implicated theta-gamma coupling as one of the mechanisms involved in working memory. The present findings indicate that theta-gamma coupling diminished in the experimental group during the spatial working memory task—a finding uncovered only this study, as no previous TRPC studies have reported theta-gamma coupling impairment during working memory tasks. The study findings indicate that TRPC4KD impairs working memory through theta-gamma coupling and is also linked to performance.

Spatial information and phase precession represent the characteristics of the place cells. Hippocampal phase precession is present in dorsal CA1 pyramidal neurons when the animal is on a narrow track or less limited arenas (134). The main finding in the phase precession results was different spike theta phase mean and mean vector lengths between the groups. The scramble group demonstrated a directional distribution for spikes representing a phase lock to theta. Moreover, high gamma power correlates with theta phase, and this fits with spiking theta phase in the scramble group in all three main segments. In contrast, the main stem spike phase did not reveal an omnidirectional distribution or a high gamma power phase for TRPC4KD. However, the goal and start area spike phase for TRPC4KD depicted directional distribution with an advanced theta phase compared to the scramble group. Phase precession impairment using cannabinoids was reported to diminish spatial memory in T-maze alternation task. This illustrates that spatial memory is firstly related to the temporal organization of neurons and could be segregated from spatial map stability (135). Phase precession is linked and coupled with gamma oscillation, with changes in gamma oscillation affecting the

spike theta phase (136). Overall, our results indicate different theta spikes between groups in the main stem, which might originate from theta-gamma coupling.

Persistent firing analysis to determine whether sustained firing existed in the CA1 pyramidal cells during the delay period and whether this mechanism was affected by TRPC4 knockdown revealed a change in the firing rate in the pyramidal cells in the start area. The z-score plots revealed a difference between the groups. However, a question arises regarding whether the persistent firing observed in the hippocampus represents place cell activity in CA1, and whether the increase in firing rate is specifically linked to place cells. Consistent with these results, Sabariego and colleagues (137) proposed that persistent firing could not support working memory (137). In primates, sufficient reports showed an increase in the firing rate related to stimulus in the dorsolateral PFC (48,138). In rodents, persistent firing is reported in a few cells during the delay period. Alternatively, the cells fire in a specific time window and form a sequence of firing by the cells that covers the delay period (139). The mPFC cells demonstrated past and future locations during the delay in spatial alternation tasks for rodents when the past and future were twisted (140,141). Our results show an increase in the firing rate in the main stem for the scramble group, but insufficient evidence exists to verify it as persistent firing during the delay period.

Additionally, SI analysis (Figure 3.4.1.5) demonstrated a change in firing rate characteristics of the cells between the groups. This shows that the cells' intrinsic properties might have changed, such as Ca^{2+} transportation. Several studies have reported changes in synaptic transmission via TRPC ko/kd (51,58,122). A previous TRPC study reported Ca^{2+} entry via the TRPC and a decrease in Schaffer collateral-CA1 excitability (122). Another study illustrated a decline in synaptic transmission and firing output in CA1 cells (51). The role of gamma oscillations and coherence between CA1 and CA3 were mentioned in the main stem. Impairment in the spiking of the cells by considering the role of cell firing in memory encoding and retrieval, phase precession, and oscillations during spatial working memory tasks could lead to memory impairment. This means that TRPC4KD could confine Ca^{2+} transportation and could results in an impairment in cell excitability and synaptic plasticity, resulting in gamma oscillations and

phase precession functions in working memory. This results in impairment of memory encoding and retrieval in the T-maze main stem. Furthermore, the mechanisms involved in plasticity require intracellular Ca^{2+} signaling. Time-dependent LTP (t-LTP) engages postsynaptic Ca^{2+} influx via NMDA receptors, which activate protein kinases (142). Thus, calcium is a key player in inducing STDP. This indicates that extracellular calcium may also play a role in forming STDP (142). Therefore, any factor affecting extracellular and intracellular calcium will alter cell firing properties and thus plasticity. Decrease in dendritic spines and postsynaptic density protein 95 (PSD-95) in the DG was demonstrated in shRNA-TRPC6 mice (124). Notably, the present study did not measure synaptic plasticity and Ca^{2+} changes. The machine-learning results illustrated a change in the beta oscillation power in the main stem between the groups. This indicates that the cells' firing properties were affected and could originate from Ca^{2+} transportation alteration based on reported ample evidence.

These were the experiments using *in vivo* electrophysiology and shRNA techniques, and the results obtained point to new questions that require new experiments, which I recommend to be considered for future experiments. First, incorporating different types of working memory tasks to study the effect of behavioral impairment will be worthwhile. Single behavioral tasks may limit the interpretation of the results. Similarly, *in vivo* electrophysiological recording in a second task would help to analyze the dataset and may reveal new aspects of the impairment. Second, the electrophysiology recording was done on the hippocampal CA1 region. Dual-site recording will provide insights into network activity, especially in the medial EC region. Using rats instead of mice may facilitate electrophysiological recordings from both hemispheres, and the T-maze apparatus can be more easily modified for rats compared to mice. A rescue experiment to return TRPC4 expression is useful to verify the developed shRNA virus. For a better understanding of the mechanisms involved, *in vitro* studies on slices to determine LTP and oscillation changes would aid *in vivo* result interpretation.

4.2 Novelty-LT

Recordings in the linear track (LT) were performed to investigate the modulation of beta oscillations in a novel environment by TRPC4. The results indicated a significant difference in beta and low gamma oscillations between the scramble and TRPC4KD groups. Beta frequency oscillations decreased at the end of the task relative to the beginning (Figure 3.5.1 and 3.5.2 A–D & F–G). These results corroborate previous studies reporting an increase in beta oscillation power in novel environments (79–81,109). An increase in the power of beta oscillation occurs with the development of spatial selectivity in place cells (81). Beta oscillations can entrain the spiking activity of hippocampal neurons (81). They are linked to the activity of the mid-PFC and PAR. This suggests that beta oscillations serve as a communication mechanism between brain regions involved in novelty detection (81). Thus, variations in beta oscillations may play a role both within the hippocampus (intrahippocampally) and beyond the hippocampus (extrahippocampally).

Accumulating evidence suggest increased ACh levels in the hippocampus during exploration in a novel context (110,143). Moreover, beta and gamma oscillations were induced by the increased tone of cholinergic receptor activation in hippocampal slice preparations (144). Cholinergic activation of TRPCs is mediated via Gq- and Gi-protein-coupled receptors. The results suggest that the cholinergic modulation of TRPC4 may contribute to beta and gamma oscillation changes in a novel context. Beyond AMPA and NMDA receptors, mGluR I activation is involved in beta oscillation modulation (145,146). Group I mGluR also activates TRPCs through the same Gq and Gi pathways (51,59,147). Our results indicate TRPC4 involvement in beta oscillation modulation. Both cholinergic and group I mGluR agonists lead to Ca^{2+} influx and membrane depolarization in hippocampal pyramidal cells (147). Thus, increased cellular activity during beta oscillations both *in vitro* and *in vivo* (82) requires Ca^{2+} influx. Furthermore, memory encoding via synaptic plasticity is enhanced in a novel contexts, and Ca^{2+} influx is essential for that. Our results suggest that modulation of hippocampal oscillatory activity in novel context via TRPC4s contributes to the encoding of a novel context.

In conclusion, the present study provides neurophysiological evidence verifying the crucial role of the rodent hippocampus in spatial working memory. The results highlight the role of CA1 in working memory functions. Moreover, TRPC4 function is revealed in the working memory and encoding novelty in the CA1 area. Gamma oscillations and theta-gamma coupling were shown to diminish, resulting in working memory impairment. Moreover, the acquired data from the linear track (as a novel environment) demonstrated that beta oscillations in hippocampus CA1 were also modulated by TRPC. These series of impairments diminish spatial working memory and modulate oscillations related to a novel context. Furthermore, based on previous reports, TRPC4 blockage using drugs or genetic manipulation should theoretically trigger Ca^{2+} influx disruption and synaptic plasticity via gamma oscillations. This is a key player, and it affects neuronal activity, oscillations, and consequently synaptic plasticity. Our results indicate that TRPC4 knockdown reduces theta-gamma coupling, contributes to beta oscillations in the hippocampus, changes spike theta phase in the main stem, and firing rate properties; therefore, it may also change plasticity. This could lead to behavioral impairments in spatial working memory tasks, which are hippocampus-dependent and also involved in encoding spatial memories in novel environments.

Summary

Working memory is the ability to retain a small amount of information available for ongoing activities. It is a pivotal hallmark of goal-directed behaviors. Hippocampal formation is one of the pivotal regions in the brain involved in working memory and novelty encoding. TRPC1–7 may be involved in working memory. This study investigated the role of TRPC4 in the hippocampal CA1 area in spatial working memory and LFP modulation in a novel environment. An shRNA virus was developed to knock down TRPC4 in the CA1 area of mice. Four weeks after virus injection, behavioral and electrophysiological data were recorded in T-maze and linear tracks. The behavioral experiment showed a significant decrease in spatial working memory performance. Theta-gamma coupling analysis (modulation index, MI) revealed a significant reduction in theta-gamma coupling for TRPC4KD compared to scramble. Moreover, MI decreased in the delay period of the incorrect trials compared to the correct trials for the scramble group. TRPC4KD single unit analysis revealed a significant difference in cells' spatial information between the groups. Although phase precession analysis showed no significant difference in rho and slope, spike phases differed between the groups. Notably, gamma oscillation impairment could diminish information transport in the working memory and pyramidal cell activity. The change in the spike theta phase could have originated from gamma oscillations based on previous reports showing gamma coupling with phase precession. Furthermore, LFP analysis in a linear track demonstrated that beta oscillation is modulated via hippocampal CA1 TRPC4. TRPCs have been implicated in Ca^{2+} transportation and declining synaptic transmission. Thus, TRPC4 knockdown could diminish neuronal activity and oscillations, possibly disrupting synaptic plasticity. In conclusion, the current study presents neurophysiological evidence verifying the crucial role of the rodent hippocampus in spatial working memory and novelty through TRPC4. Theta-gamma coupling impairment in TRPC4KD was observed exclusively in this study, as it has not been previously reported in working memory tasks. The change in gamma oscillations may also affect plasticity. This could result in behavioral impairment in spatial working memory tasks.

Bibliography

1. Per Andersen, Richard Morris, David Amaral, Tim Bliss and JO. The Hippocampus Book. 2007th ed. Vol. 53, Journal of Chemical Information and Modeling. Oxford University Press; 2013. 1689–1699 p.
2. García-López P, García-Marín V, Freire M. The discovery of dendritic spines by Cajal in 1888 and its relevance in the present neuroscience. Vol. 83, Progress in Neurobiology. 2007. p. 110–30.
3. Bird CM, Burgess N. The hippocampus and memory: Insights from spatial processing. Vol. 9, Nature Reviews Neuroscience. Nature Publishing Group; 2008. p. 182–94.
4. Preston AR, Eichenbaum H. Interplay of hippocampus and prefrontal cortex in memory. Vol. 23, Current Biology. Elsevier; 2013. p. R764–73.
5. Bock O. Cajal, Golgi, Nansen, Schäfer and the Neuron Doctrine. Vol. 37, Endeavour. 2013. p. 228–34.
6. Golledge RG. Cognitive Maps. In: Encyclopedia of Social Measurement. Elsevier Inc.; 2004. p. 329–39.
7. Eichenbaum H. The role of the hippocampus in navigation is memory. Vol. 117, Journal of Neurophysiology. American Physiological Society; 2017. p. 1785–96.
8. Bannerman DM, Sprengel R, Sanderson DJ, McHugh SB, Rawlins JNP, Monyer H, et al. Hippocampal synaptic plasticity, spatial memory and anxiety [Internet]. Nature Reviews Neuroscience Nature Publishing Group; Mar, 2014 p. 181–92. Available from: http://www.nature.com/articles/nrn3677
9. Dudchenko PA, Wood ER. Place fields and the cognitive map. Hippocampus [Internet]. 2015 Jun 1 [cited 2022 Jun 28];25(6):709–12. Available from: https://onlinelibrary.wiley.com/doi/10.1002/hipo.22450
10. Kandel E. A Place and a Grid in the Sun. Vol. 159, Cell. Cell Press; 2014. p. 1239–42.
11. BioRender.com. 2021.
12. Knierim JJ. The hippocampus. Curr Biol. 2015 Dec 7;25(23):R1116–21.
13. Schröder H, Moser N, Huggenberger S. The Mouse Hippocampus. Neuroanat Mouse [Internet]. 2020 [cited 2021 Oct 13];267–88. Available from: https://link.springer.com/chapter/10.1007/978-3-030-19898-5_11
14. Vida I. Morphology of Hippocampal Neurons. Hippocampal Microcircuits [Internet]. 2010 [cited 2021 Oct 15];27–67. Available from: https://link.springer.com/chapter/10.1007/978-1-4419-0996-1_2
15. Megías M, Emri Z, Freund TF, Gulyás AI. Total number and distribution of inhibitory and excitatory synapses on hippocampal CA1 pyramidal cells. Neuroscience. 2001 Feb 5;102(3):527–40.

16. N I, WM C, DG A. A quantitative analysis of the dendritic organization of pyramidal cells in the rat hippocampus. J Comp Neurol [Internet]. 1995 [cited 2021 Oct 19];362(1):17–45. Available from: https://pubmed.ncbi.nlm.nih.gov/8576427/

17. Amaral DG, Scharfman HE, Lavenex P. The dentate gyrus: fundamental neuroanatomical organization (dentate gyrus for dummies). Prog Brain Res [Internet]. 2007 [cited 2021 Oct 19];163:3. Available from: /pmc/articles/PMC2492885/

18. Klausberger T. GABAergic interneurons targeting dendrites of pyramidal cells in the CA1 area of the hippocampus. Eur J Neurosci [Internet]. 2009 Sep 1 [cited 2021 Dec 6];30(6):947–57. Available from: https://onlinelibrary.wiley.com/doi/10.1111/j.1460-9568.2009.06913.x

19. Pelkey KA, Chittajallu R, Craig MT, Tricoire L, Wester JC, McBain CJ. Hippocampal gabaergic inhibitory interneurons. Physiol Rev [Internet]. 2017 Oct 1 [cited 2021 Dec 6];97(4):1619–747. Available from: www.prv.org

20. Robert Logie VC. Working Memory: The state of the science [Internet]. Logie R, Camos V, Cowan N, editors. Oxford University Press; 2020 [cited 2021 Dec 8]. Available from: https://oxford.universitypressscholarship.com/view/10.1093/oso/9780198842286.001.0001/oso-9780198842286

21. Chai WJ, Abd Hamid AI, Abdullah JM. Working memory from the psychological and neurosciences perspectives: A review. Vol. 9, Frontiers in Psychology. Frontiers Media S.A.; 2018. p. 401.

22. Baddeley A. Exploring working memory: Selected works of Alan Baddeley. Exploring Working Memory: Selected works of Alan Baddeley. Taylor and Francis; 2017. 1–381 p.

23. Baddeley A. Working memory. Vol. 20, Current Biology. Cell Press; 2010. p. R136–40.

24. Baddeley A. Working Memory, Thought, and Action. Working Memory, Thought, and Action. Oxford University Press; 2012. 1–432 p.

25. Baddeley A. Working Memory: Theories, Models, and Controversies. Annu Rev Psychol [Internet]. 2012 Jan 10 [cited 2021 Dec 10];63(1):1–29. Available from: https://www.annualreviews.org/doi/10.1146/annurev-psych-120710-100422

26. Sanderson DJ, Bannerman DM. The role of habituation in hippocampus-dependent spatial working memory tasks: Evidence from GluA1 AMPA receptor subunit knockout mice. Hippocampus [Internet]. 2012 May 1 [cited 2021 Dec 17];22(5):981–94. Available from: https://onlinelibrary.wiley.com/doi/10.1002/hipo.20896

27. Dudchenko PA. An overview of the tasks used to test working memory in rodents. In: Neuroscience and Biobehavioral Reviews. Pergamon; 2004. p. 699–709.

28. Jackson CE. Cholinergic System. In: Encyclopedia of Clinical Neuropsychology [Internet]. Springer New York; 2011 [cited 2022 Jul 8]. p. 562–4. Available from:

https://link.springer.com/referenceworkentry/10.1007/978-0-387-79948-3_1113

29. Avery MC, Krichmar JL. Neuromodulatory systems and their interactions: A review of models, theories, and experiments. Vol. 11, Frontiers in Neural Circuits. Frontiers Media S.A.; 2017. p. 108.

30. Maurer S V., Williams CL. The cholinergic system modulates memory and hippocampal plasticity via its interactions with non-neuronal cells. Vol. 8, Frontiers in Immunology. Frontiers Media S.A.; 2017. p. 1489.

31. Amemiya S, Redish AD. Hippocampal Theta-Gamma Coupling Reflects State-Dependent Information Processing in Decision Making. Cell Rep [Internet]. 2018 Mar 20 [cited 2022 Jul 29];22(12):3328–38. Available from: https://pubmed.ncbi.nlm.nih.gov/29562187/

32. Volterra A, Meldolesi J. Astrocytes, from brain glue to communication elements: The revolution continues [Internet]. Vol. 6, Nature Reviews Neuroscience. Nature Publishing Group; 2005 [cited 2022 Jul 29]. p. 626–40. Available from: www.nature.com/reviews/neuro

33. Bezzi P, Gundersen V, Galbete JL, Seifert G, Steinhäuser C, Pilati E, et al. Astrocytes contain a vesicular compartment that is competent for regulated exocytosis of glutamate. Nat Neurosci [Internet]. 2004 Jun 23 [cited 2022 Jul 29];7(6):613–20. Available from: http://www.nature.com/natureneuroscience

34. Berman JA, Talmage DA, Role LW. Cholinergic Circuits and Signaling in the Pathophysiology of Schizophrenia [Internet]. Vol. 78, International Review of Neurobiology. NIH Public Access; 2007 [cited 2022 Jul 11]. p. 193–223. Available from: /pmc/articles/PMC2377023/

35. Newman EL, Gupta K, Climer JR, Monaghan CK, Hasselmo ME. Cholinergic modulation of cognitive processing: Insights drawn from computational models [Internet]. Vol. 6, Frontiers in Behavioral Neuroscience. Frontiers Media SA; 2012 [cited 2022 Jul 11]. Available from: /pmc/articles/PMC3374475/

36. Barak O, Tsodyks M. Working models of working memory. Vol. 25, Current Opinion in Neurobiology. Elsevier Current Trends; 2014. p. 20–4.

37. Nyberg L, Eriksson J. Working memory: Maintenance, updating, and the realization of intentions. Cold Spring Harb Perspect Biol [Internet]. 2016 Feb 1 [cited 2022 Jul 14];8(2):a021816. Available from: http://cshperspectives.cshlp.org/

38. Lin C, Sherathiya VN, Matthew Oh M, Disterhoft JF. Persistent firing in lec iii neurons is differentially modulated by learning and aging. Elife [Internet]. 2020 Jul 1 [cited 2022 Jul 13];9:1–30. Available from: /pmc/articles/PMC7371426/

39. Suzuki WA, Miller EK, Desimone R. Object and place memory in the macaque entorhinal cortex. J Neurophysiol [Internet]. 1997 [cited 2022 Jul 15];78(2):1062–81. Available from: https://journals.physiology.org/doi/10.1152/jn.1997.78.2.1062

40. Young BJ, Otto T, Fox GD, Eichenbaum H. Memory representation within the parahippocampal region. J Neurosci [Internet]. 1997 Jul 7 [cited 2022 Jul 15];17(13):5183–95. Available from: /pmc/articles/PMC6573311/

41. Fuster JM, Alexander GE. Neuron activity related to short-term memory. Science (80-) [Internet]. 1971 Aug 13 [cited 2022 Jul 14];173(3997):652–4. Available from: https://www.science.org/doi/10.1126/science.173.3997.652

42. Freichel M, Vennekens R, Olausson J, Stolz S, Philipp SE, Weißgerber P, et al. Functional role of TRPC proteins in native systems: Implications from knockout and knock-down studies. J Physiol [Internet]. 2005 Aug 15 [cited 2022 Jan 19];567(1):59–66. Available from: /pmc/articles/PMC1474153/

43. Zylberberg J, Strowbridge BW. Mechanisms of Persistent Activity in Cortical Circuits: Possible Neural Substrates for Working Memory. Annu Rev Neurosci [Internet]. 2017 Jul 25 [cited 2022 Jan 28];40:603–27. Available from: https://doi.org/10.1146/annurev-neuro-070815-

44. Egorov A V., Hamam BN, Fransén E, Hasselmo ME, Alonso AA. Graded persistent activity in entorhinal cortex neurons. Nature [Internet]. 2002 Nov 14 [cited 2018 Apr 3];420(6912):173–8. Available from: http://www.nature.com/doifinder/10.1038/nature01171

45. Yoshida M, Hasselmo ME. Persistent firing supported by an intrinsic cellular mechanism in a component of the head direction system. J Neurosci [Internet]. 2009 Apr 15 [cited 2022 Jul 14];29(15):4945–52. Available from: https://www.jneurosci.org/content/29/15/4945

46. Jochems A, Yoshida M. Persistent firing supported by an intrinsic cellular mechanism in hippocampal CA3 pyramidal cells. Eur J Neurosci [Internet]. 2013 Jul 1 [cited 2022 Jul 14];38(2):2250–9. Available from: https://onlinelibrary.wiley.com/doi/10.1111/ejn.12236

47. Navaroli VL, Zhao Y, Boguszewski P, Brown TH. Muscarinic receptor activation enables persistent firing in pyramidal neurons from superficial layers of dorsal perirhinal cortex. Hippocampus [Internet]. 2012 Jun [cited 2018 Apr 3];22(6):1392–404. Available from: http://www.ncbi.nlm.nih.gov/pubmed/21956787

48. Funahashi S, Bruce CJ, Goldman-Rakic PS. Mnemonic coding of visual space in the monkey's dorsolateral prefrontal cortex. J Neurophysiol [Internet]. 1989 [cited 2022 Jul 14];61(2):331–49. Available from: https://pubmed.ncbi.nlm.nih.gov/2918358/

49. Zhang Z, Reboreda A, Alonso A, Barker PA, Séguéla P. TRPC channels underlie cholinergic plateau potentials and persistent activity in entorhinal cortex. Hippocampus [Internet]. 2011 Apr 1 [cited 2022 Jul 14];21(4):386–97. Available from: https://onlinelibrary.wiley.com/doi/10.1002/hipo.20755

50. Trebak M, Lemonnier L, Smyth JT, Vazquez G, Putney JW. Phospholipase C-coupled receptors and activation of TRPC channels. Handb Exp Pharmacol [Internet]. 2007 [cited 2022 Jan 19];179:593–614. Available from: https://link.springer.com/chapter/10.1007/978-3-540-34891-7_35

51. Bröker-Lai J, Kollewe A, Schindeldecker B, Pohle J, Nguyen Chi V, Mathar I, et al. Heteromeric channels formed by TRPC1, TRPC4 and TRPC5 define hippocampal synaptic transmission and working memory. EMBO J [Internet]. 2017 Sep 15 [cited

2018 Mar 23];36(18):2770–89. Available from: http://www.ncbi.nlm.nih.gov/pubmed/28790178

52. Experiment Detail :: Allen Brain Atlas: Mouse Brain [Internet]. [cited 2022 Jan 20]. Available from: http://mouse.brain-map.org/experiment/show/1305

53. Experiment Detail :: Allen Brain Atlas: Mouse Brain [Internet]. [cited 2022 Jan 20]. Available from: http://mouse.brain-map.org/experiment/show/1306

54. Fowler MA, Sidiropoulou K, Ozkan ED, Phillips CW, Cooper DC. Corticolimbic Expression of TRPC4 and TRPC5 Channels in the Rodent Brain. McCabe B, editor. PLoS One [Internet]. 2007 Jun 27 [cited 2018 Apr 3];2(6):e573. Available from: http://dx.plos.org/10.1371/journal.pone.0000573

55. Cavalié A. Ionic channels formed by TRPC4. Handb Exp Pharmacol. 2007;179:93–108.

56. Kiselyov K, Shin DM, Kim JY, Yuan JP, Muallem S. TRPC channels: Interacting proteins. Handb Exp Pharmacol [Internet]. 2007 [cited 2022 Jan 24];179:559–74. Available from: https://link.springer.com/chapter/10.1007/978-3-540-34891-7_33

57. Wang H, Cheng X, Tian J, Xiao Y, Tian T, Xu F, et al. TRPC channels: Structure, function, regulation and recent advances in small molecular probes. May 1, 2020 p. 107497.

58. Schwarz Y, Oleinikov K, Schindeldecker B, Wyatt A, Weißgerber P, Flockerzi V, et al. TRPC channels regulate Ca2+-signaling and short-term plasticity of fast glutamatergic synapses. Demb J, editor. PLOS Biol [Internet]. 2019 Sep 19 [cited 2022 Jan 18];17(9):e3000445. Available from: https://dx.plos.org/10.1371/journal.pbio.3000445

59. Gualdani R, Gailly P. How TRPC channels modulate hippocampal function [Internet]. Vol. 21, International Journal of Molecular Sciences. MDPI AG; 2020 [cited 2022 Jan 27]. p. 1–19. Available from: https://pubmed.ncbi.nlm.nih.gov/32486187/

60. Reboreda A, Jiménez-Díaz L, Navarro-López JD. TRP channels and neural persistent activity. In: Advances in Experimental Medicine and Biology [Internet]. Springer New York LLC; 2011 [cited 2022 Jul 29]. p. 595–613. Available from: https://link.springer.com/chapter/10.1007/978-94-007-0265-3_32

61. Mrejeru A, Wei A, Ramirez JM. Calcium-activated non-selective cation currents are involved in generation of tonic and bursting activity in dopamine neurons of the substantia nigra pars compacta. J Physiol [Internet]. 2011 May 5 [cited 2022 Jul 29];589(10):2497–514. Available from: /pmc/articles/PMC3115821/

62. Yoshida M, Fransén E, Hasselmo ME. mGluR-dependent persistent firing in entorhinal cortex layer III neurons. Eur J Neurosci [Internet]. 2008 Sep [cited 2022 Jul 15];28(6):1116–26. Available from: /pmc/articles/PMC2584367/

63. Klink R, Alonso A. Morphological characteristics of layer II projection neurons in the rat medial entorhinal cortex. Hippocampus [Internet]. 1997 Jan 1 [cited 2022 Jul 15];7(5):571–83. Available from: https://onlinelibrary.wiley.com/doi/10.1002/(SICI)1098-

1063(1997)7:5%3C571::AID-HIPO12%3E3.0.CO;2-Y

64. Reboreda A, Raouf R, Alonso A, Séguéla P. Development of Cholinergic Modulation and Graded Persistent Activity in Layer V of Medial Entorhinal Cortex. J Neurophysiol [Internet]. 2007 Jun [cited 2022 Jul 15];97(6):3937–47. Available from: https://www.physiology.org/doi/10.1152/jn.01233.2006

65. Zhang Z, Seguela P. Metabotropic Induction of Persistent Activity in Layers II/III of Anterior Cingulate Cortex. Cereb Cortex [Internet]. 2010 Dec 1 [cited 2022 Jul 15];20(12):2948–57. Available from: https://academic.oup.com/cercor/article-lookup/doi/10.1093/cercor/bhq043

66. Egorov A V., Schumacher D, Medert R, Birnbaumer L, Freichel M, Draguhn A. TRPC channels are not required for graded persistent activity in entorhinal cortex neurons. Hippocampus [Internet]. 2019 Nov 19 [cited 2022 Jul 15];29(11):1038–48. Available from: https://onlinelibrary.wiley.com/doi/10.1002/hipo.23094

67. Lundqvist M, Herman P, Miller EK. Working memory: Delay activity, yes! persistent activity? maybe not. J Neurosci. 2018 Aug 8;38(32):7013–9.

68. Li S, Zhou X, Constantinidis C, Qi XL. Plasticity of Persistent Activity and Its Constraints. Vol. 14, Frontiers in Neural Circuits. Frontiers Media S.A.; 2020. p. 15.

69. Hanslmayr S, Staudigl T. How brain oscillations form memories - A processing based perspective on oscillatory subsequent memory effects. Vol. 85, NeuroImage. Academic Press Inc.; 2014. p. 648–55.

70. Düzel E, Penny WD, Burgess N. Brain oscillations and memory. Vol. 20, Current Opinion in Neurobiology. Elsevier Ltd; 2010. p. 143–9.

71. Hanslmayr S, Staresina BP, Bowman H. Oscillations and Episodic Memory: Addressing the Synchronization/Desynchronization Conundrum [Internet]. Vol. 39, Trends in Neurosciences. Elsevier Ltd; 2016 [cited 2022 Aug 1]. p. 16–25. Available from: /pmc/articles/PMC4819444/

72. Jensen O, Lisman JE. Hippocampal sequence-encoding driven by a cortical multi-item working memory buffer. Trends Neurosci. 2005 Feb 1;28(2):67–72.

73. Gloveli T, Kopell N, Dugladze T. Neuronal Activity Patterns During Hippocampal Network Oscillations In Vitro. In: Hippocampal Microcircuits [Internet]. Springer New York; 2010 [cited 2021 Dec 20]. p. 247–76. Available from: https://link.springer.com/chapter/10.1007/978-1-4419-0996-1_8

74. Buzsáki G. Theta oscillations in the hippocampus. Vol. 33, Neuron. Cell Press; 2002. p. 325–40.

75. Pignatelli M, Beyeler A, Leinekugel X. Neural circuits underlying the generation of theta oscillations. J Physiol Paris. 2012 May 1;106(3–4):81–92.

76. Huh CYL, Goutagny R, Williams S. Glutamatergic neurons of the mouse medial septum and diagonal band of broca synaptically drive hippocampal pyramidal cells: Relevance for hippocampal theta rhythm. J Neurosci [Internet]. 2010 Nov 24 [cited 2021 Dec 23];30(47):15951–61. Available from: www.jneurosci.org

77. Deshmukh SS, Yoganarasimha D, Voicu H, Knierim JJ. Theta modulation in the medial and the lateral entorhinal cortices. J Neurophysiol [Internet]. 2010 Aug [cited 2021 Dec 24];104(2):994–1006. Available from: www.jn.org

78. Gattas S, Elias GA, Janecek J, Yassa MA, Fortin NJ. Proximal CA1 20-40 Hz power dynamics reflect trial-specific information processing supporting nonspatial sequence memory. Elife. 2022 May 1;11.

79. Berke JD, Hetrick V, Breck J, Greene RW. Transient 23–30 Hz oscillations in mouse hippocampus during exploration of novel environments. Hippocampus [Internet]. 2008 May 1 [cited 2023 Feb 28];18(5):519–29. Available from: https://onlinelibrary.wiley.com/doi/full/10.1002/hipo.20435

80. Iwasaki S, Sasaki T, Ikegaya Y. Hippocampal beta oscillations predict mouse object-location associative memory performance. Hippocampus [Internet]. 2021 May 8 [cited 2022 Aug 4];31(5):503–11. Available from: https://onlinelibrary.wiley.com/doi/10.1002/hipo.23311

81. França ASC, Borgesius NZ, Souza BC, Cohen MX. Beta2 Oscillations in Hippocampal-Cortical Circuits During Novelty Detection. Front Syst Neurosci. 2021 Feb 16;15:8.

82. Bibbig A, Middleton S, Racca C, Gillies MJ, Garner H, LeBeau FEN, et al. Beta rhythms (15-20 Hz) generated by nonreciprocal communication in hippocampus. J Neurophysiol [Internet]. 2007 Apr [cited 2023 Feb 28];97(4):2812–23. Available from: https://journals.physiology.org/doi/10.1152/jn.01105.2006

83. Buzśaki G, Wang XJ. Mechanisms of gamma oscillations [Internet]. Vol. 35, Annual Review of Neuroscience. Annual Reviews ; 2012 [cited 2022 Jan 3]. p. 203–25. Available from: http://www.annualreviews.org.

84. Colgin LL, Denninger T, Fyhn M, Hafting T, Bonnevie T, Jensen O, et al. Frequency of gamma oscillations routes flow of information in the hippocampus. Nature [Internet]. 2009 Nov 19 [cited 2022 Jan 3];462(7271):353–7. Available from: https://www.nature.com/articles/nature08573

85. Butler JL, Hay YA, Paulsen O. Comparison of three gamma oscillations in the mouse entorhinal–hippocampal system. Eur J Neurosci [Internet]. 2018 Oct 1 [cited 2022 Jan 4];48(8):2795–806. Available from: https://pubmed.ncbi.nlm.nih.gov/29356162/

86. Mably AJ, Colgin LL. Gamma oscillations in cognitive disorders. Vol. 52, Current Opinion in Neurobiology. Elsevier Ltd; 2018. p. 182–7.

87. Zheng C, Bieri KW, Hsiao YT, Colgin LL. Spatial Sequence Coding Differs during Slow and Fast Gamma Rhythms in the Hippocampus. Neuron. 2016 Jan 20;89(2):398–408.

88. Colgin LL. Rhythms of the hippocampal network. Vol. 17, Nature Reviews Neuroscience. Nature Publishing Group; 2016. p. 239–49.

89. Carr MF, Karlsson MP, Frank LM. Transient Slow Gamma Synchrony Underlies Hippocampal Memory Replay. Neuron. 2012 Aug 23;75(4):700–13.

90. Colgin LL, Moser EI. Gamma oscillations in the hippocampus. Vol. 25, Physiology. 2010. p. 319–29.

91. Zheng C, Bieri KW, Hwaun E, Colgin LL. Fast gamma rhythms in the hippocampus promote encoding of novel object-place pairings. eNeuro [Internet]. 2016 Mar 1 [cited 2022 Jan 12];3(2):3089–96. Available from: http://dx.doi.org/10.1523/ENEURO.0001-16.2016

92. Lisman JE, Jensen O. The Theta-Gamma Neural Code [Internet]. Vol. 77, Neuron. NIH Public Access; 2013 [cited 2022 Aug 18]. p. 1002–16. Available from: /pmc/articles/PMC3648857/

93. De Almeida L, Idiart M, Lisman JE. A second function of gamma frequency oscillations: An E%-max winner-take-all mechanism selects which cells fire. J Neurosci [Internet]. 2009 Jun 10 [cited 2022 Aug 22];29(23):7497–503. Available from: /pmc/articles/PMC2758634/

94. Papale AE, Zielinski MC, Frank LM, Jadhav SP, Redish AD. Interplay between Hippocampal Sharp-Wave-Ripple Events and Vicarious Trial and Error Behaviors in Decision Making. Neuron [Internet]. 2016 Dec 7 [cited 2022 Jan 14];92(5):975–82. Available from: https://pubmed.ncbi.nlm.nih.gov/27866796/

95. Oliva A, Fernández-Ruiz A, Fermino de Oliveira E, Buzsáki G. Origin of Gamma Frequency Power during Hippocampal Sharp-Wave Ripples. Cell Rep [Internet]. 2018 Nov 13 [cited 2022 Jan 17];25(7):1693-1700.e4. Available from: https://pubmed.ncbi.nlm.nih.gov/30428340/

96. Zhang Y, Cao L, Varga V, Jing M, Karadas M, Li Y, et al. Cholinergic suppression of hippocampal sharp-wave ripples impairs working memory. Proc Natl Acad Sci U S A [Internet]. 2021 Apr 13 [cited 2022 Jan 17];118(15). Available from: https://doi.org/10.1073/pnas.2016432118

97. Roumis DK, Frank LM. Hippocampal sharp-wave ripples in waking and sleeping states [Internet]. Vol. 35, Current Opinion in Neurobiology. Elsevier Ltd; 2015 [cited 2022 Jan 18]. p. 6–12. Available from: https://pubmed.ncbi.nlm.nih.gov/26011627/

98. Lisman JE, Idiart MAP. Storage of 7 ± 2 short-term memories in oscillatory subcycles. Science (80-) [Internet]. 1995 Mar 10 [cited 2022 Jan 31];267(5203):1512–5. Available from: https://www.science.org/doi/10.1126/science.7878473

99. Colgin LL. Theta-gamma coupling in the entorhinal-hippocampal system. Vol. 31, Current Opinion in Neurobiology. Elsevier Ltd; 2015. p. 45–50.

100. Lisman J. Working memory: The importance of theta and gamma oscillations. Vol. 20, Current Biology. Cell Press; 2010. p. R490–2.

101. Tort ABL, Kramer MA, Thorn C, Gibson DJ, Kubota Y, Graybiel AM, et al. Dynamic cross-frequency couplings of local field potential oscillations in rat striatum and hippocampus during performance of a T-maze task. Proc Natl Acad Sci U S A [Internet]. 2008 Dec 23 [cited 2019 Mar 25];105(51):20517–22. Available from: http://www.ncbi.nlm.nih.gov/pubmed/19074268

102. Yamamoto J, Suh J, Takeuchi D, Tonegawa S. Successful execution of working memory linked to synchronized high-frequency gamma oscillations. Cell [Internet]. 2014 May 8 [cited 2022 Jul 28];157(4):845–57. Available from: https://pubmed.ncbi.nlm.nih.gov/24768692/

103. Wittmann BC, Bunzeck N, Dolan RJ, Düzel E. Anticipation of novelty recruits reward system and hippocampus while promoting recollection. Neuroimage [Internet]. 2007 Oct 15 [cited 2023 Apr 27];38(1):194–202. Available from: https://pubmed.ncbi.nlm.nih.gov/17764976/

104. Larkin MC, Lykken C, Tye LD, Wickelgren JG, Frank LM. Hippocampal output area CA1 broadcasts a generalized novelty signal during an object-place recognition task. Hippocampus [Internet]. 2014 Jul 1 [cited 2023 Mar 13];24(7):773–83. Available from: https://onlinelibrary.wiley.com/doi/full/10.1002/hipo.22268

105. Gómez-Ocádiz R, Trippa M, Zhang CL, Posani L, Cocco S, Monasson R, et al. A synaptic signal for novelty processing in the hippocampus. Nat Commun 2022 131 [Internet]. 2022 Jul 15 [cited 2023 Apr 27];13(1):1–15. Available from: https://www.nature.com/articles/s41467-022-31775-6

106. Kafkas A, Montaldi D. How do memory systems detect and respond to novelty? Neurosci Lett [Internet]. 2018 Jul 7 [cited 2023 Apr 27];680:60. Available from: /pmc/articles/PMC6565889/

107. Chen S, He L, Huang AJY, Boehringer R, Robert V, Wintzer ME, et al. A hypothalamic novelty signal modulates hippocampal memory. Nat 2020 5867828 [Internet]. 2020 Sep 30 [cited 2023 Apr 27];586(7828):270–4. Available from: https://www.nature.com/articles/s41586-020-2771-1

108. Fredes F, Shigemoto R. The role of hippocampal mossy cells in novelty detection. Neurobiol Learn Mem. 2021 Sep 1;183:107486.

109. França ASC, do Nascimento GC, Lopes-dos-Santos V, Muratori L, Ribeiro S, Lobão-Soares B, et al. Beta2 oscillations (23–30 Hz) in the mouse hippocampus during novel object recognition. Eur J Neurosci [Internet]. 2014 Dec 1 [cited 2023 Feb 3];40(11):3693–703. Available from: https://onlinelibrary.wiley.com/doi/full/10.1111/ejn.12739

110. Giovannini MG, Rakovska A, Benton RS, Pazzagli M, Bianchi L, Pepeu G. Effects of novelty and habituation on acetylcholine, GABA, and glutamate release from the frontal cortex and hippocampus of freely moving rats. Neuroscience. 2001 Sep 3;106(1):43–53.

111. Puram S V., Riccio A, Koirala S, Ikeuchi Y, Kim AH, Corfas G, et al. A TRPC5-regulated calcium signaling pathway controls dendrite patterning in the mammalian brain. Genes Dev [Internet]. 2011 Dec 15 [cited 2022 Mar 25];25(24):2659–73. Available from: /pmc/articles/PMC3248686/

112. Kullback S, Leibler RA. On Information and Sufficiency. Source Ann Math Stat. 1951;22(1):79–86.

113. Skaggs WE, Mcnaughton BL, Gothard KM, Markus EJ. An Information-Theoretic

Approach to Deciphering the Hippocampal Code.

114. Cacucci F, Wills TJ, Lever C, Giese KP, O'Keefe J. Experience-dependent increase in CA1 place cell spatial information, but not spatial reproducibility, is dependent on the autophosphorylation of the alpha-isoform of the calcium/calmodulin-dependent protein kinase II. J Neurosci [Internet]. 2007 Jul 18 [cited 2024 Apr 29];27(29):7854–9. Available from: https://pubmed.ncbi.nlm.nih.gov/17634379/

115. Deacon RMJJ, Rawlins JNP. T-maze alternation in the rodent. Nat Protoc [Internet]. 2006 Jun 27 [cited 2018 Jul 19];1(1):7–12. Available from: http://www.nature.com/doifinder/10.1038/nprot.2006.2

116. Engel AK, Fries P. Beta-band oscillations — signalling the status quo? Curr Opin Neurobiol. 2010 Apr 1;20(2):156–65.

117. Miles JT, Kidder KS, Mizumori SJY. Hippocampal beta rhythms as a bridge between sensory learning and memory-guided decision-making. Front Syst Neurosci [Internet]. 2023 [cited 2024 May 20];17:1187272. Available from: /pmc/articles/PMC10196064/

118. Tort ABL, Komorowski R, Eichenbaum H, Kopell N. Measuring phase-amplitude coupling between neuronal oscillations of different frequencies. J Neurophysiol [Internet]. 2010 [cited 2022 Aug 8];104(2):1195–210. Available from: www.jn.org

119. Foster DJ, Wilson MA. Hippocampal theta sequences. Hippocampus [Internet]. 2007 Nov 1 [cited 2022 Aug 11];17(11):1093–9. Available from: https://onlinelibrary.wiley.com/doi/10.1002/hipo.20345

120. Masuda A, Sano C, Zhang Q, Goto H, McHugh TJ, Fujisawa S, et al. The hippocampus encodes delay and value information during delay-discounting decision making. Elife. 2020 Feb 1;9.

121. Keefe JO NL. The hippocampus as a cognitive map. Clarendon Press. 1978;

122. Lepannetier S, Gualdani R, Tempesta S, Schakman O, Seghers F, Kreis A, et al. Activation of TRPC1 Channel by Metabotropic Glutamate Receptor mGluR5 Modulates Synaptic Plasticity and Spatial Working Memory. Front Cell Neurosci. 2018 Sep 14;12:318.

123. Huo S, Ren J, Ma Y, Ozathaley A, Yuan W, Ni H, et al. Upregulation of TRPC5 in hippocampal excitatory synapses improves memory impairment associated with neuroinflammation in microglia knockout IL-10 mice. J Neuroinflammation [Internet]. 2021 Dec 1 [cited 2022 Aug 30];18(1):275. Available from: https://jneuroinflammation.biomedcentral.com/articles/10.1186/s12974-021-02321-w

124. Xie R, Wang Z, Liu T, Xiao R, Lv K, Wu C, et al. AAV Delivery of shRNA Against TRPC6 in Mouse Hippocampus Impairs Cognitive Function. Front Cell Dev Biol [Internet]. 2021 Jul 13 [cited 2022 Aug 31];9. Available from: /pmc/articles/PMC8313999/

125. Montgomery SM, Buzsáki G. Gamma oscillations dynamically couple hippocampal CA3 and CA1 regions during memory task performance. Proc Natl Acad Sci U S

A. 2007 Sep 4;104(36):14495–500.

126. Spellman T, Rigotti M, Ahmari SE, Fusi S, Gogos JA, Gordon JA. Hippocampal–prefrontal input supports spatial encoding in working memory. Nature [Internet]. 2015 Jun 8 [cited 2019 Sep 6];522(7556):309–14. Available from: http://www.nature.com/articles/nature14445

127. Bygrave AM, Jahans-Price T, Wolff AR, Sprengel R, Kullmann DM, Bannerman DM, et al. Hippocampal–prefrontal coherence mediates working memory and selective attention at distinct frequency bands and provides a causal link between schizophrenia and its risk gene GRIA1. Transl Psychiatry [Internet]. 2019 Dec 18 [cited 2019 Sep 6];9(1):142. Available from: http://www.nature.com/articles/s41398-019-0471-0

128. Fries P. Neuronal gamma-band synchronization as a fundamental process in cortical computation [Internet]. Vol. 32, Annual Review of Neuroscience. Annu Rev Neurosci; 2009 [cited 2022 Sep 12]. p. 209–24. Available from: https://pubmed.ncbi.nlm.nih.gov/19400723/

129. Tort ABL, Komorowski RW, Manns JR, Kopell NJ, Eichenbaum H. Theta-gamma coupling increases during the learning of item-context associations. Proc Natl Acad Sci U S A [Internet]. 2009 Dec 8 [cited 2022 Jul 29];106(49):20942–7. Available from: https://pubmed.ncbi.nlm.nih.gov/19934062/

130. Cowan N. The magical number 4 in short-term memory: A reconsideration of mental storage capacity. Behav Brain Sci [Internet]. 2001 [cited 2022 Aug 19];24(1):87–114. Available from: https://pubmed.ncbi.nlm.nih.gov/11515286/

131. Kamiński J, Brzezicka A, Wróbel A. Short-term memory capacity (7±2) predicted by theta to gamma cycle length ratio. Neurobiol Learn Mem. 2011 Jan 1;95(1):19–23.

132. Shirvalkar PR, Rapp PR, Shapiro ML. Bidirectional changes to hippocampal theta-gamma comodulation predict memory for recent spatial episodes. Proc Natl Acad Sci U S A [Internet]. 2010 Apr 13 [cited 2022 Aug 19];107(15):7054–9. Available from: https://pnas.org/doi/full/10.1073/pnas.0911184107

133. Axmacher N, Henseler MM, Jensen O, Weinreich I, Elger CE, Fell J. Cross-frequency coupling supports multi-item working memory in the human hippocampus. Proc Natl Acad Sci U S A [Internet]. 2010 Feb 16 [cited 2022 Jan 31];107(7):3228–33. Available from: https://www.pnas.org/content/107/7/3228

134. Malhotra S, Cross RWA, Van Der Meer MAA. Theta phase precession beyond the hippocampus [Internet]. Vol. 23, Reviews in the Neurosciences. Rev Neurosci; 2012 [cited 2022 Aug 18]. p. 39–65. Available from: https://pubmed.ncbi.nlm.nih.gov/22718612/

135. Robbe D, Buzsáki G. Alteration of theta timescale dynamics of hippocampal place cells by a cannabinoid is associated with memory impairment. J Neurosci [Internet]. 2009 Oct 7 [cited 2022 Aug 18];29(40):12597–605. Available from: www.jneurosci.org

136. Lasztóczi B, Klausberger T. Hippocampal Place Cells Couple to Three Different

Gamma Oscillations during Place Field Traversal. Neuron [Internet]. 2016 Jul 6 [cited 2022 Sep 21];91(1):34–40. Available from: https://pubmed.ncbi.nlm.nih.gov/27387648/

137. Sabariego M, Schönwald A, Boublil BL, Zimmerman DT, Ahmadi S, Gonzalez N, et al. Time Cells in the Hippocampus Are Neither Dependent on Medial Entorhinal Cortex Inputs nor Necessary for Spatial Working Memory. Neuron. 2019 Jun 19;102(6):1235-1248.e5.

138. Goldman-Rakic PS. Cellular basis of working memory. Vol. 14, Neuron. Cell Press; 1995. p. 477–85.

139. MacDonald CJ, Lepage KQ, Eden UT, Eichenbaum H. Hippocampal “time cells” bridge the gap in memory for discontiguous events. Neuron [Internet]. 2011 Aug 25 [cited 2022 Aug 29];71(4):737–49. Available from: https://pubmed.ncbi.nlm.nih.gov/21867888/

140. Horst NK, Laubach M. Working with memory: evidence for a role for the medial prefrontal cortex in performance monitoring during spatial delayed alternation. J Neurophysiol [Internet]. 2012 Dec 15 [cited 2022 Aug 29];108(12):3276–88. Available from: https://www.physiology.org/doi/10.1152/jn.01192.2011

141. Baeg EH, Kim YB, Huh K, Mook-Jung I, Kim HT, Jung MW. Dynamics of population code for working memory in the prefrontal cortex. Neuron. 2003 Sep 25;40(1):177–88.

142. Inglebert Y, Aljadeff J, Brunel N, Debanne D. Synaptic plasticity rules with physiological calcium levels. Proc Natl Acad Sci U S A [Internet]. 2020 Dec 26 [cited 2022 Aug 23];117(52):33639–48. Available from: https://www.pnas.org/doi/abs/10.1073/pnas.2013663117

143. Acquas E, Wilson C, Fibiger HC. Conditioned and Unconditioned Stimuli Increase Frontal Cortical and Hippocampal Acetylcholine Release: Effects of Novelty, Habituation, and Fear. J Neurosci [Internet]. 1996 May 1 [cited 2023 Feb 28];16(9):3089–96. Available from: https://www.jneurosci.org/content/16/9/3089

144. Marrosu F, Portas C, Mascia MS, Casu MA, Fà M, Giagheddu M, et al. Microdialysis measurement of cortical and hippocampal acetylcholine release during sleep-wake cycle in freely moving cats. Brain Res. 1995 Feb 13;671(2):329–32.

145. Arai J, Natsume K. The properties of carbachol-induced beta oscillation in rat hippocampal slices. Neurosci Res. 2006 Feb 1;54(2):95–103.

146. Shimono K, Brucher F, Granger R, Lynch G, Taketani M. Origins and Distribution of Cholinergically Induced β Rhythms in Hippocampal Slices. J Neurosci [Internet]. 2000 Nov 15 [cited 2023 Feb 27];20(22):8462–73. Available from: https://www.jneurosci.org/content/20/22/8462

147. Chen X, Sooch G, Demaree IS, White FA, Obukhov AG. Transient Receptor Potential Canonical (TRPC) Channels: Then and Now [Internet]. Vol. 9, Cells. NLM (Medline); 2020 [cited 2022 Oct 26]. Available from: /pmc/articles/PMC7565274/

Acknowledgment

Die Danksagung ist in der Version aus Datenschutzgründen nicht enthalten.

Declaration of honor

I hereby declare that I prepared this thesis without impermissible help of third parties and that none other than the indicated tools have been used; all sources of information are clearly marked, including my own publications.

In particular, I have not consciously:

- Invented results or concealed contradictory results.
- Deliberately misused statistical methods in order to interpret data in an unjustified manner.
- Plagiarized third-party results or publications.
- Reproduced third-party research results in a distorted manner.

I am aware that violations of copyright may lead to injunction and damage claims of the author and also to prosecution by the law enforcement authorities.

I hereby agree that the thesis may be reviewed for plagiarism by mean of electronic data processing.

This work has not yet been submitted as a doctoral thesis in the same or a similar form in Germany or in any other country. It has not yet been published as a whole.

Magdeburg

Educational path

Der Lebenslauf ist in der Version aus Datenschutzgründen nicht enthalten.

Attachments